

# **Structural Analysis and Correlative Cathodoluminescence Investigations of Pr (doped) Niobates**

Von der Fakultät für Georessourcen und Materialtechnik  
der Rheinisch-Westfälischen Technischen Hochschule Aachen

zur Erlangung des akademischen Grades einer  
Doktorin der Naturwissenschaften

genehmigte Dissertation  
vorgelegt von M. Sc.

**Rasa Changizi**  
Aus Teheran, Iran

**Berichter:** Univ.-Prof. Dr. Christina Scheu  
Univ.-Prof. Jochen M. Schneider, Ph.D.

Tag der mündlichen Prüfung: 22. August 2022

Diese Dissertation ist auf den Internetseiten der Universitätsbibliothek online verfügbar



*“The photons which constitute a ray of light behave like intelligent human beings: out of all possible curves they always select the one which will take them most quickly to their goal.”*

Max Planck, 1968



# Abstract

In the last 40 years, great attention has been given to lanthanide (doped) compounds. These are optical materials that can be used in various applications to make lasers, LEDs as well as biological imaging systems. The reason for the good luminescent behaviour of lanthanide ions lies behind the inner shell 4f-4f electronic transitions which give rise to sharp emission lines. To develop lanthanide (doped) compounds with brighter emission lines it is essential to understand their optical properties and the mechanism of energy transfer between lanthanide ions and surrounding ions within the crystal.

This PhD work is about the luminescent properties of Pr (doped) niobates and focuses on the reasons behind the great luminescent properties of PrNbO<sub>4</sub>. Polycrystalline samples were studied which have been prepared with a solid-state route. Two phases, namely Pr<sup>3+</sup>:Ca<sub>2</sub>Nb<sub>2</sub>O<sub>7</sub> (with a cubic crystal structure) and PrNbO<sub>4</sub> (crystalized in a monoclinic structure) were produced as μm-sized particles. In addition, Pr<sup>3+</sup> doped Ca<sub>2</sub>Nb<sub>3</sub>O<sub>10</sub> nanosheets were investigated.

In the first part of the thesis, Pr<sup>3+</sup>:Ca<sub>2</sub>Nb<sub>2</sub>O<sub>7</sub> and PrNbO<sub>4</sub> were compared regarding their crystal structure, chemical composition and emission spectra for individual particles. Scanning electron microscopy in addition to energy dispersive X-ray spectroscopy were performed to investigate the morphology and chemical composition of the particles. By using a cathodoluminescence spectrometer attached to the scanning electron microscope, emission spectra for each phase were acquired. The crystal structure of individual particles was revealed using transmission electron microscope. The correlation between the optical properties and the crystal structure was obtained. Brighter emissions lines were observed for PrNbO<sub>4</sub>. Higher Pr content was the main reason for this finding. In this phase, both K and Ca from the initial KCa<sub>2</sub>Nb<sub>3</sub>O<sub>10</sub> host were substituted by Pr. As a result, Pr<sup>3+</sup> ions occupy the sites with C<sub>2</sub> symmetry which perturbs the parity forbidden rule and yields sharp f-f transitions.

PrNbO<sub>4</sub> and the underlying reasons for the good luminescent behaviour of this material were further investigated and are explained in the second part of this thesis. Presence of defects (regions with high and low density of twins) was identified within the particles. The effect of such defects on the luminescent properties were examined via a correlative study. Backscattered electron imaging and emission spectra were acquired at the same location.

Focused ion beam lift out from the same region was done to study the twin's structure. On each particle two areas including twin free and twinned regions were observed. The results indicated that the regions with higher density of twins show more intense emission lines compared to the areas with less density of twins. The twins were formed during the synthesis and belong to phase transformation twinning type. Coherent structure for the twins was recognized.

Third part of the thesis is dedicated to the study of lanthanide 2D nanosheets synthesized with different Pr content. Elemental analysis for single nanosheets was performed using transmission electron microscopy revealing an average Pr concentration of 0.9 at% – 1.8 at% within the  $[\text{Ca}_2\text{Nb}_3\text{O}_{10}]^-$  sheets, respectively. Luminescent properties of the 2D nanosheets was compared to the bulk material. Additional transitions in the visible region were observed. Structural characterization of the nanosheets was carried out using high resolution transmission electron microscopy. Thin nanosheets (3 nm) correspond to one triple  $\text{Ca}_2\text{Nb}_3\text{O}_{10}$  layer surrounded by charge compensating  $\text{TBA}^+$  molecules. Thicker nanosheets (12 nm) with the same chemical composition were observed indicating that a set of 4 nanosheets were stacked on top of each other.

This thesis confirms that electron microscopy is a great tool to get insight about the chemical composition and the crystal structure of lanthanide (doped) compounds. Moreover, it explains the necessity of obtaining emission spectra for each individual particle by using a cathodoluminescence detector within the electron microscope. This enables a precise comparison between the luminescent behaviour of different phases. And it describes why  $\text{PrNbO}_4$  with higher density of twins are the better candidates for being used in optical applications.

# Kurzzusammenfassung

In den letzten 40 Jahren wurde den (dotierten) Lanthanidverbindungen große Aufmerksamkeit geschenkt. Dabei handelt es sich um optische Materialien, die in verschiedenen Anwendungen zur Herstellung von Lasern, LEDs und biologischen Bildgebungssystemen eingesetzt werden können. Der Grund für das gute Lumineszenzverhalten von Lanthanidionen liegt in den elektronischen 4f-4f-Übergängen in der inneren Schale, die zu scharfen Emissionslinien führen. Um (dotierte) Lanthanidverbindungen mit helleren Emissionslinien zu entwickeln, ist es wichtig, ihre optischen Eigenschaften und den Mechanismus der Energieübertragung zwischen Lanthanidionen und umgebenden Ionen im Kristall zu verstehen.

Diese Doktorarbeit befasst sich mit den lumineszierenden Eigenschaften von Pr-(dotierten) Niobaten und konzentriert sich auf die Gründe für die großartigen lumineszierenden Eigenschaften von  $\text{PrNbO}_4$ . Es wurden polykristalline Proben untersucht, die mit einem Festkörpervverfahren hergestellt wurden. Zwei Phasen, nämlich  $\text{Pr}^{3+}:\text{Ca}_2\text{Nb}_2\text{O}_7$  (mit kubischer Kristallstruktur) und  $\text{PrNbO}_4$  (kristallisiert in einer monoklinen Struktur) wurden als  $\mu\text{m}$ -große Partikel hergestellt. Darüber hinaus wurden mit  $\text{Pr}^{3+}$  dotierte  $\text{Ca}_2\text{Nb}_3\text{O}_{10}$ -Nanoschichten untersucht.

Im ersten Teil der Arbeit wurden  $\text{Pr}^{3+}:\text{Ca}_2\text{Nb}_2\text{O}_7$  und  $\text{PrNbO}_4$  hinsichtlich ihrer Kristallstruktur, chemischen Zusammensetzung und Emissionsspektren für einzelne Partikel verglichen. Rasterelektronenmikroskopie und energiedispersive Röntgenspektroskopie wurden durchgeführt, um die Morphologie und chemische Zusammensetzung der Partikel zu untersuchen. Mit einem Kathodolumineszenzspektrometer, das am Rasterelektronenmikroskop angebracht war, wurden Emissionsspektren für jede Phase aufgenommen. Die Kristallstruktur der einzelnen Partikel wurde mit dem Transmissionselektronenmikroskop identifiziert. Die Korrelation zwischen den optischen Eigenschaften und der Kristallstruktur wurde ermittelt. Für  $\text{PrNbO}_4$  wurden hellere Emissionslinien beobachtet. Der höhere Pr-Gehalt war der Hauptgrund für diese Beobachtung. In dieser Phase wurden sowohl K als auch Ca aus dem ursprünglichen  $\text{KCa}_2\text{Nb}_3\text{O}_{10}$ -Kristall durch Pr ersetzt. Infolgedessen besetzen  $\text{Pr}^{3+}$ -Ionen die Plätze mit  $C_2$ -Symmetrie, was die Regel des Paritätsverbots stört und zu scharfen f-f-Übergängen führt.

PrNbO<sub>4</sub> und die Gründe für das gute Lumineszenzverhalten dieses Materials wurden weiter untersucht und werden im zweiten Teil dieser Arbeit erläutert. In den Partikeln wurden Defekte (Bereiche mit hoher und niedriger Zwillingsdichte) festgestellt. Die Auswirkungen solcher Defekte auf die Lumineszenzeigenschaften wurden in einer Korrelationsstudie untersucht. Rückgestreute Elektronenbilder und Emissionsspektren wurden am selben Ort aufgenommen. Zur Untersuchung der Zwillingsstruktur wurde ein fokussierter Ionenstrahl verwendet um elektronentransparente Proben herzustellen. In jedem Partikel wurden zwei Bereiche beobachtet, darunter zwillingsfreie und zwillingsbehaftete Regionen. Die Ergebnisse zeigten, dass die Bereiche mit höherer Zwillingsdichte intensivere Emissionslinien aufweisen als die Bereiche mit geringerer Zwillingsdichte. Die Zwillinge wurden während der Synthese gebildet und gehören zum Typ der Phasenumwandlungszwillinge. Es wurde eine kohärente Struktur für die Zwillinge ermittelt.

Der dritte Teil der Arbeit ist der Untersuchung von 2D-Nanoschichten aus Lanthaniden gewidmet, die mit unterschiedlichen Pr-Gehalten synthetisiert wurden. Die Elementaranalyse der einzelnen Nanoschichten wurde mit der Transmissionselektronenmikroskopie durchgeführt und ergab eine durchschnittliche Pr-Konzentration von 0,9 at%-1,8 at% in den [Ca<sub>2</sub>Nb<sub>3</sub>O<sub>10</sub>]<sup>-</sup> Nanoschichten. Die Lumineszenzeigenschaften der 2D-Nanoschichten wurden mit denen des Bulkmaterials verglichen. Es wurden zusätzliche Übergänge im sichtbaren Bereich beobachtet. Eine strukturelle Charakterisierung der Nanoschichten wurde mit hochauflösender Transmissionselektronenmikroskopie durchgeführt. Dünne Nanoschichten (3 nm) entsprechen einer Ca<sub>2</sub>Nb<sub>3</sub>O<sub>10</sub>-Dreifachschicht, die von ladungsausgleichenden TBA<sup>+</sup>-Molekülen umgeben ist. Es wurden dickere Nanoschichten (12 nm) mit der gleichen chemischen Zusammensetzung beobachtet, was darauf hindeutet, dass ein Satz von 4 Nanoschichten übereinander gestapelt wurde.

Diese Arbeit bestätigt, dass die Elektronenmikroskopie ein hervorragendes Werkzeug ist, um Einblicke in die chemische Zusammensetzung und die Kristallstruktur von lanthaniddotierten Materialien zu erhalten. Darüber hinaus erklärt sie die Notwendigkeit, Emissionsspektren für jedes einzelne Teilchen mit Hilfe eines Kathodolumineszenzdetektors im Elektronenmikroskop zu erhalten. Dies ermöglicht einen genauen Vergleich des Lumineszenzverhaltens der verschiedenen Phasen. Und es wird beschrieben, warum



$\text{PrNbO}_4$  mit einer höheren Zwillingsdichte der bessere Kandidat für optische Anwendungen ist.



# Preface

The following publications contributed to this thesis:

## Paper I

### **Correlation between Structural Studies and the Cathodoluminescence of Individual Complex Niobate Particles**

Rasa Changizi, Siyuan Zhang, Christian Ziegler, Torsten Schwarz, Bettina V. Lotsch, and Christina Scheu

ACS Appl. Electron. Mater. 2021, 3, 461–467

## Paper II

### **Effects of Defect Density on Optical Properties Using Correlative Cathodoluminescence and Transmission Electron Microscopy Measurements on Identical PrNbO<sub>4</sub> Particles**

Rasa Changizi, Stefan Zaefferer, Lamy Abdellaoui and Christina Scheu

ACS Appl. Electron. Mater. 2022, 4, 4, 2095–2100

## Paper III

### **Structural and Cathodoluminescence Investigations of Pr<sup>3+</sup>-Doped Ca<sub>2</sub>Nb<sub>3</sub>O<sub>10</sub> Nanosheets**

Rasa Changizi, Stefan Zaefferer, Christian Ziegler, Vitaliy Romaka, Bettina V. Lotsch and Christina Scheu

Manuscript submitted



# Table of Contents

<b>Abstract .....</b>	<b>I</b>
<b>Kurzzusammenfassung .....</b>	<b>III</b>
<b>Preface .....</b>	<b>VII</b>
<b>List of abbreviations and Symbols.....</b>	<b>XIII</b>
<b>1. Introduction.....</b>	<b>1</b>
1.1. Aim of the thesis .....	3
<b>2. Fundamentals .....</b>	<b>5</b>
2.1. Lanthanides.....	5
2.2. Atomic orbitals.....	5
2.3. Electronic configuration of trivalent lanthanides.....	7
2.4. 4f electronic states transitions.....	10
2.5. Term symbols and Dieke diagram .....	12
2.6. Semiconductors.....	14
<b>3. Characterization techniques .....</b>	<b>17</b>
3.1. Electron microscopy.....	17
3.1.1. Scanning electron microscopy (SEM).....	19
3.1.2. Energy-dispersive X-ray spectroscopy (EDX) .....	21
3.1.3. Cathodoluminescence (CL) .....	23
3.1.4. Transmission electron microscopy (TEM).....	25
3.1.5. Image simulations .....	31
3.1.6. Scanning transmission electron microscopy (STEM).....	33
<b>4. Correlation between structural studies and the cathodoluminescence of individual complex niobate particles .....</b>	<b>35</b>
4.1. Literature review .....	35
4.2. Experimental details .....	36
4.2.1. Preparation of complex niobates powder .....	36
4.2.2. Characterization methods .....	37

4.3.	Results and discussions .....	37
4.3.1.	EDX and XRD data of powder.....	37
4.3.2.	Elemental analysis (EDX) of individual particles .....	39
4.3.3.	CL properties of PrNbO <sub>4</sub> and Pr <sup>3+</sup> : Ca <sub>2</sub> Nb <sub>2</sub> O <sub>7</sub> .....	42
4.3.4.	Crystal structure analysis .....	44
4.4.	Conclusion.....	46
<b>5.</b>	<b>Effects of Defect Density on Optical Properties Using Correlative Cathodoluminescence and Transmission Electron Microscopy Measurements on Identical PrNbO<sub>4</sub> Particles .....</b>	<b>49</b>
5.1.	Literature review.....	49
5.2.	Experimental procedures.....	50
5.3.	Results and Discussion.....	52
5.3.1.	(S)TEM analysis of twins and twin densities .....	52
5.3.2.	CL and BSE analysis of the twins .....	55
5.4.	Other twin types in PrNbO <sub>4</sub> .....	60
5.4.1.	Twins with (200) twin boundary plane .....	61
5.4.2.	Deformation twins .....	63
5.5.	Conclusion.....	64
<b>6.</b>	<b>Structural and Cathodoluminescence Investigations of Pr<sup>3+</sup>-Doped Ca<sub>2</sub>Nb<sub>3</sub>O<sub>10</sub> Nanosheets.....</b>	<b>67</b>
6.1.	Literature review .....	67
6.2.	Experimental procedures.....	68
6.3.	Results and discussions .....	70
6.3.1.	EDX analysis of the nanosheets .....	70
6.3.2.	Structural analysis of the nanosheets in (S)TEM .....	73
6.3.3.	CL analysis of the nanosheets .....	77
6.4.	Conclusion.....	78
<b>7.</b>	<b>Summary and Outlook.....</b>	<b>81</b>
<b>8.</b>	<b>References .....</b>	<b>85</b>
<b>9.</b>	<b>Curriculum Vitae.....</b>	<b>i</b>
<b>10.</b>	<b>List of publications, presentations and awards.....</b>	<b>iii</b>
10.1.	Scientific publications .....	iii

10.2. Poster presentations.....	iii
10.3. Awards.....	iv
<b>Acknowledgment.....</b>	<b>v</b>





## List of abbreviations and Symbols

Å	Angstrom ( $10^{-10}$ m)
ABF	Annular bright field
ADF	Annular dark field
AFM	Atomic force microscopy
at%	Atomic percent
BF	Bright field
BSE	Backscattered electron
$c$	Speed of light
CB	Conduction band
CDs	Carbon dots
CL	Cathodoluminescence
$C_s$	Spherical aberration coefficient
$C_c$	Chromatic aberration coefficient
CTF	Contrast transfer function
DF	Dark field
DFT	Density functional theory
$d_{hkl}$	Interplanar spacing of the (hkl) plane
$e^-$	Electron
ED	Electric dipole
EDX	Energy-dispersive X-ray spectroscopy
$E_F$	Fermi energy

EQ	Electric quadrupole
eV	Electron volt
FEG	Field emission gun
FFT	Fast Fourier transform
FIB	Focused ion beam
$h$	Planck's constant
$H$	Hamiltonian
HAADF	High angle annular dark field
hkl	Miller indices
HRTEM	High resolution transmission electron microscopy
IR	Infrared
$K_{ab}$	Cliff-Lorimer factor
kV	Kilovolt
$l$	Orbital angular momentum quantum number
LED	Light-emitting diode
$m$	Mass
MD	Magnetic dipole
$m_l$	Magnetic quantum number
mm	Millimetre
mrad	Milliradian
$m_s$	Electron spin quantum number
$n$	Principal quantum number
nA	Nanoampere

NIR	Near infrared
nm	Nanometer
$P$	Momentum
PE	Primary electron
PIPS	Precision ion polishing system
PL	Photoluminescence
PMT	Photomultiplier tube
$r$	Distance
RE	Rare earth
SAD	Selected area diffraction
SAED	Selected area electron diffraction
SE	Secondary electron
SEM	Scanning electron microscope
STEM	Scanning transmission electron microscope
$T$	Kinetic energy
TB	Twin boundary
TEM	Transmission electron microscope
TMDs	Transition metal dichalcogenides
$u$	Spatial frequency
UV	Ultraviolet
$V$	Potential energy
VB	Valence band
X-FEG	Extreme field emission gun

XRD	X-ray diffraction
$Z$	Atomic number
$Z^*$	Screened nucleus charge
$^{\circ}\text{C}$	Celsius
$\vartheta$	Polar angle
$\theta_{\text{Bragg}}$	Bragg angle
$\lambda$	Wavelength
$\mu\text{m}$	Micrometer
$\Delta f$	Defocus
$\Psi$	Wavefunction
$\varphi$	Azimuthal angle
$\otimes$	Convolution
$\mu$	Dipole moment
$\Delta$	Laplacian operator

# 1. Introduction

Have you ever wondered about the two rows of elements which are separately put in a box below the main body of the periodic table? The elements in the first row of the box are called lanthanides. Discovery of lanthanides goes back to the 18<sup>th</sup> century.[1] Although lanthanides are historically called “rare earth”, some of them are very common in Earth’s crust. The reason behind this etymology is related to the time when chemists would use the word earth instead of oxides. So by using rare earth they were referring to the oxides of lanthanides to distinguish them from the other renowned oxides.[2] As scientists slowly gained more knowledge about the chemistry of lanthanides, they started to use them in different applications such as chemical industries, batteries, optics, and electronics. Lanthanides applications are dependent on certain properties of each element and its compounds.[2] Therefore, the arrangement of the electrons in the inner 4f shell is very important since that makes the difference between all the elements in this group. Although various studies in the past years have been done on lanthanides applications, more details about the energy transfer between the host (or surrounding ions) and the lanthanide ions are not yet discovered. Lanthanides are used in the laser, lighting, and display industry as they have unique long lifetime luminescence.[3] The focus of this thesis is to understand the luminescence of lanthanides compounds in crystalline form with special emphasis on their crystal structure, composition and defects. Although lanthanides luminescence has been applied in applications for decades, the importance of finding new uses for it is increasingly seen in today’s research.[4]

The attention given to lanthanide optical spectroscopy started in the 1880s. Scientists including Sir William Crookes, LeCoq de Boisbaudran, Euge`ne Demarcay or, later, Georges Urbain used luminescence to analyse new elements’ crystal structure.[4] Since then the characteristic absorption and emission spectra of lanthanide compounds in a wide spectral range, including the visible, near-ultraviolet, and infrared have been investigated. This is possible due to the transitions between 4f subshells. These transitions have sharp lines and oscillators strengths typically in the order of  $10^{-6}$ .[5] f-f transitions are forbidden but after doping lanthanides into a semiconducting host these transitions become allowed and are called forced electric dipole transitions.[3,6–13] In case of compounds depending on the lanthanide surroundings these transitions can occur. More details about the electronic configuration, energy transfer mechanism, and the emission spectra are given in the next

chapter. In this work, the chosen lanthanide is Praseodymium with the atomic number 59. The name of the element stems from two Greek words: “Prasios” meaning green and “didymos” meaning twin.[1] Pr has a silvery color and shows good magnetic, optical and electrical properties.[1], [14]–[16] The main reason behind choosing  $\text{Pr}^{3+}$  as the lanthanide ion is related to its efficiency of emitting photons in a broad range: starting from the ultraviolet (UV) to infrared (IR) spectral regions.

Several studies have been done on lanthanides doped into different hosts. Among all the host materials, oxide-based materials (specifically, niobates) doped with  $\text{Ln}^{3+}$  have been suggested by many groups. In this thesis, the host  $\text{KCa}_2\text{Nb}_3\text{O}_{10}$  was used as a semiconducting host. The results are compared to those of a compound, namely  $\text{PrNbO}_4$ .

The crystal structure and composition of Pr (doped) niobates is very crucial and plays an important role in the material’s properties.  $\text{PrNbO}_4$  crystallizes in a monoclinic structure. At very high temperatures due to phase transformation, it changes to a tetragonal system. Depending on the lanthanide ion, the transformation temperature can be different. After cooling in the room temperature, the system changes to a monoclinic which leads to the formation of defects (twins).[17][18] Presence of these defects changes the luminescent properties of the material. The amount of the dopant is another vital factor for the properties. Many studies were done to find the optimum amount. If lanthanide amount is too low, there will be no luminescence and if it is too high luminescence quenching will occur. Thus, it is essential to find the optimum amount. Depending on the dopant amount different phases with various crystal structures can be formed. Since the surrounding environment of the dopant has influence on the luminescence properties of the material, it is imperative to synthesis particles in a way to reach the highest luminescence efficiency.

Lanthanide “two-dimensional” materials are another interesting class of materials which are studied increasingly.[19] Understanding the differences between the bulk and the 2D materials regarding structure and properties are the main goals which have attracted scientists. Main focus of the former studies on lanthanide 2D materials are related to synthesis and preparation of the 2D nanosheets in an efficient way. Not enough studies are reported regarding the luminescence behaviour of the nanosheets. One chapter of this thesis is dedicated to the investigation of  $\text{Pr}^{3+}$  doped  $\text{Ca}_2\text{Nb}_3\text{O}_{10}$  nanosheets. The optical properties and crystal structures of the 2D nanosheets are compared with the bulk.

In the last years, many studies were carried out on lanthanide doped oxides but no report was published to correlate optical, structural, and chemical properties measured at the identical location. Moreover, majority of studies on the optical properties are performed using photoluminescence (PL). Although PL is a great approach to obtain emission spectra for a group of particles, it is vital to do cathodoluminescence (CL) to study individual particles separately. In particular for inhomogeneous samples or two-phase materials. CL technique enables doing a correlative work and learning about the influence of different factors (crystal structure, chemistry and defects). To understand the mechanism of the energy transfer between the lanthanide ions and the surrounding it is essential to do multiple analyses. Performing transmission electron microscopy (TEM) is crucial to study materials on a nanoscopic scale in order to observe lanthanide ion surroundings, and crystal defects which can all influence the luminescence properties. Elemental analysis should be carried out by doing energy dispersive X-ray (EDX) measurements to gain information about the chemical composition.

In this thesis, a newly developed methodology was used to correlate the optical properties of the lanthanide compounds with their defect density measured at the identical particle. The main focus on Pr niobates compounds and Pr doped host show promising results and highlight that besides the structural differences the influence of local defects such as twins has to be taken into account.

### **1.1. Aim of the thesis**

The aim of this thesis is to understand the luminescent properties of lanthanide doped semiconductors and lanthanide niobate compounds through characterizing the materials with varied compositions and crystal structures. To develop better optical materials, the effect of lanthanide content and presence of defects on the optical properties are investigated. Pr as the selected lanthanide and  $\text{KCa}_2\text{Nb}_3\text{O}_{10}$  as the semiconducting host were studied. Polycrystalline  $\text{Pr}^{3+}$  doped  $\text{Ca}_2\text{Nb}_3\text{O}_{10}$  powder particles were synthesized in a solid-state route by collaborative partners from the Ludwig Maximilian University of Munich. Two phases;  $\text{Pr}^{3+}:\text{Ca}_2\text{Nb}_2\text{O}_7$  with a cubic structure and  $\text{PrNbO}_4$  with a monoclinic structure, were investigated. The optical properties for both phases were compared and the reasons behind the differences are described in detail. In addition to bulk particles, 2D nanosheets ( $\text{Pr}^{3+}$  doped  $\text{Ca}_2\text{Nb}_3\text{O}_{10}$ ) were studied. 2D materials are interesting as they have different chemical and physical properties compared to the bulk.

The particles with a micrometre size and 2D nanosheets were characterized using various analytical techniques. The microstructure and chemical composition were investigated using scanning electron microscopy (SEM), backscattered electron imaging (BSE), X-ray diffraction (XRD), and EDX. For the structural analysis TEM lamella were prepared by focused ion beam (FIB) microscopy and characterized in depth by TEM techniques including high resolution transmission electron microscopy (HRTEM). The optical properties of individual particles were studied by a cathodoluminescence spectrometer attached to the SEM. The optical properties of the lanthanide compounds were correlated with their defect density acquired at the identical particle. This was possible by observing defects using BSE and taking lamella lift out of the regions with different density of the twins. Further structural analysis on the lamellae was done using scanning transmission electron microscopy (STEM). CL study was carried out on regions with different density of twins to understand the effect of defects on the luminescence.

The outline of thesis is as follows: First chapter gives an introduction about lanthanides and the importance of studying these materials. In the second chapter, the lanthanides fundamentals including electronic configuration, atomic spectra and details about 4f-4f transitions are described. The experimental details with a focus on the electron microscopy characterization techniques are explained in chapter 3. Chapter 4 focuses on the comparison between the existing two phases,  $\text{Pr}^{3+}:\text{Ca}_2\text{Nb}_2\text{O}_7$  and  $\text{PrNbO}_4$ . Chemical composition, crystal structure, and cathodoluminescent properties of the mentioned phases are described in detail. Chapter 5 demonstrates the effect of twin density on the optical properties of the lanthanide niobate ( $\text{PrNbO}_4$ ). Lanthanide 2D nanosheets, and their structure and effect on the luminescence are studied in chapter 6. Specifically,  $\text{Pr}^{3+}$  doped  $\text{Ca}_2\text{Nb}_3\text{O}_{10}$  nanosheets with a Pr content of less than 2 at% are investigated. The thesis is summarized in chapter 7 and an outlook is given.



## 2. Fundamentals

This chapter starts with a short introduction on lanthanides. Later in the chapter details of the lanthanides electronic configuration, atomic spectra and transitions are discussed. At the end of the chapter, basic information about semiconductors is given.

### 2.1. Lanthanides

Lanthanides consist of a group of 15 elements on the periodic table with the atomic numbers 57 to 71. Due to the similarities in the electronic configuration, all the rare earth elements (RE) have many physical properties in common.[20] And, since only electrons in the inner orbitals (4f) are changing and not the valence electrons, there are only a few differences between lanthanides' chemical behavior. Based on this fact, lanthanides are called inner transition elements and are placed in a separate row below the main periodic table of elements.[21]

For lanthanide ions, following the Aufbau principle and Madelung's energy ordering rule, 4f orbitals are the first to get filled.[20] Although 4f orbitals are part of the valence configuration, they are very well shielded by the outer filled 5s and 5p orbitals from the coordination environment and will not participate in the chemical bonding formation or interact with ligands.[5] As a result, the spectroscopic and magnetic properties of RE elements are vastly influenced.[20] In the following sections, details about 4f orbitals and RE transitions and their atomic spectra are given.

### 2.2. Atomic orbitals

In classical physics, by applying Newton's second law:  $F=md^2x/dt^2$  the position of a particle of mass  $m$  is given at any time:  $x(t)$ . By knowing that, the velocity ( $v=dx/dt$ ), the momentum ( $P=mv$ ), and the kinetic energy ( $T=1/2 mv^2$ ) can be calculated.[22]

However, in quantum mechanics, the same problem is approached differently. In this case, wavefunction of a particle ( $\psi(x,t)$ ) is given by solving the Schrödinger equation. In this approach, a particle is not considered as a localized object but rather as a wave which is spread out in space.[22] The Schrödinger equation is given by:

$$H\psi = E\psi \tag{2.1}$$

Here  $H$  is the Hamiltonian operator,  $\Psi$  and  $E$  are the eigenfunctions and eigenvalues of  $\Psi$ , respectively. The time-dependent Schrödinger equation can be described as:

$$-\frac{\hbar^2}{2m} \frac{\partial^2 \psi}{\partial x^2} + V\psi = i\hbar \frac{\partial \psi}{\partial t} \quad (2.2)$$

$\hbar$  is the reduced Planck's constant and is equal to  $h/2\pi$ :  $1.054 \times 10^{-34}$  J s,  $V$  is the potential energy and  $i = \sqrt{-1}$ .

In case of a Hydrogen atom (an atom with one electron), the Hamiltonian can be described as:[4]

$$H = -\frac{1}{2} \Delta - \frac{1}{r} \quad (\text{with } \Delta \text{ or Laplacian which is defined as } \nabla^2 = \frac{\partial^2}{\partial x^2} + \frac{\partial^2}{\partial y^2} + \frac{\partial^2}{\partial z^2}) \quad (2.3)$$

The first term in Eq.3 belongs to the kinetic energy of the electron and the second term describes the Coulomb's attraction between the nucleus and the electron, divided by a distance  $r$ .

If there are more than one electron in the configuration, the Hamiltonian is changed to the equation given below:

$$H_e = \sum_i \left( -\frac{1}{2} \Delta_i - \frac{Z^*}{r_i} \right) + \sum_{i \neq j} \left( \frac{1}{r_{ij}} \right) \quad (2.4)$$

The first term is similar to Eq.3 with the difference of taking  $Z^*$  (screened nucleus charge) into account. In the second term, the repulsion between electrons located at a distance  $r_{ij}$  is added.[4]

By solving the Schrödinger equation (Eq.1), wavefunctions are obtained. Four quantum numbers are assigned to each wavefunction. These quantum numbers are called, principal quantum number ( $n$ ), the orbital angular momentum quantum number ( $l$ ), the magnetic quantum number ( $m_l$ ) and the electron spin quantum number ( $m_s$ ).  $n$  represents the energy level of an electron and can be any integer number (1, 2, 3, etc.).  $l$  defines the shape of an orbital and varies from 0 to  $(n-1)$ .  $m_l$  can change between  $-l$  and  $+l$  and determines how many orbitals exist per energy level. Finally, the spin quantum number or  $m_s$  adopts a value of either  $+\frac{1}{2}$  (spin up) or  $-\frac{1}{2}$  (spin down). In agreement with Pauli's exclusion principle, only two electrons of opposite spin can exist in one orbital.[4]

In case of using polar coordinates  $(r, \vartheta, \varphi)$ , wavefunctions ( $\Psi$ ) are written as:

$$\Psi_{n,l,m_l,m_s} \propto R_{n,l}(r) \cdot \Phi_{l,m_l}(\vartheta, \varphi) \cdot S_{m_s} \quad (2.5)$$

Where,  $R_{n,l}$ ,  $\Phi_{l,m_l}$  and  $S_{m_s}$  stand for radial function, angular function and spin function, respectively.[4]

### 2.3. Electronic configuration of trivalent lanthanides

The electron configuration of the trivalent lanthanides is  $[\text{Xe}]4f^N$ , where  $N$  starts from 1 for ( $\text{Ce}^{3+}$ ) to 13 for ( $\text{Yb}^{3+}$ ).[23] No 4f-4f transition occurs for  $\text{La}^{3+}$  ( $N=0$ ) and  $\text{Lu}^{3+}$  ( $N=14$ ). In the first case there are no electrons in the 4f orbitals and in the second one, 4f orbitals are completely filled.[23]

As mentioned earlier in this chapter, 4f orbitals are very well shielded with the filled 5s and 5p orbitals which are located in the outer most (see Fig.2.1). As a result, 4f electrons cannot be mixed with the surrounding orbitals. Fig.2.2 shows the radial charge density ( $R^2$ ) of the valence orbitals of  $\text{Pr}^{3+}$ . [20] As seen on this figure, most of the 4f orbitals are much less spatially extended than the 5s and 5p orbitals. This leads to very sharp emission spectra between the 4f states for all the lanthanides.[4], [19]

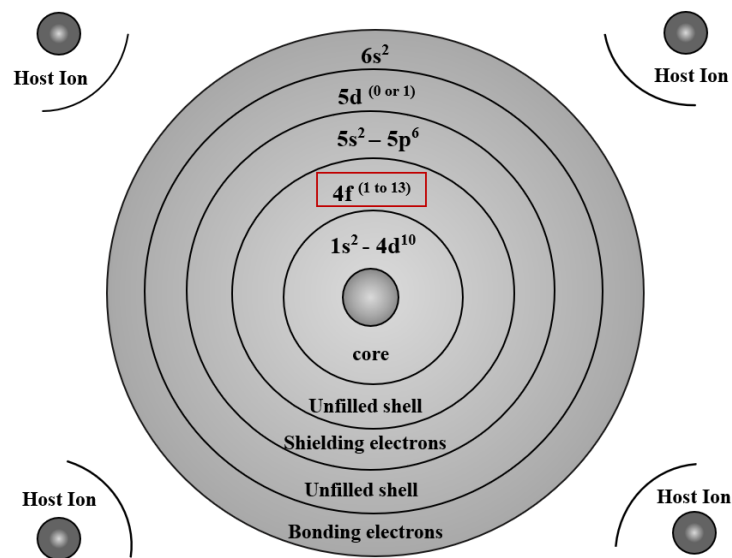


**Figure 2.1** Representation of the atomic structure of the lanthanide series. Adapted from [24]

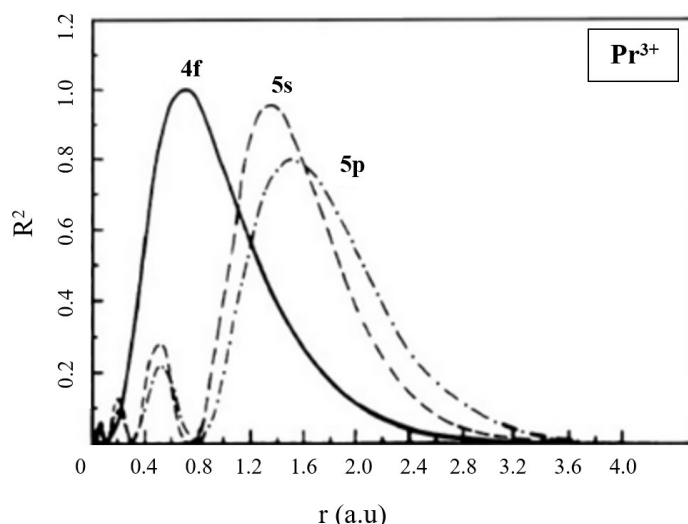


**Figure 2.2** Radial charge density of the valence orbitals of  $\text{Pr}^{3+}$  as a function of distance  $r$  from the nucleus. As shown on this figure, the 5s and 5p orbitals are much more extended in space compared to 4f orbitals. Reproduced with permission from [20]. © 2012 John Wiley and Sons, Ltd

Although most common oxidation state for lanthanide ions is 3+, some stable compounds can be formed where the oxidation state is 2+ (e.g. Nd, Sm, Eu, Dy, Tm and Yb) and 4+ (e.g. Ce, Pr, Nd, Tb and Dy).[23] The valence configurations for the lanthanides are summarized in table 2.1.[20]

**Table 2.1:** Lanthanides' valence electron configurations in the oxidation states 0, 2+, 3+ and 4+ and their term symbols. Reproduced with permission from [20] © 2012 John Wiley and Sons, Ltd

Atomic number	Element symbol	Valence configuration	Term symbol	Valence configuration of $\text{Ln}^{+3}$	Term symbol of $\text{Ln}^{+3}$	Valence configuration of $\text{Ln}^{+2}$	Valence configuration of $\text{Ln}^{+4}$
57	La	$[\text{Xe}]5d^16s^2$	$^2D_{3/2}$	$[\text{Xe}]$	$^1S_0$	$[\text{Xe}]5d^1$	$[\text{Kr}]4d^{10}5s^25p^5$
58	Ce	$[\text{Xe}]4f^15d^16s^2$	$^3H_4$	$[\text{Xe}]4f^1$	$^2F_{5/2}$	$[\text{Xe}]4f^2$	$[\text{Xe}]$
59	Pr	$[\text{Xe}]4f^36s^2$	$^4I_{9/2}$	$[\text{Xe}]4f^2$	$^3H_4$	$[\text{Xe}]4f^3$	$[\text{Xe}]4f^1$
60	Nd	$[\text{Xe}]4f^36s^2$	$^5I_4$	$[\text{Xe}]4f^3$	$^4I_{9/2}$	$[\text{Xe}]4f^4$	$[\text{Xe}]4f^2$
61	Pm	$[\text{Xe}]4f^56s^2$	$^6H_{5/2}$	$[\text{Xe}]4f^4$	$^5I_4$	$[\text{Xe}]4f^5$	$[\text{Xe}]4f^3$
62	Sm	$[\text{Xe}]4f^66s^2$	$^7F_0$	$[\text{Xe}]4f^5$	$^6H_{5/2}$	$[\text{Xe}]4f^6$	$[\text{Xe}]4f^4$
63	Eu	$[\text{Xe}]4f^76s^2$	$^8S_{7/2}$	$[\text{Xe}]4f^6$	$^7F_0$	$[\text{Xe}]4f^7$	$[\text{Xe}]4f^5$
64	Gd	$[\text{Xe}]4f^75d^16s^2$	$^9D_2$	$[\text{Xe}]4f^7$	$^8S_{7/2}$	$[\text{Xe}]4f^75d^1$	$[\text{Xe}]4f^6$
65	Tb	$[\text{Xe}]4f^96s^2$	$^6H_{15/2}$	$[\text{Xe}]4f^8$	$^7F_6$	$[\text{Xe}]4f^9$	$[\text{Xe}]4f^7$
66	Dy	$[\text{Xe}]4f^{10}6s^2$	$^5I_8$	$[\text{Xe}]4f^9$	$^6H_{15/2}$	$[\text{Xe}]4f^{10}$	$[\text{Xe}]4f^8$
67	Ho	$[\text{Xe}]4f^{11}6s^2$	$^4I_{15/2}$	$[\text{Xe}]4f^{10}$	$^5I_8$	$[\text{Xe}]4f^{11}$	$[\text{Xe}]4f^9$
68	Er	$[\text{Xe}]4f^{12}6s^2$	$^3H_6$	$[\text{Xe}]4f^{11}$	$^4I_{15/2}$	$[\text{Xe}]4f^{12}$	$[\text{Xe}]4f^{10}$
69	Tm	$[\text{Xe}]4f^{13}6s^2$	$^2F_{7/2}$	$[\text{Xe}]4f^{12}$	$^3H_6$	$[\text{Xe}]4f^{13}$	$[\text{Xe}]4f^{11}$
70	Yb	$[\text{Xe}]4f^{14}6s^2$	$^1S_0$	$[\text{Xe}]4f^{13}$	$^2F_{7/2}$	$[\text{Xe}]4f^{14}$	$[\text{Xe}]4f^{12}$
71	Lu	$[\text{Xe}]4f^{14}5d^16s^2$	$^2D_{5/2}$	$[\text{Xe}]4f^{14}$	$^1S_0$	$[\text{Xe}]4f^{14}6s^1$	$[\text{Xe}]4f^{13}$

In general, the spectroscopic properties of RE ions is determined by the electronic interactions.[5] Historically, a complete Hamiltonian for  $4f^N$  configurations was obtained in two ways. 1) Taking the fundamental electronic interactions, such as electrostatic Coulomb interactions and spin-orbit coupling into account. 2) Considering the crystal field interaction when the ion is in a condensed phase.[5]

With that being mentioned, the next contribution to Eq.4 is the spin-orbit interaction described by  $H_{SO}$ . The Hamiltonian is then given as [4]:

$$H = H_e + H_{SO} = \sum_i \left( -\frac{1}{2} \Delta_i - \frac{Z}{r_i} \right) + \sum_{i \neq j} \left( \frac{1}{r_{ij}} \right) + H_{SO} \quad (2.6)$$

This interaction is created by the intrinsic magnetic moment of the electron with the magnetic field induced when electron moves around the nucleus. The magnitude of the spin-orbit interaction increases as  $Z^4$  (with  $Z$  being the nuclear charge).[23] For light elements, spin-orbit coupling is smaller than  $H_e$  (electrostatic interaction between 4f electrons) but for RE elements,  $H_{SO}$  becomes comparable to  $H_e$ . [23] By increasing the relative magnitude of the spin-orbit coupling, both  $S$  ( $\sum s_i$ ) and  $L$  ( $\sum l_i$ ) are no longer good quantum numbers, and  $J$  as the total angular momentum must be introduced. In fact,  $J$  represents the coupling of  $S$  and  $L$ . However, the rare earth elements indicate an ‘‘intermediate coupling’’ case ( $H_{SO} \approx H_e$ ) where the spin-orbit interaction causes splitting in different energy levels for RE<sup>3+</sup> ions configuration and therefore,  $^{2s+1}L$  changes to  $^{2s+1}L_J$ , where  $J$  is equal to  $|L-S|, |L-S+1|, \dots, |L+S|$ . [23]

$H_{SO}$  is given via:

$$H_{SO} = \sum_i \xi(\vec{r}_i) (\vec{S}_i \cdot \vec{L}_i) \quad \left( \xi(\vec{r}_i) \text{ is defined as } \left( \frac{\hbar^2}{2\pi c^2 m^2 r_i} \right) \left\{ \frac{dV(r_i)}{dr_i} \right\} \right) \quad (2.7)$$

$r_i, s_i$  and  $l_i$  are the radial coordinate, spin and orbital angular momentum of the  $i$ -th electron, respectively. The central field potential is defined as  $V(r_i)$  with  $\hbar$  being the Planck constant,  $m$  the mass of the electron and  $c$  the speed of light.[23]

In general, for RE<sup>3+</sup> ions, the electrostatic ( $H_e$ ) and spin-orbit ( $H_{SO}$ ) interactions are the dominant ones.[23] The energy levels of the RE<sup>3+</sup> ion in the spherical symmetry of free space or in another word ‘‘free ions’’ are indicated by  $^{2s+1}L_J$  multiplets. When RE<sup>3+</sup> ion is placed into the lower symmetry electrostatic field, due to the charges of the neighbouring ions in a solid, the spherical symmetry of its electronic structure is destroyed.[4] As a result,

depending on the exact symmetry of the metal–ion site a much smaller energy splitting occurs. However, in the next section, the importance of the crystal-field interactions is explained. It is in fact because of these interactions that parity-forbidden 4f-4f transitions become allowed.[23]

## 2.4. 4f electronic states transitions

The Judd-Ofelt theory which was introduced over 50 years ago is the most essential study on the 4f-4f transitions.[23] This theory enables us to understand and analyse the transition intensities in the so-called forbidden transitions.[23] Before starting with the Judd-Ofelt theory, the basics of electronic transitions and spectroscopy will be introduced.

When an atom absorbs a photon, the energy of that photon is transferred to the electron. As a result, the electron will go to higher energy states. The absorption is defined by “operators” related to the nature of light. These operators are called, the odd-parity electric dipole (ED) operator  $\vec{P}$ , the even-parity magnetic dipole (MD) operator  $\vec{M}$  and electric quadrupole (EQ) operator  $\vec{Q}$ . [4] And they are defined as:

$$\vec{P} = -e \sum_{i=0}^N \vec{r}_i \quad (2.8)$$

$$\vec{M} = -\frac{eh}{4\pi mc} \sum_{i=0}^N (\vec{l}_i + 2\vec{s}_i) \quad (2.9)$$

$$\vec{Q} = \frac{1}{2} \sum_{i=0}^N (\vec{k} \cdot \vec{r}_i) \cdot \vec{r}_i \quad (2.10)$$

Here, the wave-vector of the photon is defined with  $\vec{k}$ . [3] Other variables such as  $r_i$ ,  $s_i$ ,  $l_i$ ,  $h$ ,  $m$  and  $c$  were introduced above. Like the absorption, emission of light through f–f transitions is achieved by either electric dipole or magnetic dipole mechanisms.

Lanthanide ions can have three types of electronic transitions: sharp intraconfigurational 4f-4f transitions, broader 4f-5d transitions, and broad charge-transfer transitions (metal to ligand or ligand-to metal).[4] Following selection rules, not all the transitions are allowed. Laporte’s parity selection rule (given in Table 2.2) implies f–f transitions are forbidden because of having same parity in the initial and final states of transition. However, when the lanthanide ion is under the influence of a crystal field, non-centrosymmetric (without inversion of symmetry) interactions allow the mixing of electronic states of opposite parity

into the 4f wavefunctions. This relaxes the selection rules and the transition becomes partially allowed; it is called an induced electric dipole transition. Although magnetic dipole transitions are allowed, their intensity is weak. For the case of 4f-4f transition, their intensity in emission spectra is very similar to the one from the induced electric dipole transitions.[4]

**Table 2.2:** Selection rules for intra-configurational f-f transitions. Reproduced with permission from [4]. © Springer-Verlag Berlin Heidelberg 2011

<b>Operator</b>	<b>Parity</b>	$\Delta S$	$\Delta L$	$\Delta J$
ED	Opposite	0	$\leq 6$	$\leq 6$ (2,4,6 if J=0)
MD	Same	0	0	0, $\pm 1$
EQ	Same	0	0, $\pm 1$ , $\pm 2$	0, $\pm 1$ , $\pm 2$

There are also parity allowed quadrupolar transitions but their intensity is even weaker than MD transitions, and therefore they are usually not observed. Some induced ED transitions are called hypersensitive as they are highly sensitive to the changes in the Ln<sup>3+</sup> environment. Since these transitions follow the selection rules of EQ transitions they are called pseudo-quadrupolar transitions.[4] One should take into consideration that the terms “forbidden” and “allowed” transitions are not totally accurate. A forbidden transition does not indicate that a transition will never happen but rather it has a low probability of happening, while an allowed transition has a high probability of occurring.[4]

The probability that a transition occurs from one state ( $\Psi_1$ ) to another state ( $\Psi_2$ ), is proportional to the transition moment ( $\vec{M}_{12}$ ) given below [23]:

$$\vec{M}_{12} = \int \psi_2 \vec{\mu} \psi_1 d\tau \quad (2.11)$$

$\vec{\mu}$  stands for the dipole moment operator.

The 4f wavefunctions have ungerade (u) inversion symmetry. The electric-dipole (ED) interactions have also an operator with ungerade (u) inversion symmetry. Therefore, for an ED-induced 4f-4f transition, the direct product is  $u \otimes u \otimes u = u$ . However, since Eq.11 becomes non-zero only if the direct product of  $\psi_2 \otimes \vec{\mu} \otimes \psi_1$  is symmetric (gerade), therefore, 4f-4f transition has zero probability to occur. Symbol  $\otimes$  is the sign for convolution. To make such transitions allowed, some admixture of states with opposite parity into the 4f wavefunctions is needed. Such admixtures can be done in a solid, by odd-parity crystal-field parts which causes electronic transitions to occur. This explains the

fundamental idea of the Judd–Ofelt theory. Further mathematical treatment of the parity by the crystal-field perturbation is not the focus of this thesis. Details can be found in [23].

## 2.5. Term symbols and Dieke diagram

One of the earliest studies on the absorption spectra of the trivalent lanthanides was done by Dieke and Crosswhite in the 1960s at Johns Hopkins University.[25] Their work illustrates the observed energy levels of the trivalent lanthanide elements and is summarized in a diagram called ‘‘Dieke Diagram’’. This diagram was produced from experimental observations (see Fig.2.3). In order to figure out the exact influence of the crystal field, lanthanides energy levels in a crystal lattice ( $\text{Ln}^{3+}:\text{LaCl}_3$ ) were studied. The ground state of each lanthanide and the wave number ( $\text{cm}^{-1}$ ) are given by the x and y axes, respectively.

In electronic spectroscopy, to specify the electronic configuration of an electron, the atomic term symbol is used. The term symbols of the ground state of an element follow Hund’s rules: [25]

1.  $^{2s+1}L_J$  is the general form with  $J$  ranging from  $|L-S| < J < L+S$
2.  $n^*$  is the number of electrons in f orbital, if  $n^* < 7$ ,  $J$  is  $|L-S|$  and for  $n^* > 7$ , it is  $L+S$ .
3.  $L$  is represented by letters: S, P, D, F, G, H, . . . and stands for  $L=0, 1, 2, 3, 4, 5$ , etc.

As an example, to write the term symbol for the ground state of  $\text{Pr}^{3+}$ , these steps have to be followed:

1. Electron configuration for  $\text{Pr}^{3+}$  should be written:  
 $1s^2 2s^2 2p^6 3s^2 3p^6 4s^2 3d^{10} 4p^6 5s^2 5p^6 4f^2$
2. Defining  $n^*$  based on the remaining electrons inside the f orbital for  $\text{Pr}^{3+}$ ;  $n^*=2$ .
3. Defining  $S$  for  $\text{Pr}^{3+}$ ;  $S=1$ ;
4. Defining  $L$  for  $\text{Pr}^{3+}$ ;  $L=5$ ;
5. Defining  $J$  for  $\text{Pr}^{3+}$ ;  $n^*$  is smaller than 7, then  $J$  is  $L-S$ ;  $J=5-1=4$ ;

Therefore, the term symbol  $^{2s+1}L_J$  is  $^3\text{H}_4$ .



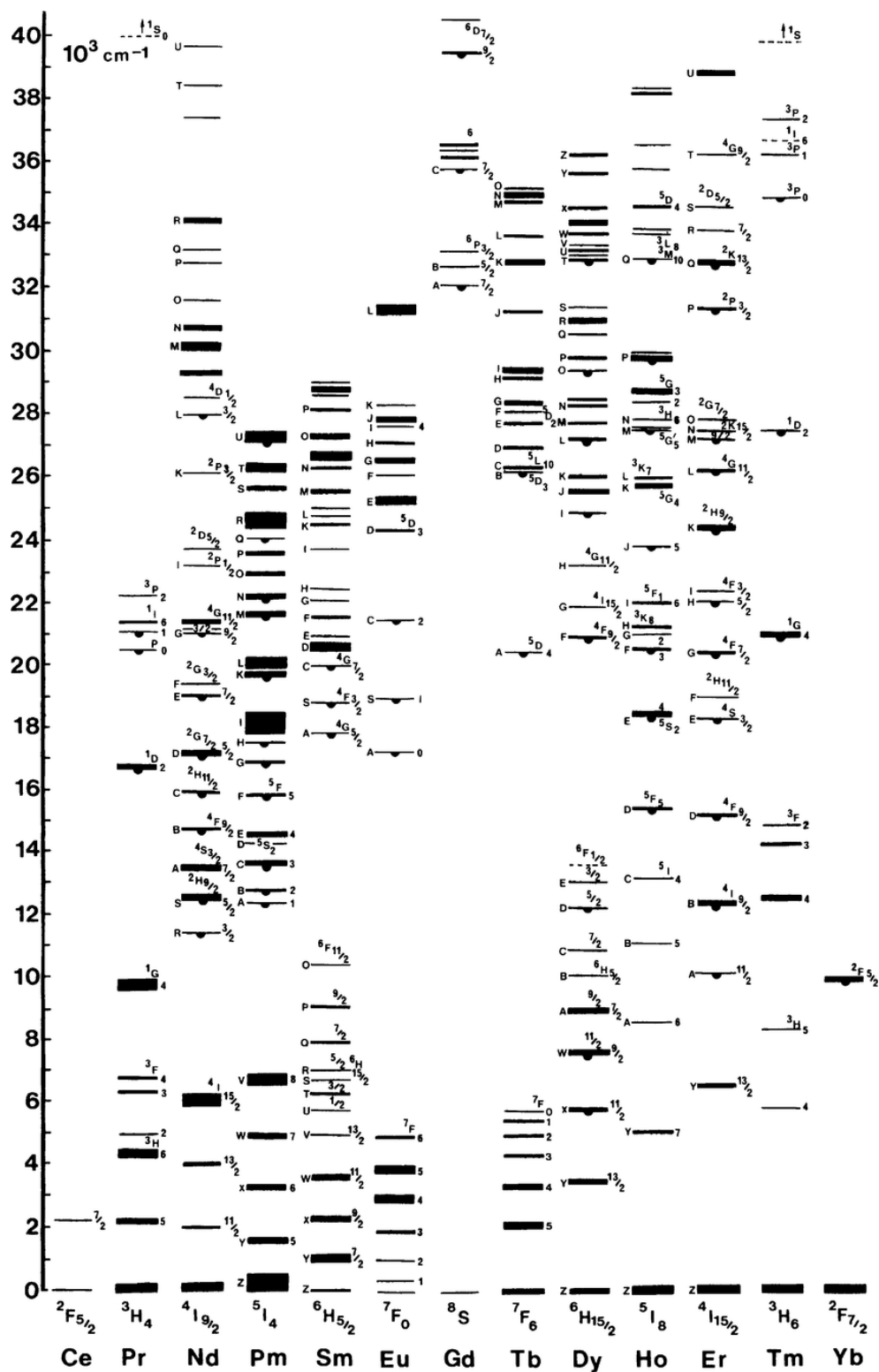


**Figure 2.3** Observed energy levels of the trivalent lanthanide ions in  $\text{LaCl}_3$ . Reproduced with permission from [26]. Copyright © 2014, Springer-Verlag

## 2.6. Semiconductors

There exist 3 classifications for the conductivity of materials including: metals, semiconductors and insulators.[27–31] These 3 classes are different in their band structures or the electronic energy states which will be explained below.

As shown in Fig.2.4.a, in metals the valence band (VB) is totally filled while the conduction band (CB) is partially (up to the Fermi level  $E_F$ ) filled. Therefore, many electrons are available for conduction. As a result, electrons can move freely leading to very high electrical conductivity.[27]

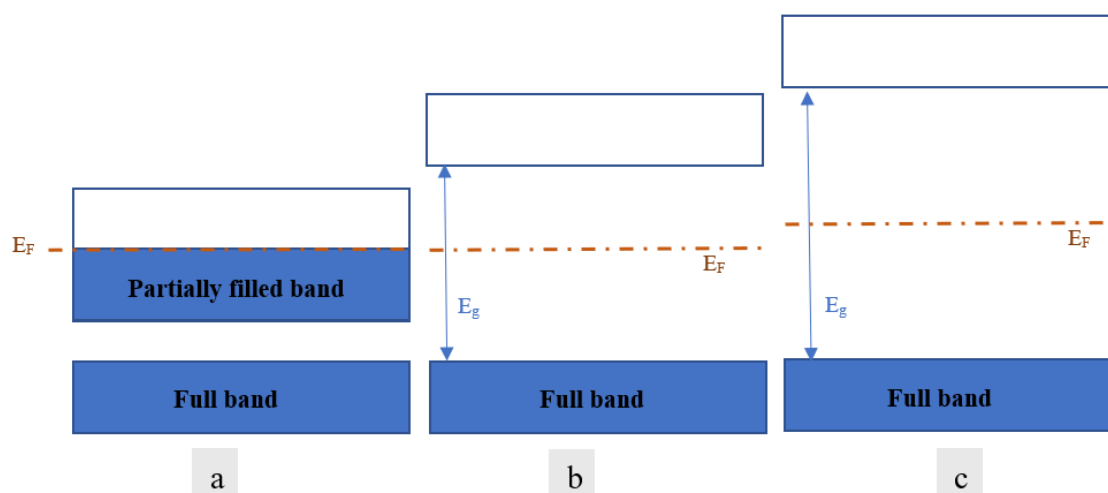


**Figure 2.4** Energy bands of (a) metal indicating partially filled CB; Electrons move from the filled states to the empty states, (b) semiconductor and (c) insulator.  $E_g$  and  $E_F$  show the energy of the bandgap and the Fermi level, respectively.

In semiconductors and insulators, there exists an energy gap between the valence band and the conduction band. In this energy gap no states exist which the valence electrons could occupy. Energy bands for a semiconductor are shown in Fig.2.4.b. At a temperature of absolute zero the conduction band is empty. Increasing the temperature provides the energy for the electrons to jump from VB to CB and leave behind a hole in the VB. The energy gap for semiconductors is usually between 0.1 to 3 eV. Semiconductors have moderate conductivity which increases with increasing temperature. The bandgap of semiconductors is generally divided into direct and indirect bandgaps. In the first case, when plotting the energy of the  $e^-$  as a function of wavevector  $\vec{k}$ , the minimum of the CB and the maximum of the VB occur at the same  $\vec{k}$ -vector. On the other hand, for indirect bandgaps, there will be a change in momentum.

If a material has a completely empty conduction band and a large bandgap, it is called insulator. The conductivity even at high temperature is negligible. The energy gap is between 3.5 to 6 eV or larger. At room temperature, no electrons exist in the CB, and the VB is completely filled. Energy bands for an insulator are schematically drawn in Fig.2.4.c. [27]

In this work,  $\text{KCa}_2\text{Nb}_3\text{O}_{10}$  (semiconducting host),  $\text{Pr}^{3+}:\text{Ca}_2\text{Nb}_2\text{O}_7$  (lanthanide doped compounds) and  $\text{PrNbO}_4$  (lanthanide niobate compounds) were investigated. According to [32], the band gap of  $\text{KCa}_2\text{Nb}_3\text{O}_{10}$  is 3.2 eV and thus a wide-bandgap semiconductor. The monoclinic  $\text{Ca}_2\text{Nb}_2\text{O}_7$  is a direct wide band gap semiconductor and has a band gap of 3.07 eV.[33] The band gap of  $\text{PrNbO}_4$  is given as 3.75 eV in [34], thus it can be classified as an insulator.



### **3. Characterization techniques**

In this chapter, a brief introduction to the basic concepts of the experimental techniques applied, with the main focus on electron microscopy, are given. Detailed information on the microscopy techniques used can be found in textbooks.[35–40]

#### **3.1. Electron microscopy**

Before the invention of electron microscopes, light microscopes played a vital role in many fields of research. Light microscopes are still important in today's research, but due to their resolution limit governed by the wavelength of the photons and decreasing object sizes, the need for a higher resolution microscope became a limiting factor. Electrons, with a shorter wavelength and negative charges are the best solution to conquer the photon resolution limit.[36] With the help of electron microscopy, material characterization on the range of micrometre to angstrom can be performed. Although the microscopy concepts such as resolution, magnification, depth of field, and lens aberrations are the same for both electron and light sources, the key difference in understanding electron microscopy lies in the interaction of electrons with the matter.[36]

Regardless of having a bulk or thin specimen, electrons will always interact with the sample. When primary electrons (PEs) of the incident electron beam interact with the sample, a group of signals are generated and recorded by different detectors.[36] These signals are created because of two vital phenomena: elastic and inelastic scattering of electrons.[36]

Elastic scattering occurs when the incident electron is scattered at the screened Coulomb potential of the atoms, leading to large scattering angles. Backscattered electrons belong to this group and they conserve almost all their energy. Electron diffraction, HRTEM, and XRD are all based on elastic scattering. Moreover, electrons can get scattered through a larger angle (more than  $90^\circ$ ) when they interact with the nucleus (Rutherford scattering)[36], which is considered as quasi-elastic scattering.

Most electron-electron interactions are inelastic, causing a small angular deviation after the primary beam electron interacts with the electron cloud or nucleus of the atom. Inelastically scattered electrons lose part of their initial energy to the atoms of the specimen. Secondary electrons, Auger electrons, characteristic X-rays, and bremsstrahlung X-rays can all be

generated as a result of this energy loss. When an electron from the incident beam collides with another electron in the outer orbital shell of an atom, i.e. electrons that belong to the conduction or valence band, the released electrons are called secondary electrons. Secondary electrons are mostly used for forming images of the specimen surface in SEM. If the collision happens in the inner shell of an atom, the created unoccupied state will be filled by another electron located in a higher energy state of the atom. The excess of energy from this higher-to-lower energy transition is released as either secondary electrons – also called Auger electrons - or as X-ray radiation. Both types of signal emission carry unique and characteristic information about the sample. Lighter elements predominately emit Auger electrons and heavier elements predominately generate X-rays. Although Auger electrons carry elemental information, they have low energies (in the range of a few hundred eV to a few keV) and are often re-absorbed by the specimen. Consequently, they are only acquired in dedicated instruments that are used for chemical analysis. X-rays are used in most elemental analysis. Electrons can also be decelerated while interacting with the Coulomb field of the nucleus. Due to the relative change in momentum during this process, bremsstrahlung X-rays are generated. These X-rays are typically non-specific radiation.[36] Fig.3.1 summarizes a group of different signals which are generated when an electron beam interacts with the atoms of a specimen.

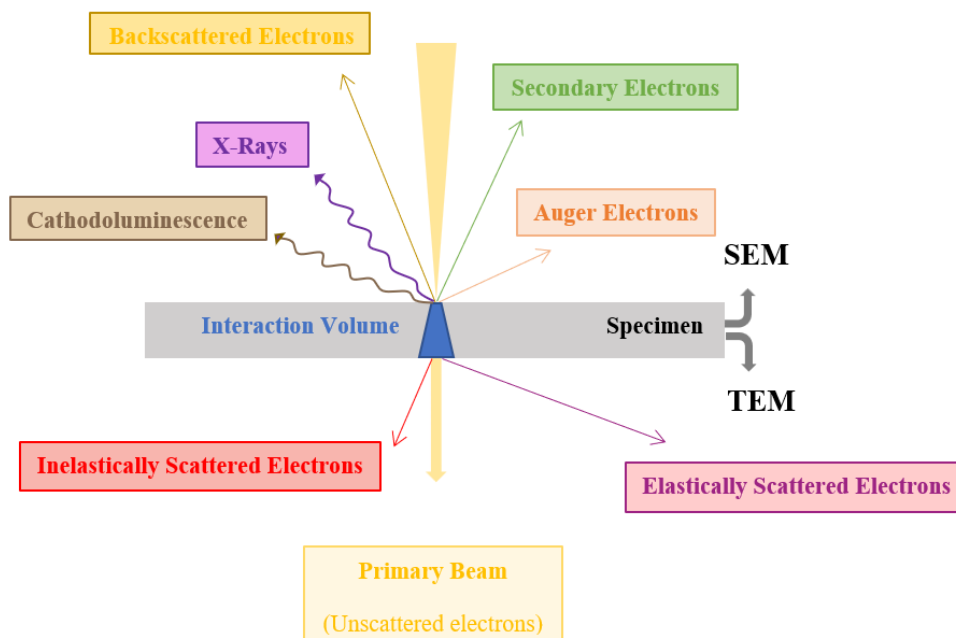


**Figure 3.1** Schematic drawing of most common interactions between an electron beam and the specimen. While in TEM, thin samples are required, thicker samples can be investigated in a SEM. The drawing is inspired by [36]

The following sections briefly describe the electron-based imaging and diffraction techniques that were used in this work.

### 3.1.1. Scanning electron microscopy (SEM)

SEM is a technique used to display the surface topography or different material phases of bulk specimens and microstructural features (grain size, etc). Electron guns with different types, namely thermionic emission or the field emission are used to generate the electrons inside an SEM.[37] In an SEM a focused electron beam with energy  $E_0 < 30$  keV is rastered over the sample and generates signals such as secondary electrons, backscattered electrons, X-rays or CL.[36,37] The optical system is composed of condenser lenses and an objective lens, through which the electrons are focused into a beam which has a diameter of 2-10 nm. The volume in which electrons penetrate until they come to rest is called interaction volume. (see Fig.3.2)

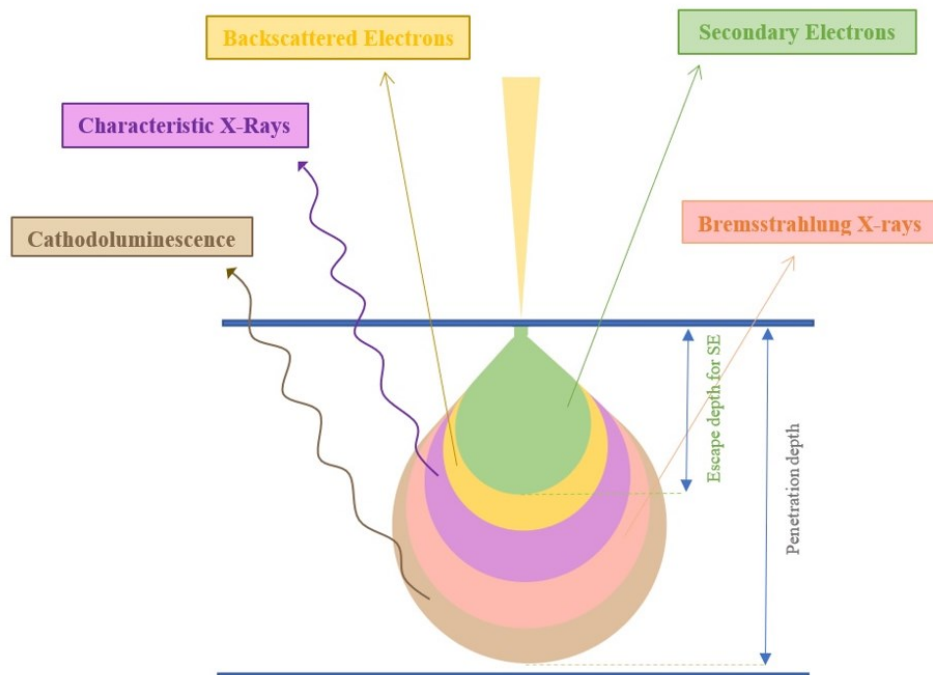


**Figure 3.2** Schematic drawing of the interaction between the electron beam and the specimen in SEM. The penetration depth relates to the interaction volume and is indicated in brown. The different signals can only escape from the regions colored in green (SE), yellow (BSE), purple (X-rays), pink (Bremsstrahlung) and brown (CL). The drawing is inspired by [37]

The atomic number of the sample and the accelerating voltage of the beam can influence the depth of the interaction volume.[40] Fig.3.3 demonstrates how penetration depth

changes by using a higher voltage or interacting with atoms with larger atomic number. Higher voltage leads to larger electron energy and larger penetration depth of electrons. For samples with higher atomic numbers, the interaction volume is small.

To obtain a high resolution image of specimen topology, secondary electrons are most commonly used. The kinetic energy of secondary electrons is less than 50 eV. In fact, most of them have energies in the range of 1-3 eV, which makes their escape depth only several tens of nanometres (up to 100 nm), suitable for surface imaging (see Fig.3.2). Secondary electrons can also be generated in the deeper part of the sample (beyond 100nm depth), but they are easily re-absorbed and cannot leave the sample, and will not be detected by a secondary electron detector.[36]

Backscattered electrons (BSE) have slightly less energy than the PEs. Their escape depth is in the order of  $\mu\text{m}$ , resulting in a limited lateral resolution. In a BSE image, elements with higher atomic numbers will appear brighter. Thus, the contrast in BSE images is  $Z$  dependent.[36] In general, the escape depth of BSE is larger than secondary electrons but less than the escape depth of X-rays (1-4  $\mu\text{m}$ ). The BSE signal carries information on specimen composition, topography and crystallography due to channelling effect (channelling of the electron beam as it travels through the sample along the atomic column).

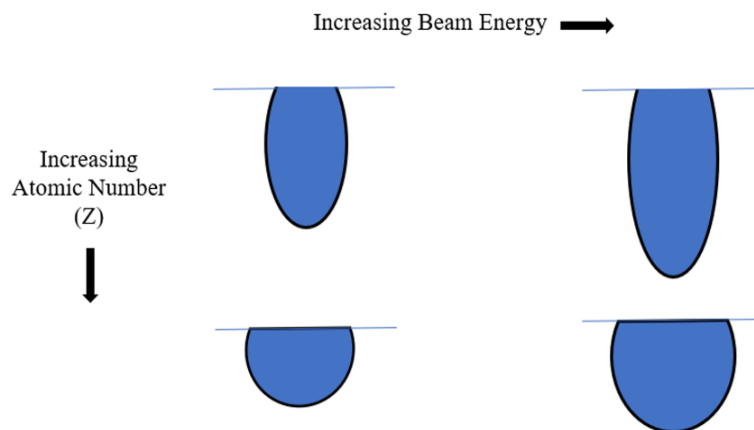


**Figure 3.3** Schematic drawing of the influence of the accelerating voltage and atomic number in SEM. Adapted from [40]

To detect secondary electrons in SEM, mainly two detectors are used - the Everhart-Thornley detector and the in-lens detector.[38,41] The Everhart-Thornley detector has a positively charged surface potential to attract the SEs, and is mounted above the specimen



in a side position. This causes an additional shadowing effect. The in-lens detector is installed above the specimen in the electron column, which allows SE collection with less pronounced shadowing effects but very good collection efficiency. In contrast to the Everhart-Thornley detector, the in-lens detector enables the microscope to operate at very short working distances with a better resolution as it mainly detects SEs. In the SEM, the working distance is the distance from the lower pole piece of the lens to the specimen.[40]

### 3.1.2. Energy-dispersive X-ray spectroscopy (EDX)

As explained in section 3.1, if the incident electron beam interacts with the inner shell electrons, bremsstrahlung X-rays and characteristic X-rays can be generated. After an electron in the inner shell gets sufficiently excited and can escape the attractive field of the nucleus, consequently, a hole will be created which can be filled by an outer shell electron. The difference in energy may be released as photon as illustrated in Fig.3.4 These photons are called characteristic X-rays as their energies are characteristic of specific atoms.[36] Bremsstrahlung X-rays appear as a continuous background signal in each EDX spectrum.

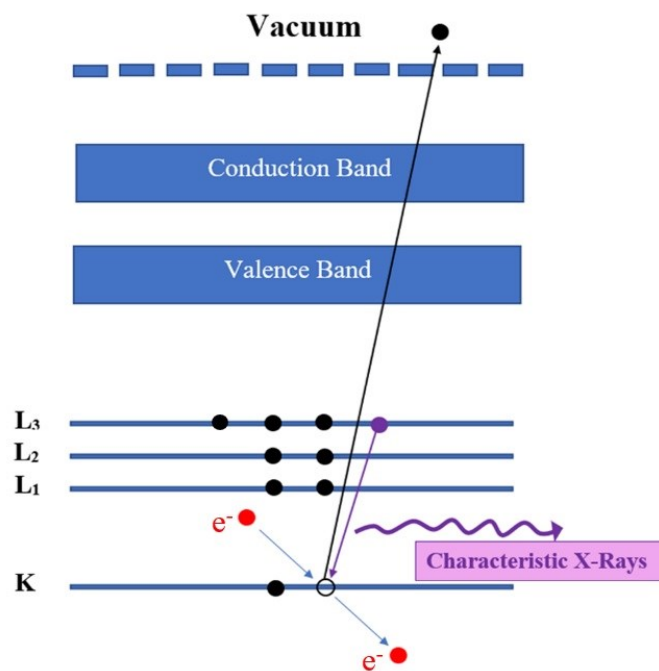


**Figure 3.4** Schematic drawing illustrating the generation of characteristic X-rays. Adapted from [36]

There are several possible transitions in a heavy atom, each of which enables the generation of an X-ray of a discrete wavelength.[36] As illustrated in Fig.3.5 below, depending on the

involved electron states, specific transitions can happen. If an electron from the L shell fills the K-shell hole,  $K_\alpha$  X-rays are generated. For relaxation from the electrons in the M shell to the K-shell hole,  $K_\beta$  X-rays are released, etc. As each element has specific and unique energy levels, measurement of the X-ray energies enables chemical identification of various elements in each specimen.

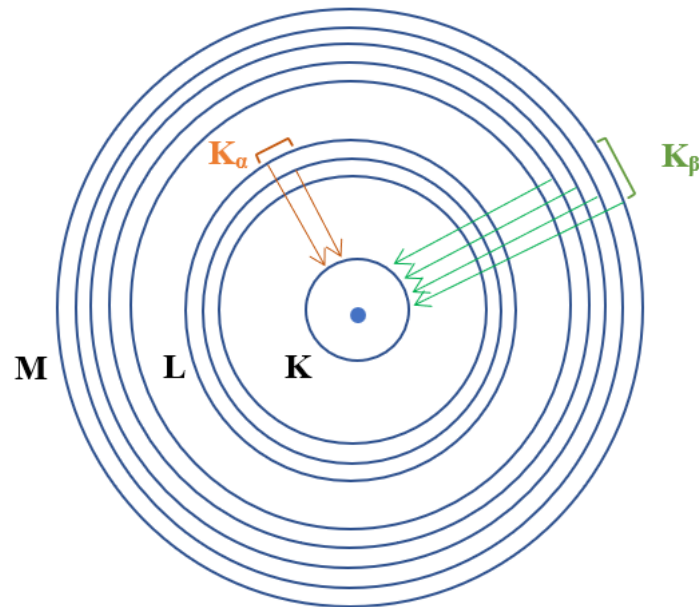


**Figure 3.5** Possible electron transitions that give rise to  $K_\alpha$  and  $K_\beta$  characteristic X-rays. Redrawn from [36]

If the sample is thin enough, the Cliff-Lorimer equation (3.1) is used to quantify the detected elements.[36]

$$\frac{C_a}{C_b} = K_{ab} \frac{I_b}{I_a} \quad (3.1)$$

$a$  and  $b$  indicate the elements,  $C_a$  and  $C_b$  stand for the concentrations, and the respective intensities of the X-ray lines are given as  $I_{a,b}$ .  $K_{ab}$  is the Cliff-Lorimer factor which depends on the voltage as well as the detector efficiency, and other parameters.

If the specimen is thick, equation 3.1 is corrected for three different factors - atomic number, absorption, and fluorescence. In this case, the ratio of the concentrations changes to [36]:

$$\frac{C_a}{C_b} = K_Z K_A K_F \frac{I_a}{I_b} \quad (3.2)$$

With  $C_a$  and  $C_b$  being the concentration of elements  $a$  and  $b$ , and respective intensities of the X-ray lines are given as  $I_{a,b}$ .  $K_z$  is a correction for atomic number,  $K_A$  is correction for absorption of X-rays in the sample and  $K_F$  corrects for any energy released as fluorescence. As mentioned before, bremsstrahlung radiation should be removed from the EDX spectrum, then X-rays lines can be used in the Cliff-Lorimer equation. These steps are performed automatically by most commercial EDX software and are critical to obtain quantitative, rather than qualitative chemical information about the sample.

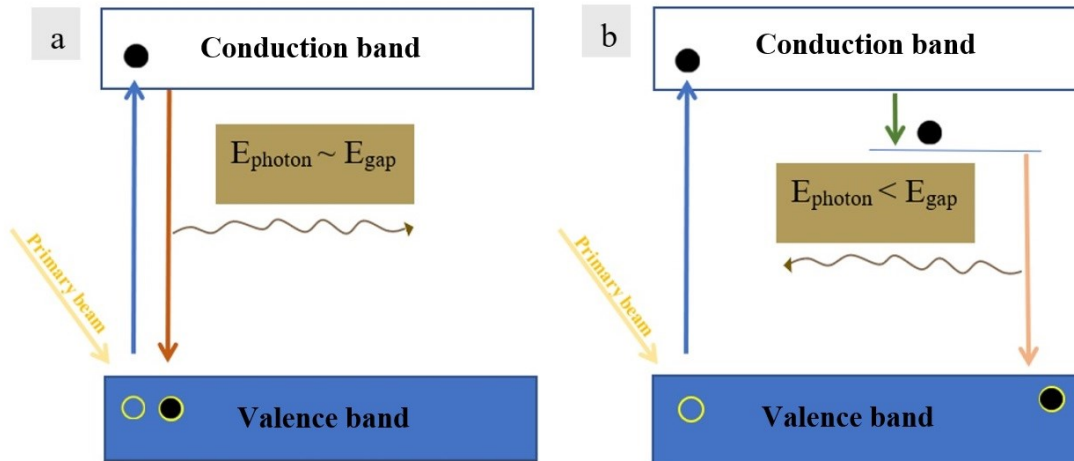
### 3.1.3. Cathodoluminescence (CL)

CL happens as a result of inelastic scattering of the electron beam with luminescent materials. These materials are insulators or semiconductors that have an electronic structure with a filled valence band separated by a gap of forbidden energy states from the empty conduction band (for  $T=0$  K).[38] The energy of CL is in the range of less than 10 eV (infrared, visible, and ultraviolet light). Over a sample area, the CL gets detected from the whole interaction volume, which results in an image with a low spatial resolution. The spatial resolution of the CL mode is thus limited by the beam penetration range in the specimen.[42] CL spectroscopy enables characterization of the optical and electronic properties of materials with a spatial resolution of the order of 1  $\mu\text{m}$  in a SEM which is much better than the one for PL spectra generated with a  $\mu\text{m}$ -sized light source.[42] The ability to obtain detailed depth-resolved information by modifying the electron beam energy as well as directly visualizing the defects are the advantages of the CL technique.

Luminescence emission spectra are divided into two categories, namely intrinsic (edge emission) and extrinsic (characteristic emission). Intrinsic luminescence- which happens at ambient temperature- is due to the recombination of free electrons and holes.[42] The most likely energy transitions in materials with a direct band gap happen between the minimum of the conduction band (highest probability of filled states) and the maximum of the valence band (highest probability of unoccupied states). Fig.3.6.a shows the schematic of an intrinsic CL emission. When the electron beam excites one electron from the valence band, a hole will be created in the valence band. After another electron relaxes and fills the hole, a photon can be emitted which has an energy equal to the energy of the band gap of the material.[38]

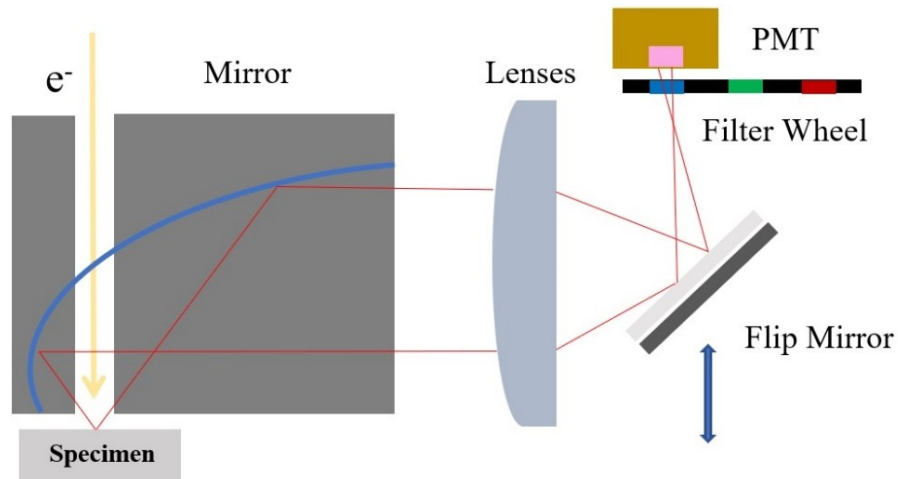
Extrinsic CL, on the other hand, depends on the presence of impurities.[42] These impurities influence the emission spectra in both direct and indirect semiconductors.

Fig.3.6.b represents an extrinsic CL emission. Certain impurity atoms lead to the creation of allowed energy states within the bandgap.[38] When the energy relaxation happens, the electron goes first to the impurity level and loses parts of its energy. In the subsequent transition, the electron will reach the valence band and fills the hole. In this case, the energy of the emitted photon is less than the energy of the band gap.[38]



**Figure 3.6** Scheme of (a) intrinsic CL generation (b) extrinsic CL generation. Adapted from [38]

Inside the electron microscope, the optical radiation is collected by a parabolic mirror placed between the electron beam and the specimen (see Fig.3.7). A lens is used to focus the light towards the detector. The collected radiation is measured with a photomultiplier tube (PMT). The spectrometer can be operated in two different modes, namely panchromatic imaging and spectral mode. CL images are observed by panchromatic imaging. In this mode, the CL signal is the average over all wavelengths within the detection range and displayed across the scanned area. Regions with high emission appear bright on the CL image. Emission spectra are acquired in spectral mode on a specific region and then displayed for one selected position of the electron beam. By using PMT and a filter wheel, intensity mapping becomes possible. The spectral resolution in CL measurements depends on the material's luminescence efficiency, temperature, and sensitivity of the CL detection system.[42] More intense and narrower luminescence lines are achieved at liquid helium temperatures.[42]



**Figure 3.7** Schematic drawing of the optical path of the CL setup. Using a flip mirror, the CL emission is directed towards the PMT. Modified from [43]

### 3.1.4. Transmission electron microscopy (TEM)

Having a beam of high-energy electrons (100-300 keV) -modern TEM can go as low as 60 or even 30keV-, and smaller interaction volume in TEM samples (less than 100 nm), are the main reasons for obtaining images with higher spatial resolution in TEM compared to SEM. In TEM, the specimen is illuminated by a parallel electron beam and only the elastically scattered electrons (non-deflected) are used for imaging. The TEM is multi-modal - other modes can be used depending on which information about the sample is required. In this work, selected area electron diffraction (SAED), bright field (BF), dark field (DF), and HRTEM imaging are used. In the following, the basic concepts of these modes are briefly explained. Fig.3.8 shows the construction of a TEM and the different modes for imaging and diffraction.

Inside a TEM column, electrons are generated with an electron gun consisting of two parts, namely the emitter and accelerator. The emitter can be any of these types: thermionic emitter (usually heated W or LaB<sub>6</sub>), cold field emission gun or CFEG (applied high electric field to extract e<sup>-</sup>), or a Schottky emitter (mixture of high temperature and high electric field). The reason to use hot sources is to prevent source contamination and keep tunnelling high. Depending on which type of gun is used inside the electron microscope, different energy spread and total brightness are achieved. In general, FEGs have a much narrower energy spread than thermionic sources, which benefits chemical analysis. Electro-magnetic lenses are used inside the electron microscope. The focal length of these lenses can be adjusted by changing the current in the magnetic coil.

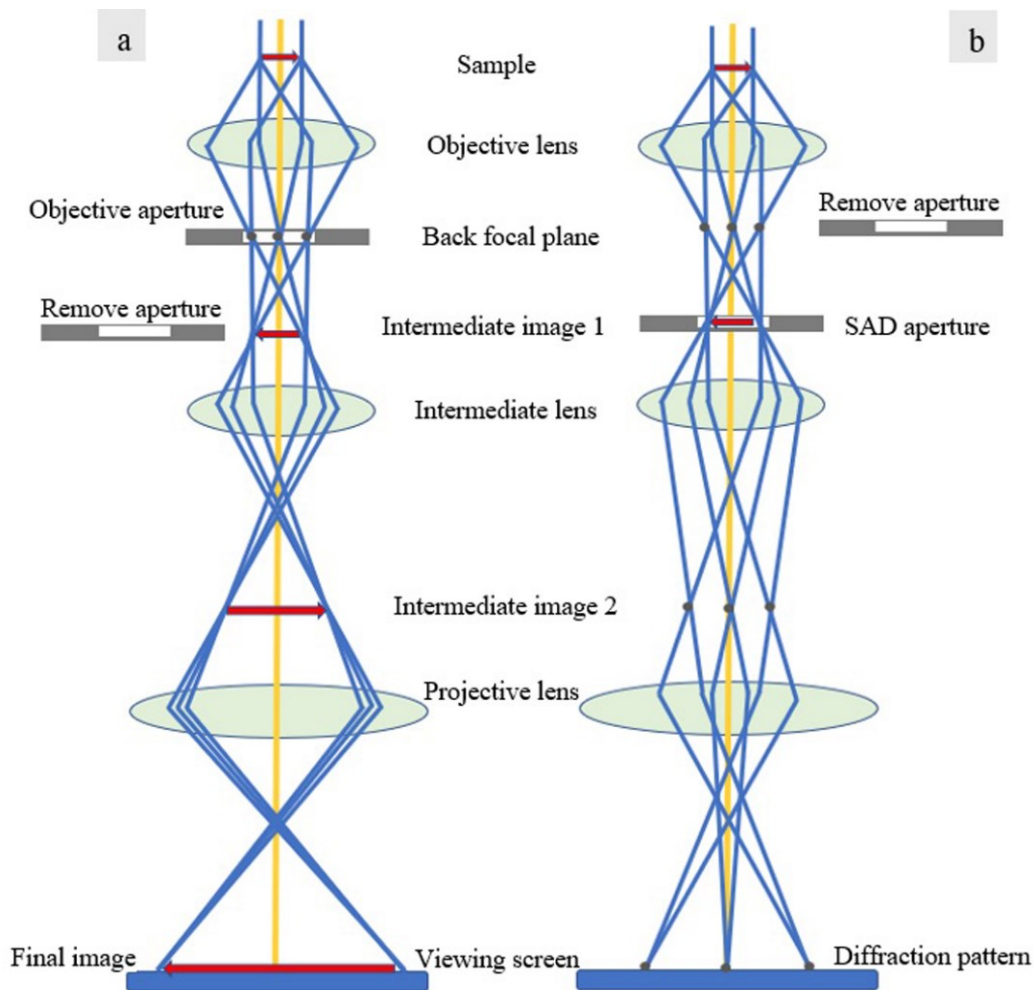


**Figure 3.8** Schematic ray diagram showing (a) image mode and (b) diffraction mode in TEM. The drawing is redrawn from [36]

The condenser lens system and apertures control the size and current of the beam. The objective lens is the first lens through which the electrons pass after their interaction with the specimen. This lens is important as it determines the image quality (resolution, contrast, etc). The objective is usually surrounding the specimen. In TEM, condenser lens astigmatism, objective lens astigmatism, spherical aberration and chromatic aberration are the main types of lens imperfections. Spherical aberration is caused when electrons travel at a large distance from the optical axis and bend strongly due to the lens magnetic field compared to those rays near the centre. Thus, instead of a point all the rays form a disk. The other type of aberration is related to chromatic aberration which arises because electrons with slightly different energies will focus at different locations. Astigmatism occurs when the electrons pass by a nonuniform magnetic field around the optic axis. As a result, the beam has an oval shape instead of having a circular shape. All these aberrations can get corrected using stigmators or aberration correctors for the spherical aberration or

chromatic aberration. Nowadays,  $C_s$  correctors are more available than chromatic aberration coefficient ( $C_c$ ) correctors. Besides the lens system, there are apertures located in the electron column of the microscope. The most important apertures are objective aperture and selected area diffraction (SAD) aperture. Objective aperture is located where the back focal plane of the objective lens is, and SAD is placed at the image plane of the objective lens where the first intermediate image is formed (see Fig.3.8). By changing the focal length of the intermediate lens, the back focal plane of the objective lens is imaged onto the screen and a diffraction pattern of the sample is observed (diffraction mode). In imaging mode, the image plane of the objective lens is viewed on the screen/ camera.

### 3.1.4.1. Electron diffraction

When the electron beam passes through the specimen, due to the Coulomb potential of the atom the electrons path will be affected. However, as they will lose no energy, this scattering event is considered elastic.

In the case of a crystalline material, the scattered electrons have specific path differences in all scattering directions. Constructive interference can happen only if the path difference is an integer multiple number of the wavelength ( $\lambda$ ). Bragg equation specifies the conditions for constructive interference for a lattice distance, ( $d_{hkl}$ ) occurring in a specific scattering angle  $\theta$  (equal to  $2\theta_{Bragg}$ )[36]:

$$2 \cdot d_{hkl} \cdot \sin(\theta_{Bragg}) = n\lambda \quad (3.3)$$

$n$  is the diffraction order.

Although the angle of scattering may change, the magnitude of the diffracted beam wave vectors does not change. Thus, the magnitude of diffracted wave vector as  $|\vec{k}|$  will be equal to the incident electron beam wave vector  $|\vec{k}_0| = 1/\lambda$ . In reciprocal space, all possible scattering wave vectors with the same magnitude will form a sphere, called the Ewald sphere. When the surface of the Ewald sphere intersects with a reciprocal lattice point, the plane corresponding to that spot is at the exact Bragg condition, which leads to a strong reflection spot. Therefore, each spot in the diffraction pattern relates to a point of the reciprocal lattice and thus to a specific plane (hkl). The Ewald sphere changes as a function of voltage in the TEM. Ewald sphere size increases as voltage increases.

Since the reciprocal lattice is the Fourier transform (FT) of the real lattice, reciprocal lattice spots of that of the selected area of a TEM sample have specific position. Size and shape of the objects in the sample or the sample itself affect the shape of the spot. If the selected region has a disk shape, the reciprocal lattice spots are elongated (so called relrods). Due to this, the Ewald sphere can intersect with more than one relrod simultaneously. Therefore, many diffraction spots appear on each diffraction pattern.

#### **3.1.4.2. BF and DF imaging**

BF and DF imaging are two basic techniques to form amplitude-contrast images. BF and DF images are formed by selecting the direct or scattered beam, respectively. To select a specific diffracted or direct beam in a TEM, objective aperture is used. An aperture is used to enhance the contrast and physically block the contribution of electron beam to the image. The size of the aperture allows only the selected electrons to pass and contribute to the image and thus define the contrast.

In the case of a BF image, the objective aperture is located at the central beam. As a result, in a BF image, thinner or lower-mass areas will appear brighter. However, thicker or higher-mass areas (high  $Z$ ) will appear darker, as the corresponding more strongly scattered electrons are blocked by the objective aperture and do not contribute to the forward scattered information. On the other hand, for DF imaging, the aperture is located around a Bragg diffracted beam. Hence, contrary to BF imaging, only the strong scattering parts which would be the crystalline areas in the specific orientation will appear bright. And the rest will appear dark. To prevent lens aberration, the incident beam is tilted such that the diffracted beam is parallel to the optical axis.

#### **3.1.4.3. HRTEM imaging**

To be able to interpret an HRTEM image, it is vital to understand the wave approach to electron scattering. In HRTEM, a parallel illumination is used and the electrons are assumed to all arrive at the sample simultaneously and scatter elastically and coherently. It can be considered as an interference pattern of the direct beam and all scattered beams. When the electron beam travels through the specimen, after the electrons interact with the crystal field of the sample, the phase of the incoming plane wave is shifted. The electron wave that leaves the specimen is named the exit wave. The exit wave function ( $\Psi_0(\vec{r})$ ) with a particular phase ( $\varphi$ ) has all information about the specimen. For a thin specimen assuming



the weak phase approximation (meaning a constant amplitude ( $A$ ) but a changing phase),  $\Psi_0(\vec{r})$  can be defined by Equation 3.4.[36]

$$\Psi_0(\vec{r}) = A(\vec{r}) \cdot e^{i\varphi(\vec{r})} \quad (3.4)$$

When the exit wave passes through the microscope, further modulation of the electron wave due to the aberration of the lens system occurs. Considering the spherical aberration coefficient of the electron source ( $C_s$ ) and the defocus to form the image ( $\Delta f$ ), the spatial frequencies ( $u$ : also defined as a vector (in  $\text{nm}^{-1}$ ) in reciprocal space) are not transferred with the same contrast. For different defocus values, the contrast transfer function (CTF) is different. The CTF describes how the phase is transferred within the lens system and thus explains the oscillation of the contrast. For a weak phase object it is given by equation 3.5:

$$CTF = \sin\left(\pi\Delta f\lambda u^2 + \frac{\pi}{2}C_s\lambda^3 u^4\right) \quad (3.5)$$

Here  $\lambda$  is the wavelength of the electron defined by the acceleration voltage, other variables were introduced before.[36]

As shown in Fig.3.9, when there is a large band (between 0 and less than  $5 \text{ nm}^{-1}$  in the example), the information is transmitted well and when the CTF is zero there will be no information transferred. At the first zero crossing, no contrast transfer exists. After that, CTF is oscillating. As a result, the contrast will change from positive to negative. This leads to images that are difficult to interpret.

To compromise for the width and value of the CTF by choosing a particular negative value of  $\Delta f$ , the first zero-crossing can be shifted to a higher  $u$ . This optimum value is defined by Eq.3.6 and is known as Scherzer defocus ( $\Delta f_{Scherzer}$ ). The first zero-crossing at  $\Delta f_{Scherzer}$  determines the maximum point resolution of the microscope.[36]

$$\Delta f_{Scherzer} = -1.2\sqrt{C_s \cdot \lambda} \quad (3.6)$$

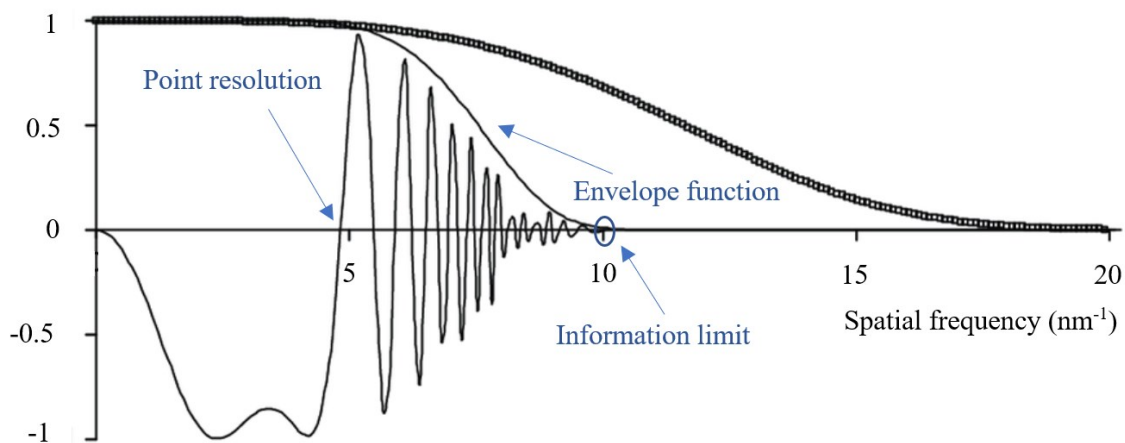


**Figure 3.9** Schematic diagram of CTF at  $C_s= 1.3$  mm,  $\Delta f= -59$  nm and collection angle= 0.2 mrad. The thick line shows the CTF multiplied by the damping envelopes: spatial (thin line) and chromatic (squares). The graph is drawn for an uncorrected TEM at the Scherzer condition. Reproduced with permission from [44]. © The Royal Society of Chemistry 2015

Within this range, a nearly intuitive image interpretation (black atoms on a white background) is possible. However, for a detailed interpretation of HRTEM images in order to know the exact atomic positions, simulations and image processing schemes are needed.[45]

The damping of the higher spatial frequencies because of not having perfect coherency for the electron source and chromatic effects will also limit the resolution. When the envelopes (shown in Fig.3.9) cut completely the CTF, no more information can be obtained out of the microscope and this is called the information limit. Using a microscope equipped with a  $C_s$  corrector is beneficial as it brings together the point resolution (first zero crossing) and information limit.

#### 3.1.4.4. Negative $C_s$

Typically, where the CTF is negative, atomic positions appear dark on a bright background.[45–48] On contrary, in the negative spherical aberration imaging (the contrast is due to imaging under negative spherical aberration conditions), the image has an enhanced contrast with bright atoms on a dark background. This enhanced contrast is due to contributions of both amplitude and phase contrast. The amplitude contrast increases at the atomic positions of the specimen. And that leads to bright atom contrast at these

positions. Furthermore, the diffraction channelling effect reduces the electron density in between the atom positions causing a dark background.[45] Negative spherical aberration imaging is due to overcompensation of spherical aberration of the objective lens.[45] This technique is only available in instruments with spherical aberration corrector for the objective lens.

The plot of CTF (solid line) for negative  $C_s$  conditions in an aberration-corrected TEM is shown in Fig.3.10. The region of optimized contrast increases to the information limit  $u$ . The imaging  $C_s$  corrector is placed between the post corrector lens and the magnifying objective mini-lens doublet.[48]

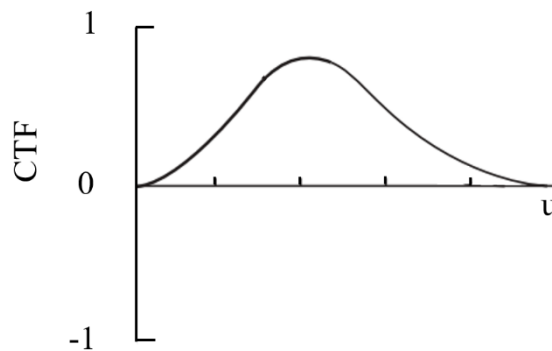


**Figure 3.10** Phase contrast transfer function as a function of spatial frequency ( $u$ ) for negative  $C_s$  conditions. Adapted from [45]

### 3.1.5. Image simulations

As mentioned before, simulations and image processing techniques are vital in order to have a detailed interpretation of HRTEM images or to know the exact atomic positions. It is not possible to trace back from the experimental image to the atomic structure due to the phase information loss. In particular, for thicker samples or larger  $C_s$  values. Instead, with the help of the software, the image of a crystal (a perfect crystal or with containing defects) is simulated and then it is compared with the experimental image. However, as one of the pitfalls of this method, the sensitivity of the image due to several factors (defocus value of the objective lens, the correct alignment of the beam with respect to the specimen and the zone axis, coherency of the beam, etc.) can be mentioned.[36]

### 3.1.5.1. Multislice method

The most basic method which is used in many of the simulation software is called the multislice method. In this method, the specimen will be divided into different slices. These slices are all normal to the electron beam. The crystal potential of each slice is projected onto a plane which is located usually on top/bottom or middle of the slice. These projected potential planes are called phase grating. Due to the interaction of the beam with the slices which is not the same for different slices (as each beam gets diffracted in a different direction), multiple beams are generated. The phases and the amplitudes of these beams on each slice are calculated separately. The process is shown in Fig.3.11.

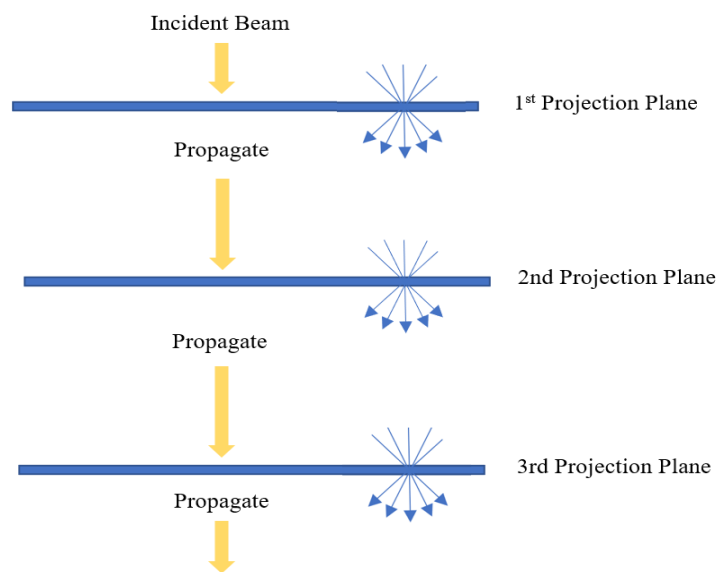


**Figure 3.11** Schematic illustrating the multislice method. The amplitudes and phases are calculated for all the beams generated due to interaction with the first phase grating plane. Then the process is repeated for the diffracted beams through free space to the next projected potential plane. Adapted from [36]

Since all the beams passing from any grating will be incident on the next grating and so on, not only Bragg beams but all of the directions should be taken into account. Eq.3.7 describes the process for the multislice method:

$$\psi_{n+1}(K) = [\psi_n(K)P_{n+1}(K)] \otimes Q_{n+1}(K) \quad (3.7)$$

Here,  $\psi$  is the electron wave.  $P$  is the propagation of the electron wave in free space related to the microscope, and  $Q$  is the phase grating describing the specimen.  $\psi_{n+1}(k)$  represents

the wave function in reciprocal space at the exit of the  $n+1$  slice and the symbol  $\otimes$  is the sign for convolution.[36]

Since the three functions  $\psi(k)$ ,  $P(k)$ , and  $Q(k)$  are all functions in reciprocal space, this approach is called the reciprocal-space formulation.[36]

### 3.1.6. Scanning transmission electron microscopy (STEM)

In contrast to the TEM mode, where a parallel illumination is used, in STEM mode the beam is changed into a focused and convergent beam. Similar as in a SEM, the electron beam rasters over the sample which leads to various signals at each point. These signals are coming from the transmitted electrons passing through the sample which get scattered at different angles in all directions. The scattered electrons are afterward recorded with different annular detectors. These detectors are categorized by the angular range (schematically displayed in Fig.3.12). By changing the camera length  $L$ , the detectable angles can be altered even more specifically. The electrons which are elastically and inelastically scattered in forward direction (with  $\theta_1 < 10-25$  mrad) are collected with the annular bright-field (ABF) detector. ABF and BF TEM images share the same contrast mechanism. The next detector is annular dark field (ADF) detector. This detector collects coherent, elastically scattered electrons in an angular range of  $25 < \theta_2 < 50$  mrad. As mentioned in previous section, in DF TEM mode, only one diffraction spot is used for image formation. However, in ADF STEM the contrast results from all scattered electrons that fall on the detector.

The last detector is the high angle annular dark-field (HAADF) detector which detects the electron in the range  $\theta_3 > 50$  mrad and collects only the incoherent, elastically scattered electrons (Rutherford scattering). For the HAADF images, the contrast mechanism is typically mass-thickness contrast, and the observed brightness is dependent on the atomic number  $Z$ , with contrast approximately proportional to  $Z^2$ . As a result, heavy elements with a higher  $Z$  look bright in the HAADF STEM images. In contrast, the lighter elements will appear dark.

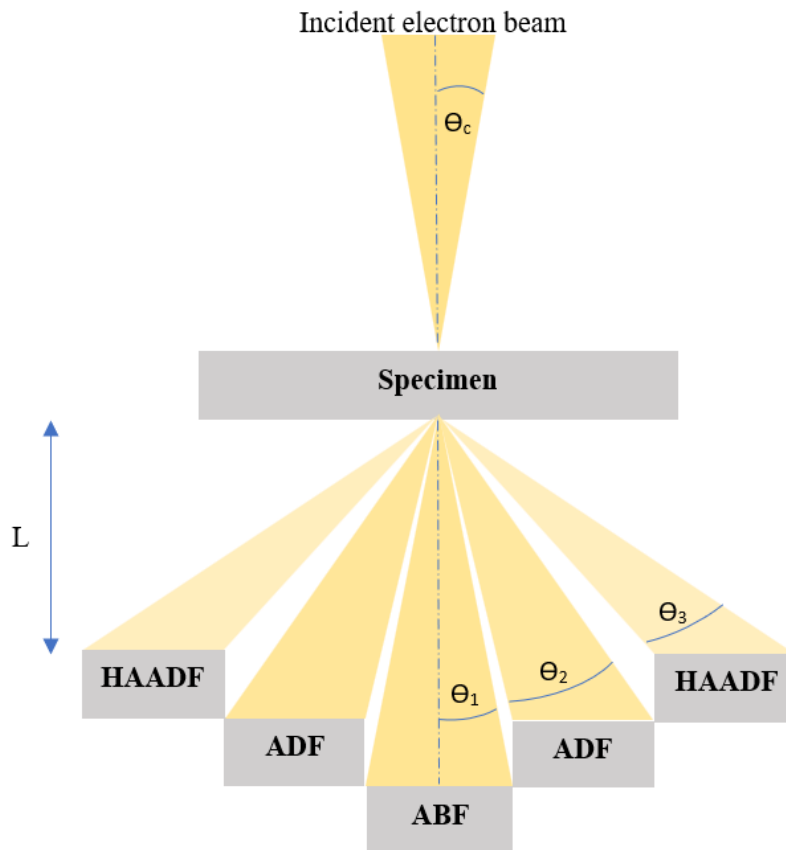


**Figure 3.12** Schematic diagram of STEM different annular detectors. ABF stands for annular bright field, ADF is annular dark field and HAADF represents the high angle annular dark field. Modified from [36]

The resolution of the STEM images is dependent on both the diameter of the incident beam and the specimen thickness. With the help of aberration correction, the resolution can be improved to lower 100 pm. The STEM Cs corrector is placed at the condenser lens and the demagnifying doublet that is composed of condenser mini-lens placed above the objective lens.[48] It is used to generate an electron beam with a size down to 0.8, which is scanned across the sample. Another crucial factor is related to the semi-convergent angle which was set at 23.5 mrad by default in this thesis.

## 4. Correlation between structural studies and the cathodoluminescence of individual complex niobate particles

This chapter is based on the publication by Changizi, R.; Zhang, S.; Ziegler, C.; Schwarz, T.; Lotsch, B.; and Scheu, C.; published in ACS Appl. Electron. Mater. 2021, 3, 461–467. Complex niobates, namely PrNbO<sub>4</sub> and Pr<sup>3+</sup>: Ca<sub>2</sub>Nb<sub>2</sub>O<sub>7</sub> and the effect of the crystal structure and lanthanide ions' surroundings on the width of the emission lines are analyzed in detail. All images and tables in this chapter are reproduced with permission from ACS journal.[49] Further permission related to the material excerpted should be directed to the ACS.

### 4.1. Literature review

Trivalent lanthanides (Ln<sup>3+</sup>) have a specific configuration of inner shell 4f orbitals, from which electronic transitions arise. As the 4f orbital is very well shielded from any coupling with other ligands by the outer filled 5s and 5p orbitals, these materials have magnetic and optical properties.[50,51] Laporte rule states that f-f transitions are forbidden, however, according to the crystal field theory, due to the influence of the coordination geometrical symmetry around the lanthanide ion, these transitions become partially allowed.[52] The Judd-Ofelt theory explains how the crystal field perturbs the orbitals of the lanthanide ion. This perturbation causes mixing of the orbitals with different parities, and as a result, the forbidden f-f transition becomes partially allowed.[23,24,53] In order to achieve emission spectra with high intensity and sharp emission lines, different factors such as doping concentration, the ionic radii mismatch to the host and different lattice sites for the lanthanide ions have been investigated.[54,55] Morais Faustino et al.[55] have shown that increasing the doping concentration of Eu<sup>3+</sup> to a certain amount optimizes the emission intensity. However, increasing the concentration more than the optimum amount leads to emission quenching which is caused by non-radiative energy transfer between Eu<sup>3+</sup> ions. The optimum concentration of Eu<sup>3+</sup> dopants changes remarkably with the type of host material, synthesis conditions, etc.[55] Furthermore, the authors suggest that due to the mismatch of ionic radii, the doping mechanisms play a crucial role for the formation of defects within the host. In another work, Krishnan and Swart studied the influence of different doping concentrations on the CL properties of a series of monoclinic phase BaY<sub>2</sub>(MoO<sub>4</sub>)<sub>4</sub>

phosphor powders doped with  $\text{Eu}^{3+}$ . [56] They have concluded that not only by increasing the doping content but also with a deeper penetration depth of the incident electrons, the CL intensity increases linearly. [56,57]

During the past few years, several studies have been done on different lanthanides doped into various hosts. [51,58–65] Great attention has been paid to oxide-based materials doped with  $\text{Ln}^{3+}$ . [66,67] Nico et al. [58] have suggested to use niobates as the host. Commonly, rare earth (RE) niobates have been considered as host matrices and have also attracted interests as potential rare earth-doped laser hosts. [54] The  $\text{RENbO}_4$  phases are known to crystallize in a fergusonite-type crystal structure, i.e. in a monoclinic crystal structure. [58]

Many applications for the lanthanide doped materials in the field of optoelectronic devices such as LEDs, lasers and optical amplifiers have been suggested. [59,66–69] Lanthanide doped niobates are interesting materials in the field of photorefractive memories and as linear and self-frequency converter solid state laser materials. [54,60,70]

Although there exist many studies on lanthanide doped oxides, it is interesting that, to our knowledge, no report has been published that deals with correlating optical, structural and chemical properties. Even studies with CL, lack this correlation.  $\text{Pr}^{3+}$  has attracted a lot of attention due to its efficiency of emitting photons from the UV to infrared (IR) spectral regions. [64] And there are versatile applications for lanthanide doped niobates. [54,60,70] Therefore, in the present study, we demonstrate for  $\text{Pr}^{3+}$  doped niobate powders the importance to study individual particles. Their crystal structure and chemical composition are investigated by electron microscopy and the results are correlated with their optical properties measured by CL.

## **4.2. Experimental details**

### **4.2.1. Preparation of complex niobates powder**

$\text{Pr}^{3+}$  doped  $\text{KCa}_2\text{Nb}_3\text{O}_{10}$  were synthesized in a solid-state route according to protocols modified from those reported in the literature. [25] For preparation of  $\text{Pr}^{3+}$  doped oxides, a desired amount of  $\text{K}_2\text{CO}_3$ ,  $\text{CaCO}_3$  and  $\text{Nb}_2\text{O}_5$  were mixed together with  $\text{Pr}_6\text{O}_{11}$ . This mixture was then grinded and heated to temperatures between 1100-1300°C. After washing all products in deionized water, they were dried at room temperature. 20 at% excess of  $\text{K}_2\text{CO}_3$  and  $\text{CaCO}_3$  was added to the compounds, in order to compensate for evaporation losses during heating. Pr with high amount of concentration [ $x=0.75$ ] was doped into  $\text{KCa}_2\text{Nb}_3\text{O}_{10}$



particles to reach the nominal formula  $\text{Pr}_x\text{K}_{1-x}\text{Ca}_{2-x}\text{Nb}_3\text{O}_{10}$ . However, later characterization determined that this was not the case and instead, complex niobates were produced as a result of this reaction.

#### 4.2.2. Characterization methods

XRD data of powders were collected using a Huber G670 Guinier imaging plate diffractometer (Huber, Rimsting; Cu  $\text{K}_{\alpha 1}$  radiation,  $\lambda = 154.051$  pm, Ge (111)-monochromator). The particle morphology was analyzed by an Auriga Zeiss SEM equipped with an in-lens detector and coupled with EDX for composition analysis. Elemental quantification was done using the ZAF quantification method by the Team software. Secondary electron images and EDX data were acquired at 10 keV. CL data were recorded using FEI Helios Nanolab 600 equipped with a paraboloidal mirror, MonoCL4 monochromator (acquisition software Gatan DigitalMicrograph®) and a liquid  $\text{N}_2$  cooled Hamamatsu photomultiplier tube R5509-73. The sample powders were irradiated with an electron beam of 10 keV and beam current of 5.5 nA. Furthermore, crystal structure analysis of individual particles was done using a Thermo Fisher Scientific Titan TEM operated at 300 kV, equipped with an X-FEG (extreme field emission gun) as electron source and an aberration corrector for the objective lens. For SEM investigations, the powder was dispersed on a Si substrate, while for TEM an Au-finder grid coated with a continuous carbon film was used.

### 4.3. Results and discussions

#### 4.3.1. EDX and XRD data of powder

EDX measurements of powder show Ca, Pr, Nb and O with the corresponding average composition 5.3 at%, 5.9 at%, 10.3 at% and 78.4 at%. The values are average values of three EDX measurements taken over a size of several hundred microns. No K was detected. This indicates that K is evaporated and not incorporated into the lattice for such a high amount of Pr. Fig.4.1 compares the XRD patterns of the pure  $\text{KCa}_2\text{Nb}_3\text{O}_{10}$  powder with the  $\text{Pr}^{3+}$  doped compounds.

The XRD pattern of the synthesized Pr doped material (red pattern in Fig.4.1) does not fit to the monoclinic crystal structure of  $\text{KCa}_2\text{Nb}_3\text{O}_{10}$ , as only a few reflections occur at similar  $2\theta$  values. Instead all reflections can be explained by the presence of two other phases. One is  $\text{PrNbO}_4$ , which has also a monoclinic crystal structure (space group:  $\text{C2/c}$ ) with lattice parameters  $a = 5.499$  Å,  $b = 5.157$  Å,  $c = 11.342$  Å and  $\alpha = 90^\circ$ ,  $\beta = 94.57^\circ$ ,  $\gamma = 90^\circ$  (ICSD

109176). The reference pattern is shown in green in Fig.4.1. The peaks at  $2\theta = 33.95^\circ$ ,  $48.9^\circ$  and  $57.96^\circ$  do not belong to  $\text{PrNbO}_4$  but match to the cubic crystal structure of  $\text{Ca}_2\text{Nb}_2\text{O}_7$  (ICSD 72206). The pure, cubic  $\text{Ca}_2\text{Nb}_2\text{O}_7$  (space group:  $Fd-3m$ ) has a lattice parameter  $a = 10.445 \text{ \AA}$ . The reference pattern of this phase is displayed in blue in Fig.4.1 and shows slightly shifted peaks at  $2\theta = 34.31^\circ$ ,  $49.31^\circ$  and  $58.55^\circ$ . Other peaks of this phase partly overlap with the one of the  $\text{PrNbO}_4$  phase. The peaks which are slightly shifted to lower  $2\theta$  values indicate an increase in the interplanar spacing. In this coordination geometry, ionic radii of Ca and Nb are  $1.12 \text{ \AA}$  and  $0.64 \text{ \AA}$ , respectively. When Nb is replaced by Pr the ionic radius changes to  $0.99 \text{ \AA}$ . Therefore, the increase in the interplanar spacing is most likely due to the Pr ions sitting on Nb sites within the  $\text{Ca}_2\text{Nb}_2\text{O}_7$  crystal lattice, e.g. a Pr doped  $\text{Ca}_2\text{Nb}_2\text{O}_7(\text{Pr}^{3+}: \text{Ca}_2\text{Nb}_2\text{O}_7)$  phase has formed. We have calculated this crystal lattice strain which is 0.5 %. The XRD results thus indicate that during the synthesis two phases were formed.

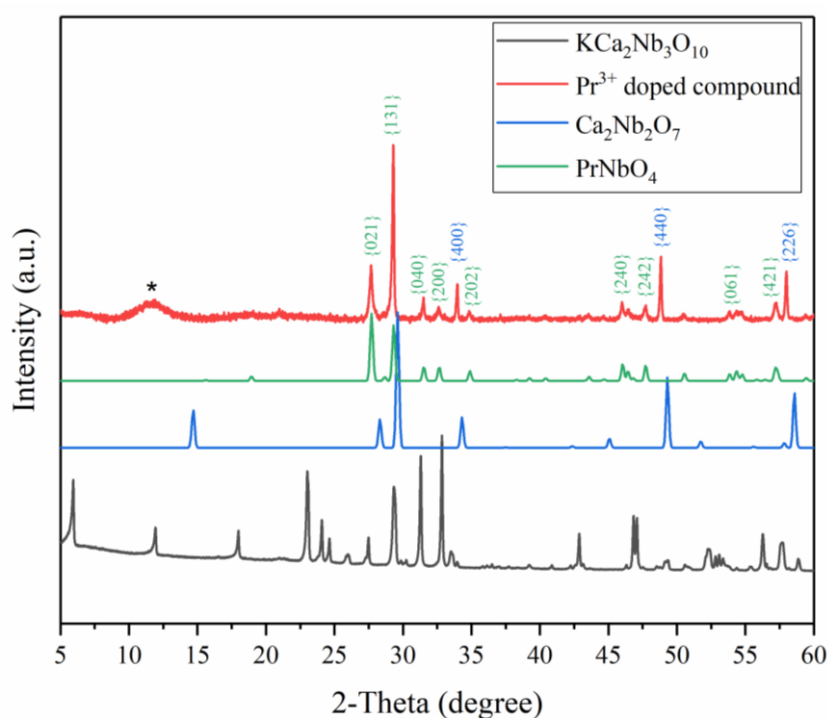


**Figure 4.1** XRD pattern of  $\text{Pr}^{3+}$  doped compound (red curve) in comparison with the reference  $\text{KCa}_2\text{Nb}_3\text{O}_{10}$  (black curve),  $\text{Ca}_2\text{Nb}_2\text{O}_7$  [ICSD 72206] is shown in blue and  $\text{PrNbO}_4$  [ICSD 109176] is indicated in green. (\*) mark shows an instrumental artefact.

It is worth mentioning here, that according to [55], multiple sites exist in the lattice of lanthanide doped materials which were studied by the visible emission bands of the  $\text{Ln}^{3+}$ .

For example, after investigating the local structure around the  $\text{Ln}^{3+}$  dopants, it was found that  $\text{Ln}^{3+}$  ions enter the  $\text{ABNbO}_3$  structure with A and B being alkali and alkaline earth metals not only by substituting A and B, but also by substituting Nb lattice positions.[54] Similarly, in our sample not only the K of  $\text{KCa}_2\text{Nb}_3\text{O}_{10}$  is completely replaced, but Ca and Nb are partly replaced by Pr.

#### **4.3.2. Elemental analysis (EDX) of individual particles**

As the XRD data indicated the presences of two phases,  $\text{Pr}^{3+}:\text{Ca}_2\text{Nb}_2\text{O}_7$  and  $\text{PrNbO}_4$ , it was important to obtain EDX data of individual particles to correlate the chemical composition and the corresponding CL spectrum. The EDX spectra for two selected particles are shown in Fig.4.2, together with their SEM image. The particles are micron-sized. The EDX spectra proved the presence of Si, O, Nb, Ca and Pr. In accordance to the EDX measurements over the powder, no K is detected. Since low energy peaks, such as the  $\text{O-K}_\alpha$  line, cannot be quantified precisely due to the high amount of absorption by the specimen, O in addition to Si (from the substrate) and other contaminations such as F were removed from the quantification. The higher intensity of the  $\text{Si-K}_\alpha$  line in Fig.4.2.a is due to larger contributions from the substrate as the particle is thinner in this region.

EDX was performed for 21 single particles. Regarding their chemical composition, both phases were found in these particles. In phase (i) for 13 particles the elements Ca, Nb and Pr were observed with the corresponding average composition of 37.5 at%, 39.7 at% and 22.8 at% besides O.

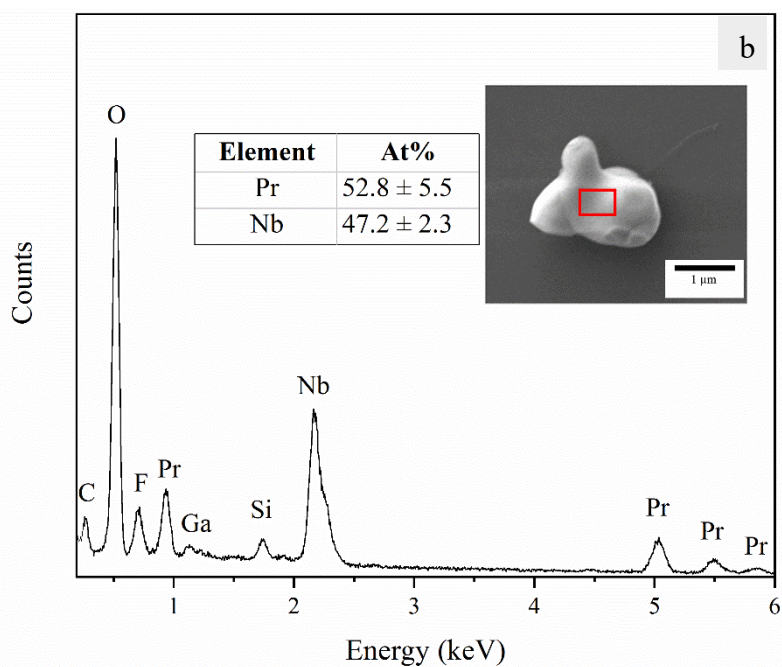
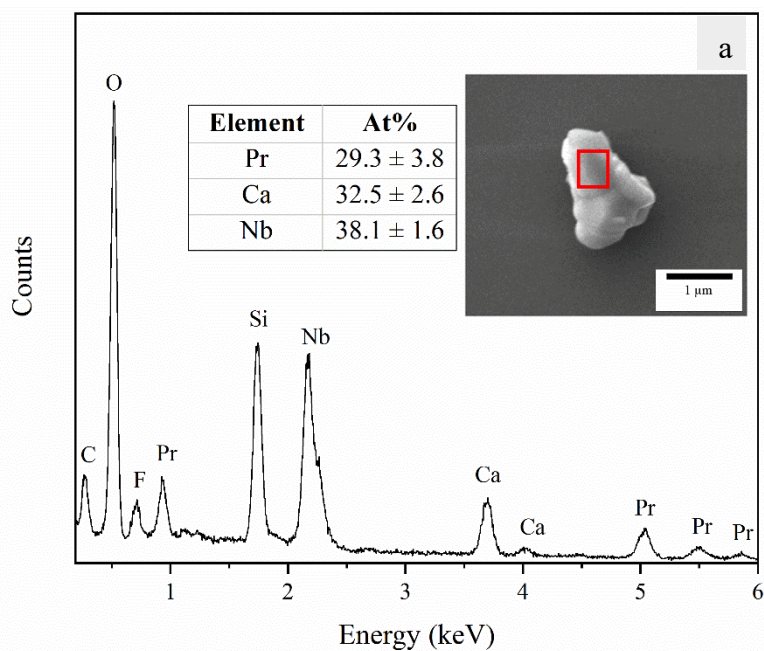


**Figure 4.2** EDX spectra of individual (a)  $\text{Pr}^{3+}:\text{Ca}_2\text{Nb}_2\text{O}_7$  and (b)  $\text{PrNbO}_4$  particles. The area where the data were acquired are indicated by a red box in the SEM image shown as inset.

By plotting the concentrations of Ca and Nb against the Pr concentration a linear dependency was found (see Fig.4.3). As a result, with a good approximation, the chemical formula was obtained as  $\text{Pr}_x\text{Ca}_{48-x/2}\text{Nb}_{52-x/2}\text{O}_y$ , the average composition of x equals to 20 at%. In

phase (ii) for 8 particles only Pr and Nb with almost constant composition of (46.4 at% for Nb and 53.6 at% for Pr) were found besides O. Comparing the ratio of Pr and Nb with the stoichiometric ratio, i.e. Pr:Nb = 1:1, it indicates that a small fraction of the Pr ions are located on Nb sites within the  $\text{PrNbO}_4$  crystal structure.

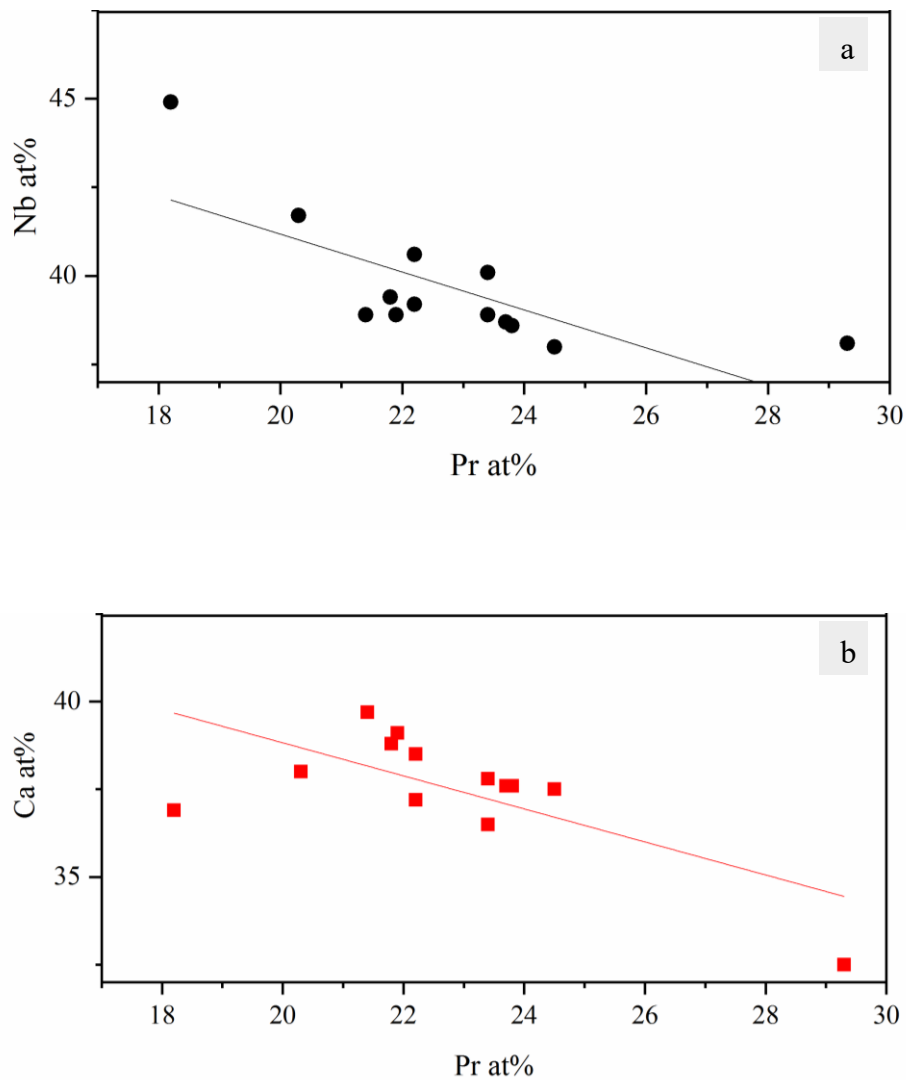


**Figure 4.3** Pr at% versus (a) Nb at% and (b) Ca at% for a set of individual nanoparticles with the formula  $\text{Pr}_x\text{Ca}_{48-x/2}\text{Nb}_{52-x/2}\text{O}_y$ .

Comparing the Pr concentration in both phases, a higher amount of Pr is found in the second phase where both Ca and K atoms are substituted by Pr. As a result, Pr is replacing K and is substituting also locally Ca and Nb. Since the measured concentrations of Pr are higher than its solubility limit in  $\text{Pr}^{3+}$  doped  $\text{KCa}_2\text{Nb}_3\text{O}_{10}$ , the aforementioned two phases are

formed during annealing. Several SEM images at different magnifications were taken of each particle. This made it possible to trace back and identify all the 21 single particles in the microscope where we did the CL measurements.

#### 4.3.3. CL properties of $\text{PrNbO}_4$ and $\text{Pr}^{3+}:\text{Ca}_2\text{Nb}_2\text{O}_7$

In order to study the optical properties of the two formed phases, i.e.  $\text{PrNbO}_4$  and  $\text{Pr}^{3+}:\text{Ca}_2\text{Nb}_2\text{O}_7$ , CL measurements of single particles were obtained. A representative CL spectrum of  $\text{PrNbO}_4$  is plotted in Fig.4.4 in black, which exhibits the following transitions  $^3\text{P}_0$  to  $^3\text{H}_4$ ,  $^3\text{P}_2$  to  $^3\text{H}_5$ ,  $^3\text{P}_1$  to  $^3\text{H}_5$ ,  $^3\text{P}_2$  to  $^3\text{H}_6$ ,  $^3\text{P}_0$  to  $^3\text{H}_6$ ,  $^3\text{P}_2$  to  $^3\text{F}_3$ ,  $^3\text{P}_0$  to  $^3\text{F}_2$  and  $^3\text{P}_2$  to  $^3\text{F}_4$ . Spectra of particles with the formula  $\text{Pr}^{3+}:\text{Ca}_2\text{Nb}_2\text{O}_7$  were also acquired. The red curve in Fig.4.4 shows one representative CL spectrum with major emission lines (higher than the noise level) which can be associated with the  $^3\text{P}_0$  to  $^3\text{H}_4$ ,  $^3\text{P}_2$  to  $^3\text{H}_6$ ,  $^3\text{P}_0$  to  $^3\text{H}_6$ ,  $^3\text{P}_2$  to  $^3\text{F}_3$ ,  $^3\text{P}_0$  to  $^3\text{F}_2$  and  $^3\text{P}_2$  to  $^3\text{F}_4$  electric dipole transitions of  $\text{Pr}^{3+}$ . All transitions were labelled according to the Dieke diagram ( $\text{Pr}^{3+}:\text{LaCl}_3$ ).[25] In comparison with the Dieke diagram, our emission lines deviate by less than  $\pm 4$  nm (see Table 4.1).

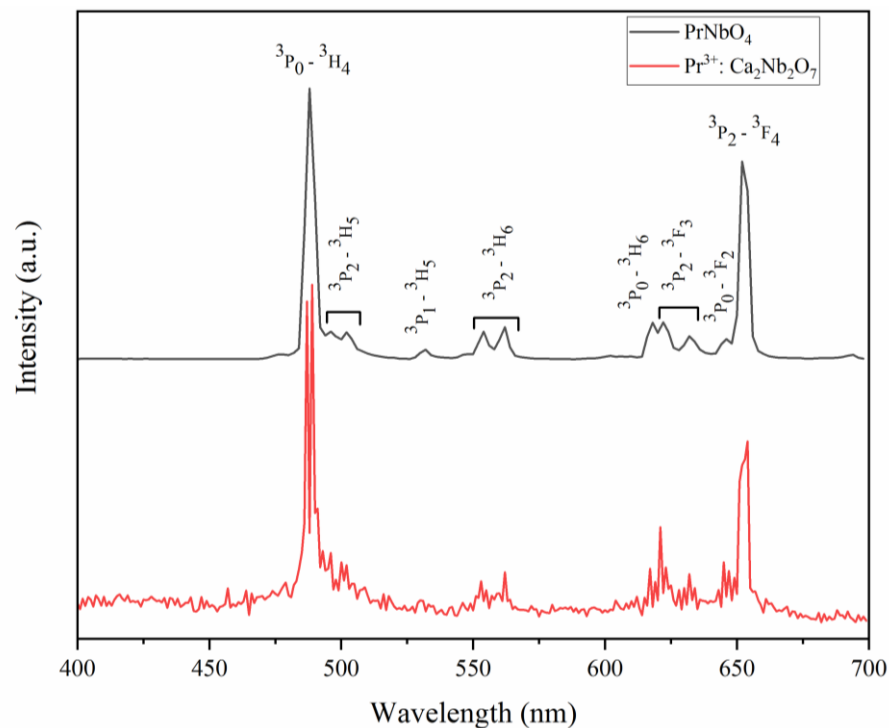


**Figure 4.4** CL spectra of  $\text{PrNbO}_4$  (black curve) and  $\text{Pr}^{3+}:\text{Ca}_2\text{Nb}_2\text{O}_7$  (red curve).

The wavelengths of each emission line are listed in Table 4.1. The strongest emission lines belong to  $^3P_0$  to  $^3H_4$  and  $^3P_2$  to  $^3F_4$  transitions, which are at 489 nm and 653 nm, respectively, in both phases. Similar main emission lines were reported for other  $Pr^{3+}$  doped systems.[70–72] Both phases show the identical wavelength values for each transition. However, the transitions belonging to  $^3P_2$  to  $^3H_5$  and  $^3P_1$  to  $^3H_5$  were not clear in Fig.4.4 for the  $Pr^{3+}$ :  $Ca_2Nb_2O_7$  phase as the related emission peaks show low intensity.

We normalized the CL spectra to their highest peak ( $^3P_0$  to  $^3H_4$ ) to 100 and the relative intensities for the other transitions are given in Table 4.2. In the spectra of  $PrNbO_4$  the intensity ratio between the dominant transitions ( $^3P_0$  to  $^3H_4$  and  $^3P_2$  to  $^3F_4$ ) is lower than for the other phase. However, the intensity ratios between the emission line originating from  $^3P_0$  to  $^3H_4$  and the remaining emissions are higher for  $PrNbO_4$  compared to the one of the  $Pr^{3+}$ :  $Ca_2Nb_2O_7$  spectrum.

**Table 4.1:** Wavelength comparison between both spectra and the Dieke diagram ( $Pr^{3+}$ :  $LaCl_3$ ), all wavelengths are in [nm]

Formula	$^3P_0$ to $^3H_4$	$^3P_2$ to $^3H_5$	$^3P_1$ to $^3H_5$	$^3P_2$ to $^3H_6$	$^3P_0$ to $^3H_6$	$^3P_2$ to $^3F_3$	$^3P_0$ to $^3F_2$	$^3P_2$ to $^3F_4$
$Pr^{3+}$ : $Ca_2Nb_2O_7$	489	Low SNR*	Low SNR*	553 562	617	621 632	645	653
$PrNbO_4$	489	495 502	531	553 562	617	621 632	645	653
$Pr^{3+}$ : $LaCl_3$	492	500	531	558	617	625	645	649

\*SNR stands for signal to noise ratio.

**Table 4.2:** Intensity comparison between both spectra, all wavelengths are in [nm]

Formula	$^3P_0$ to $^3H_4$	$^3P_2$ to $^3H_5$	$^3P_1$ to $^3H_5$	$^3P_2$ to $^3H_6$	$^3P_0$ to $^3H_6$	$^3P_2$ to $^3F_3$	$^3P_0$ to $^3F_2$	$^3P_2$ to $^3F_4$
$Pr^{3+}$ : $Ca_2Nb_2O_7$	100	—	—	16 19	19	30 18	21	55
$PrNbO_4$	100	11 11	3	11 12	15	15 9	8	65

Based on our CL results we can conclude that for each phase ( $PrNbO_4$  and  $Pr^{3+}$ :  $Ca_2Nb_2O_7$ ), depending on Pr concentration and which host element it is substituting, similar transition peaks but varying intensity ratios can be found. Depending on which site  $Ln^{3+}$  ions occupy, different transitions can be achieved.[73–76] If the active ions occupy the site with  $C_2$

symmetry (RE sites), which leads to the removal of the parity-forbidden f-f transition, a higher intensity can be observed.[60] Magnetic-dipole transitions are independent of site symmetry, whereas electric-dipole ones are only allowed at sites of low symmetry with no inversion centre.[55] Therefore, the high intensity of some peaks indicates that a significant proportion of the  $\text{Pr}^{3+}$  is located in non-centrosymmetric sites, whereas broad emission lines are related to the lower incorporation of  $\text{Pr}^{3+}$  ions into the crystal lattice. [55]

#### 4.3.4. Crystal structure analysis

To confirm that the luminescent properties of  $\text{PrNbO}_4$  are due to its chemistry and crystal structure, TEM measurements were performed on these particles. Fig.4.5.a shows a BF TEM image of a  $\text{PrNbO}_4$  particle. Since the particle thickness was very thin at the edges, the HRTEM image (see Fig.4.5.b) was taken on this area. The corresponding SAED pattern is shown Fig.4.5.c. The crystal was oriented in the  $[\bar{2}\bar{3}0]$  zone axis and for the corresponding SAED pattern we indexed the (002) and (321) and  $(3\bar{2}\bar{1})$  planes. Furthermore, we identified for the particle a monoclinic structure which agrees well with the one for  $\text{PrNbO}_4$  (ICSD 109176). The same crystal structure is reported for several lanthanide niobates systems. [58,60,77]

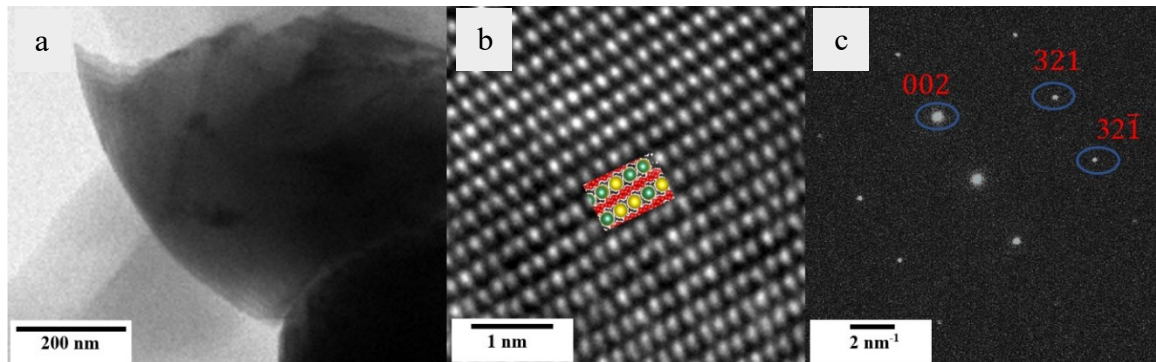
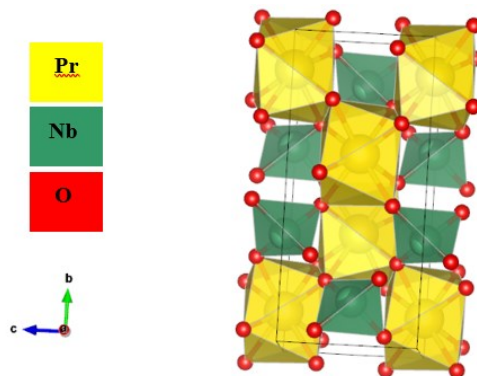


**Figure 4.5** (a) TEM of an individual particle, (b) HRTEM image; (Green spheres: Niobium, Yellow: Praseodymium, Red: Oxygen) and (c) corresponding SAED patterns of  $\text{PrNbO}_4$  in the  $[\bar{2}\bar{3}0]$  zone axis.

The structure of  $\text{PrNbO}_4$  in its monoclinic structure viewed along  $[\bar{2}\bar{3}0]$  is superimposed in Fig.4.5.b using the program VESTA ver. 3.3.2 and basic atom locations:  $\text{Pr}(0.25, 0.12, 0)$ ,  $\text{Nb}(0.25, 0.65, 0)$  and  $\text{O}(0.01, 0.72, 0.2)$ .

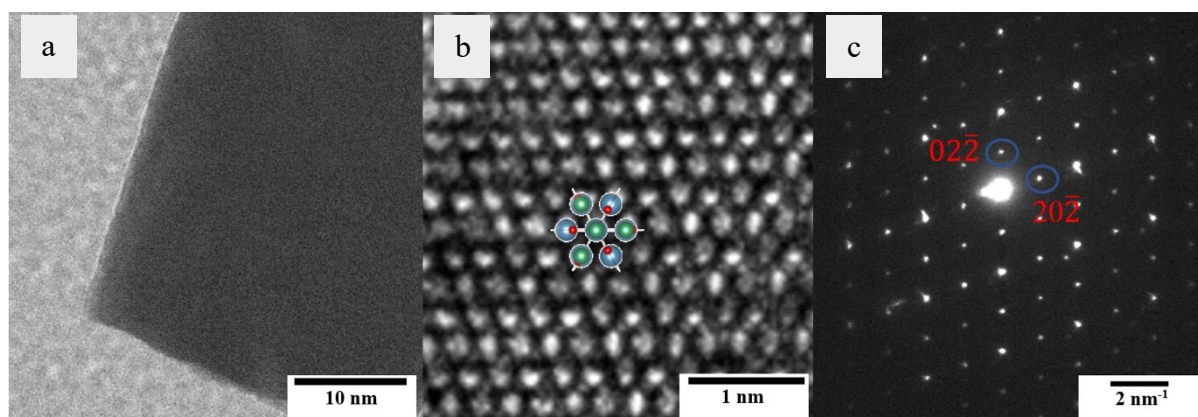


The crystal structure of PrNbO<sub>4</sub> is depicted in Fig.4.6. As shown on the figure, Pr is bonded to eight O atoms in an 8-coordinate geometry (maximum bond length: 2.74 Å). Nb in a tetrahedral geometry is bonded to four O atoms (maximum bond length: 2.45 Å).



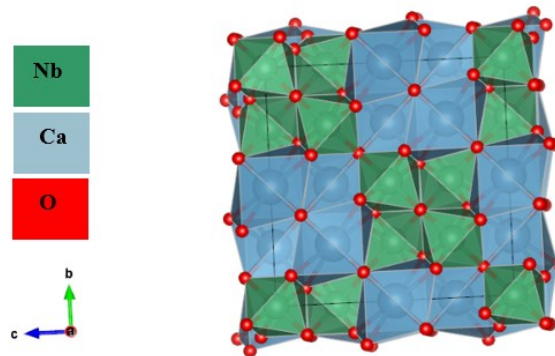
**Figure 4.6** Crystal structure of PrNbO<sub>4</sub>.

Fig.4.7.a shows the BF TEM image of the Pr<sup>3+</sup>: Ca<sub>2</sub>Nb<sub>2</sub>O<sub>7</sub>. In Fig.4.7.b a HRTEM image of the particle taken in the [111] zone axis is shown. The corresponding SAED pattern of this particle is given in Fig.4.7.c. The diffraction patterns index well to the one for Ca<sub>2</sub>Nb<sub>2</sub>O<sub>7</sub> (ICSD 72206). VESTA was used to show the structure of Ca<sub>2</sub>Nb<sub>2</sub>O<sub>7</sub> and the zone [111] which is superimposed in Fig.4.7.b. The following basic atom locations were used: Ca(0.5, 0.5, 0.5), Nb(0, 0, 0) and O(0.32, 0.12, 0.12).



**Figure 4.7** (a) TEM, (b) HRTEM image; (Blue spheres: Calcium, Green: Niobium, Red: Oxygen) and (c) corresponding SAED patterns of the Pr<sup>3+</sup>: Ca<sub>2</sub>Nb<sub>2</sub>O<sub>7</sub> phase in the [111] zone axis.

Fig.4.8 Illustrates the crystal structure of  $\text{Ca}_2\text{Nb}_2\text{O}_7$ . Ca is bonded to eight O atoms and forms a distorted  $\text{CaO}_8$  hexagonal bipyramids (maximum bond length: 2.83 Å). Nb is bonded to six equivalent O atoms to form  $\text{NbO}_6$  octahedra (maximum bond length: 2.45 Å). In case of  $\text{Pr}^{3+}:\text{Ca}_2\text{Nb}_2\text{O}_7$  particles,  $\text{Pr}^{3+}$  occupies Ca (16d) and Nb (16c) sites. To compensate for charge neutrality, Ca vacancies can form close to Pr(Ca) sites and oxygen vacancies can form around Pr(Nb) sites, similar to the mechanism described by Górecka et al. for  $\text{Eu}^{3+}$  doped  $\text{Ca}_9\text{Y}(\text{PO}_4)_7$ . [78]



**Figure 4.8** Crystal structure of  $\text{Ca}_2\text{Nb}_2\text{O}_7$

We have measured the  $d$  spacing value corresponding to the (111) plane based on the diffraction pattern of a  $\text{Pr}^{3+}:\text{Ca}_2\text{Nb}_2\text{O}_7$  particle. The  $d$  spacing in this case is 6.4 Å. According to (ICSD 72206), the  $d$  value for the same plane of  $\text{Ca}_2\text{Nb}_2\text{O}_7$  is 6.03 Å. Due to the difference that exists between these values, the chemical formula calculated for this phase and obtaining two different CL spectra for each phase, we assume that Pr should be sitting on Ca and Nb sites almost equally.

#### 4.4. Conclusion

$\text{Pr}^{3+}$  doped  $\text{KCa}_2\text{Nb}_3\text{O}_{10}$  were synthesized via a solid-state route. Complex niobates with different phases, namely  $\text{PrNbO}_4$  and  $\text{Pr}^{3+}:\text{Ca}_2\text{Nb}_2\text{O}_7$  were produced during the annealing process. Characterization of both phases was achieved by XRD, EDX, CL and TEM analysis. The main conclusions drawn from this study are summarized as follows.

1. XRD patterns of Pr<sup>3+</sup> doped compounds index well to the monoclinic crystal structure of PrNbO<sub>4</sub> and the cubic crystal structure of Ca<sub>2</sub>Nb<sub>2</sub>O<sub>7</sub>. There is a small shift in the XRD pattern of Pr doped compounds compared to the one for Ca<sub>2</sub>Nb<sub>2</sub>O<sub>7</sub>, which indicates an increase in the *d* spacing value. This confirms that Pr ions with bigger ionic radius value must occupy Nb sites.
2. In the SEM, individual micron sized particles were observed. EDX results show the presence of both phases. Based on these data, chemical formulas of the phases were calculated. In PrNbO<sub>4</sub> higher amount of Pr with the average of 53.6 at% is found as a result of both Ca and K atoms being substituted by Pr. In Pr<sup>3+</sup>: Ca<sub>2</sub>Nb<sub>2</sub>O<sub>7</sub>, Pr ions occupy both Ca and Nb sites almost equally. Average Pr content in this phase is 22.8 at%.
3. The CL data show similar transition lines but varying intensity ratios for PrNbO<sub>4</sub> and Pr<sup>3+</sup>: Ca<sub>2</sub>Nb<sub>2</sub>O<sub>7</sub>. In the spectrum of PrNbO<sub>4</sub>, brighter emission lines exist compared to the ones from the second phase. This is due to the fact that more Pr atoms are occupying sites with C<sub>2</sub> symmetry which leads to the removal of the parity-forbidden f-f transition. In both spectra major emission lines are labelled in which the dominant ones are associated with the <sup>3</sup>P<sub>0</sub> to <sup>3</sup>H<sub>4</sub> and <sup>3</sup>P<sub>2</sub> to <sup>3</sup>F<sub>4</sub> of electric dipole transition of Pr.
4. Both phases, PrNbO<sub>4</sub> and Pr<sup>3+</sup>: Ca<sub>2</sub>Nb<sub>2</sub>O<sub>7</sub>, are observed and characterized by TEM. Monoclinic crystal structure for PrNbO<sub>4</sub> and cubic structure for Pr<sup>3+</sup>: Ca<sub>2</sub>Nb<sub>2</sub>O<sub>7</sub> were observed based on the diffraction pattern for each phase and comparison with ICSD data of PrNbO<sub>4</sub> and Ca<sub>2</sub>Nb<sub>2</sub>O<sub>7</sub>.

Based on these results, lanthanide niobate compounds with brighter emission lines are better candidates in terms of luminescent efficiency and can be used in various applications.



## 5. Effects of Defect Density on Optical Properties Using Correlative Cathodoluminescence and Transmission Electron Microscopy Measurements on Identical PrNbO<sub>4</sub> Particles

The present chapter is a modified version of the paper by Changizi, R.; Zaefferer, S.; Abdellaoui, L.; and Scheu, C.; published in ACS Appl. Electron. Mater. 2022, 4, 13. In this chapter, the investigations on PrNbO<sub>4</sub> powder particles with different density of twins and the effect on the intensity of the emission lines are explained. All images and tables in this chapter are reproduced with permission from ACS journal.[79] Further permission related to the material excerpted should be directed to the ACS.

### 5.1. Literature review

Lanthanide niobates have been widely studied in recent decades. The physical properties and chemical stability of these oxides enable them to be potential laser and optical materials.[60,80,81] A large variety of lanthanide niobates exists with different stoichiometries such as RENbO<sub>4</sub>, RE<sub>3</sub>NbO<sub>7</sub>, RENb<sub>3</sub>O<sub>9</sub>, RENb<sub>5</sub>O<sub>14</sub>, and RENb<sub>7</sub>O<sub>19</sub>, where RE stands for rare earth lanthanide ions. Based on the RE ions and their ionic radius, different crystal structures exist.[60] According to [60], orthoniobates with the formula RENbO<sub>4</sub> have enhanced luminescent properties compared to other RE-niobates. They crystallize in a monoclinic structure and undergo a reversible ferroelastic phase transformation to a tetragonal system at high temperatures (above 700 °C).[58,82,83] The transformation temperature depends on the rare-earth ions.[17] Upon cooling, a monoclinic distortion occurs, resulting in the formation of ferroelastic domain structures which resemble twinning.[17,18] This leads to a characteristic ferroelasticity for RENbO<sub>4</sub>. Ferroelasticity is mainly observed in one of two forms of stress-induced crystal deformations, martensitic transformations and twinning deformation.[84] Both of these deformations are shear-induced and occur without diffusion of the atoms.[84] In the case of martensitic transformations, the crystal structure of the stress-induced domain and mother domain are of different phases, while on the contrary, for twinning deformations the stress-induced domain and mother domain are of the same phase. [84,85]

Different lanthanide niobates have been studied by different groups reporting the presence of twins in their structure, which are briefly summarized here. Prytz and Tafto reported that

LaNbO<sub>4</sub> shows a phase transformation upon cooling from a tetragonal to a monoclinic structure.[86] Their research indicates that the transformation occurs around 500°C and causes a monoclinic distortion associated with changes in the lattice parameters. These changes result in an increase in elastic lattice strain, which is accommodated by twinning. The authors referred to these twins as mechanical twins. Other literature reports that for RENbO<sub>4</sub>, at high temperature the tetragonal scheelite phase is stable but it reverts to the monoclinic fergusonite phase at approximately 550°C upon cooling.[87,88] A series of complex micro domain twins are created due to this phase transition. These microdomains are ferroelastic and many detailed studies about the domain structures at the nanoscopic regime have been done on them.[18,87–89] Rojas-Gonzalez et al studied EuNbO<sub>4</sub> nanoparticles. By taking HRTEM images, the presence of planar defects (twinning) in these particles was confirmed.[90] Furthermore, they suggested that due to its intense luminescence the system LiNbO<sub>3</sub>:Eu<sup>3+</sup>-EuNbO<sub>4</sub> is a good candidate for building light-emitting devices for medical and biological applications. Fulle et al. used a hydrothermal synthesis approach to grow RENbO<sub>4</sub> (RE= La<sup>3+</sup>, Nd<sup>3+</sup>, Eu<sup>3+</sup>, Gd<sup>3+</sup>, Lu<sup>3+</sup>).[87] Due to the high vapor pressure during the synthesis the monoclinic phase directly forms at low temperature without the necessity to form the tetragonal phase first. As a result, twinning is minimized or eliminated and high-quality single crystals are created.

In our recent work [49], we compared two types of complex niobates with different Praseodymium (Pr) concentration and reported that PrNbO<sub>4</sub> with monoclinic structure has enhanced luminescence compared to the cubic Pr<sup>3+</sup>:Ca<sub>2</sub>Nb<sub>2</sub>O<sub>7</sub>. In the present study, we focus on PrNbO<sub>4</sub> but with the emphasis on its crystal defects (such as twins) and the local differences in defect density in order to understand the excellent luminescent properties of these materials. We applied a multi-technique correlative methodology and acquired BSE images and CL spectra in a SEM at identical particles possessing locally different twin densities. (S)TEM lamellae have been prepared by FIB lift out technique from the same particles with a high density of twins and investigated using aberration corrected (S)TEM. We observed that changes in the intensity of the emission lines are related to different defect densities.

## 5.2. Experimental procedures

Synthesis of the polycrystalline samples was done using a solid-state route with protocols altered from the literature.[91] The optimum amount, described in [49], of K<sub>2</sub>CO<sub>3</sub>, CaCO<sub>3</sub>

and Nb<sub>2</sub>O<sub>5</sub> was mixed together with Pr<sub>6</sub>O<sub>11</sub>. Afterwards, to complete the reaction progress, various temperatures between 1100-1300°C were used to anneal the mixture. The product was then washed in deionized water, and dried at room temperature. This reaction was done to obtain particles with the nominal formula: Pr<sub>x</sub>K<sub>1-x</sub>Ca<sub>2-x</sub>Nb<sub>3</sub>O<sub>10</sub>. XRD reported in [49] showed the formation of two phases, namely Pr<sup>3+</sup>:Ca<sub>2</sub>Nb<sub>2</sub>O<sub>7</sub> and PrNbO<sub>4</sub>. PrNbO<sub>4</sub> particles were produced due to the excess of Pr. For these particles both Ca and K atoms of the parental phase were substituted by Pr. The particles used in the present work are micron sized (see SEM images in the following sections).

TEM samples of the PrNbO<sub>4</sub> particles were prepared in three different ways. First, electron transparent lamella was prepared using FIB milling from an individual powder particle deposited on a Si substrate. A conventional lift-out technique [92] was performed to prepare the lamella. In the final step, low-voltage (5 kV) cleaning process was used to remove the surface Ga-ion. All the process was done using a Scios2 instrument from Thermo Fischer. The lamella was used for BF and DF TEM imaging, as well as diffraction pattern observation and HR(S)TEM studies.

Second, for conventional TEM sample preparation, the powder was mixed with a Gatan G1 epoxy and hardener (two component glue). The mixture was then put into a brass tube with 2.3 mm inner diameter. After curing the tube at 130°C, the tube was cut into discs of approximately 200 µm thickness with a diamond saw. Using a disc grinder, the discs with a thickness of 80 µm were achieved. To obtain a thickness of 20 µm in the center of the sample, dimple grinding was applied. At the end, a precision argon ion polishing system (PIPS) from Gatan was used to prepare an electron transparent sample.[92] The ion milling was done without sample cooling. This sample was used for TEM observations.

In the third way, the powder was crunched with mortar in a ceramic bowl. Crunched particles were then mixed with ethanol and dropped on a continuous carbon film grid for further HRTEM investigations.

TEM BF, DF, HRTEM imaging and SAED studies were performed using a Thermo Fisher Scientific Titan TEM equipped with an X-FEG as electron source and an aberration corrector for the objective lens. The instrument was operated at 300 kV. EDX analysis was done using the attached Super X-detector from Bruker.

Further characterization was performed using a FEI Titan Themis 300, operated at 300 kV. This microscope is equipped with a  $C_s$  probe corrector. For STEM imaging a HAADF detector was used. The probe had a convergence angle of 23.8 mrad and a beam diameter of around 0.1 nm.

CL data were recorded in a FEG SEM Zeiss SEM 450, equipped with a motorized parabolic mirror, (acquisition software Odemis), without sample cooling system. An electron acceleration voltage of 15 kV, beam current of 5.5 nA and working distance of 15 mm was used. CL images were observed by panchromatic imaging and emission spectra were acquired in spectral mode. Powder particles were mixed in ethanol and dropped on silicon wafers. These wafers were then placed on SEM sample stubs using copper tape. For the correlative study, the FIB lamella was lifted out from the identical particle on which CL measurements were performed (see supplement, figure S1). BSE images were acquired with the same instrument using 15 kV, a beam current of 2 nA and working distance of 8 mm.

### **5.3. Results and Discussion**

#### **5.3.1. (S)TEM analysis of twins and twin densities**

TEM images of  $\text{PrNbO}_4$  particles exhibit lamellar shape twins as illustrated in Fig. 1. Two types of particles with different twin boundary densities were observed. Fig. 1.a shows the BF TEM image of an individual  $\text{PrNbO}_4$  particle with higher density of twins. The domains vary in size; the smallest observed twin width is less than 20 nm, while the largest observed twin width is more than 50 nm. Another individual  $\text{PrNbO}_4$  particle with a lower density of twins is displayed in Fig. 1.b. For this particle, the twin width is slightly bigger in size, i.e. 80 nm. As explained in [93], when a crystal transfers upon cooling to a structure with lower crystal symmetry, transformation twinning is almost inevitable when the new phase is nucleated at more than one center in the original phase. As stated earlier, these twins show ferroelastic behavior and are induced by stress.[84] Since the free-standing particles did not undergo any external deformation during their production, it must be assumed that the observed twins are due to the phase transformation during the synthesis. To measure the density of the twins, a perpendicular line to the twin boundaries with a length of 900 nm was drawn (indicated with blue on Fig. 5.1). Then the number of the twins for each particle was divided by the length of the blue line. The density of the twins for the particles in Fig. 5.1.a and b was measured using this line sectioning approach as  $0.05 \text{ nm}^{-1}$  and  $0.004$



$\text{nm}^{-1}$ , respectively.

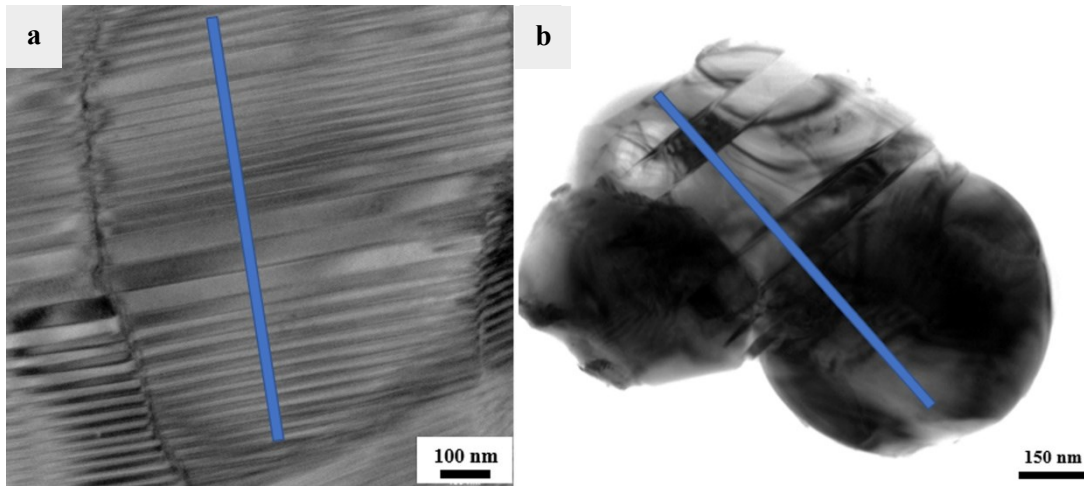


**Figure 5.1** BF images of PrNbO<sub>4</sub> particles with (a) higher density of twins ( $0.05 \text{ nm}^{-1}$ ) and (b) lower density of twins ( $0.004 \text{ nm}^{-1}$ ).

Since the twins with higher density were the dominant type of the observed twins on the particles, further analysis of these twins was carried out. FIB lamella lift out was done on an identical particle on which BSE and CL measurements were carried out (see Fig.5.2).

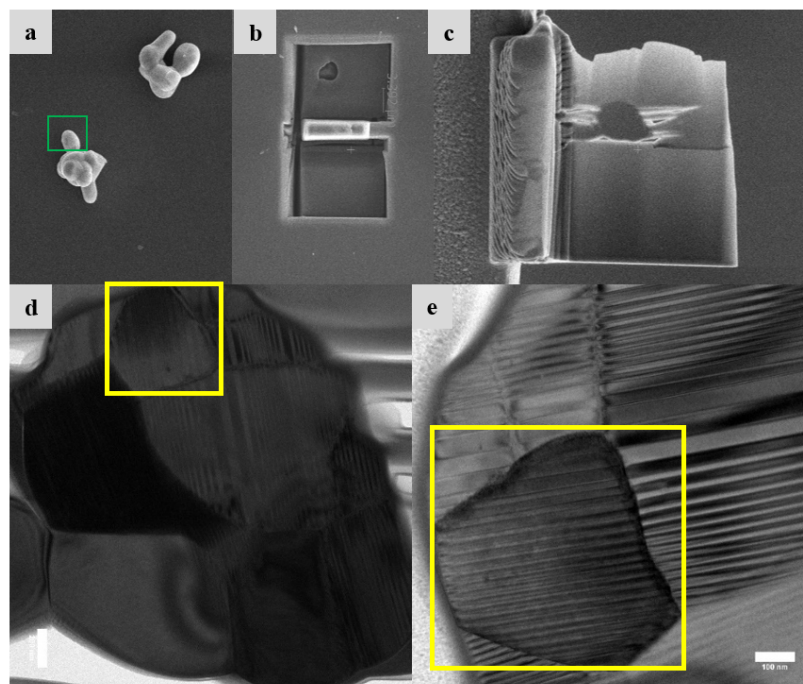


**Figure 5.2** (a) SEM micrograph of PrNbO<sub>4</sub> on a Si substrate; The green box marks the particle selected for lamella preparation. (b) and (c) show the SEM images of the FIB lamella preparation process. (d) TEM image of the Lamella; The yellow box indicates the selected grain on which the HR(S)TEM analysis was performed. (e) A more zoomed-in TEM image of the same grain.

The result of these measurements are given in section 3.2. BF and DF images of the lamella on the same grain are shown in Fig.5.3.a and b, respectively. A high density of nanotwins is visible in these images. The corresponding SAED pattern of this grain along the  $[\bar{1}0\bar{3}]$  zone axis is given in Fig.5.3.c. The  $(30\bar{1})$  and  $(020)$  planes are indicated on the diffraction pattern. As shown on the SAED pattern, there are no other phases observed and the pattern agrees well with the one for  $\text{PrNbO}_4$  (ICSD109176) which has a monoclinic structure.

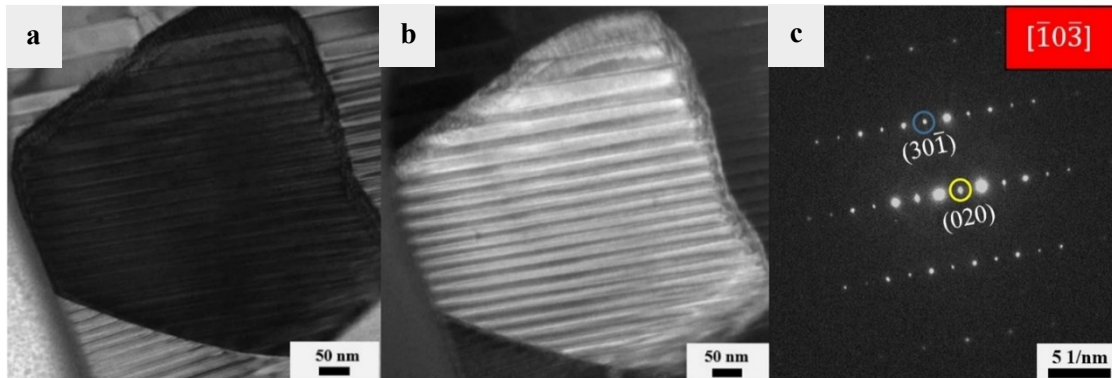


**Figure 5.3** (a) BF image of  $\text{PrNbO}_4$  lamella with corresponding (b) DF image and (c) SAED pattern in the zone axis  $[\bar{1}0\bar{3}]$ .

To observe the atomic structure, aberration corrected HRTEM images of the same grain were taken (Fig.5.4.a). A more zoomed in image is presented in Fig.5.4.b.

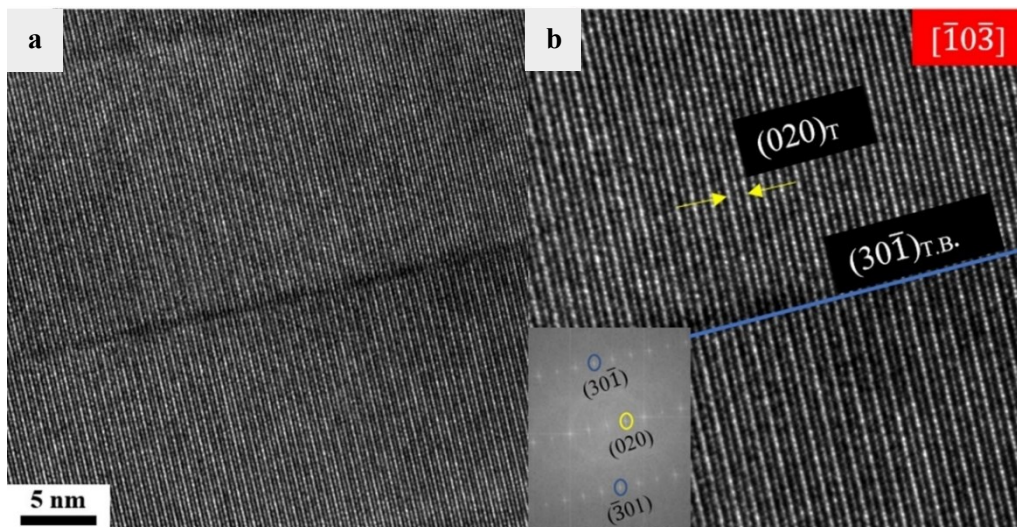


**Figure 5.4** (a) HRTEM image of  $\text{PrNbO}_4$  lamella (b) zoomed-in image on the twins. (T.B. stands for twin boundary). The inset shows the FFT pattern of the same area. Twin boundary is marked with blue circles on the FFT pattern and blue line on the HRTEM image. Twin planes are indicated with yellow arrows on the HRTEM and yellow circle on the FFT pattern.

The inset shows the fast Fourier transform (FFT) pattern which was used to index the twin

boundary plane as  $(30\bar{1})$ . This agrees with S. Tsunekawa et. al. [82] who illustrated that  $(602)$  or  $(20\bar{6})$  are possible twin boundary planes for  $\text{NdNbO}_4$ . The crystal was oriented in the  $[\bar{1}0\bar{3}]$  zone axis.

The contrast in HRTEM micrographs cannot be directly interpreted as atomic columns due to the dependence on focus and sample thickness. To confirm where the atomic columns are located, HRSTEM measurements were thus performed on the same lamella. HAADF and BF imaging of the same grain as shown in Fig.5.3 are presented in Fig.5.5. The grain was tilted to the same zone axis as in Fig.5.4. The twin boundary plane  $(30\bar{1})$  is marked with a blue line on both HAADF and BF images. HRSTEM and HRTEM images of the lamella are in agreement with each other. Based on that, it is proved that the twins have a coherent structure.

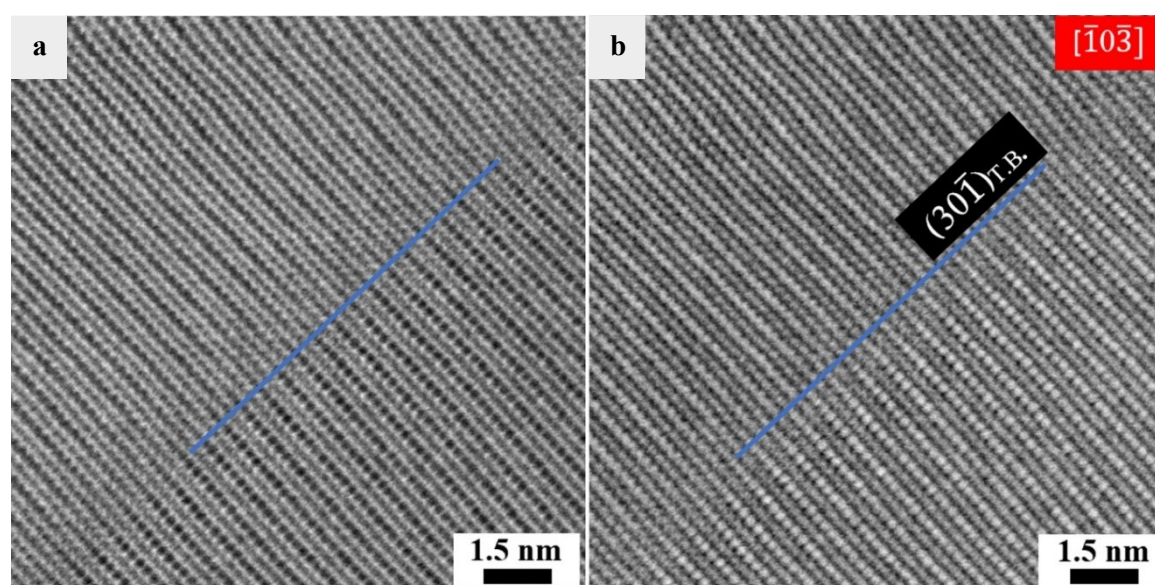


**Figure 5.5** (a) HRSTEM-HAADF image of  $\text{PrNbO}_4$  lamella (b) HRSTEM-BF image of the lamella in the same location. The blue line on both images indicates the twin boundary plane. (both HAADF and BF images are acquired at the identical place)

### 5.3.2. CL and BSE analysis of the twins

To study the influence of the twin density on the optical properties of the particles, CL measurements were done directly on powder particles glued to a support without further sample preparation. BSE imaging was performed to find particles with twins. The results of two particles as the representative of the major group (particles with high density of twins) and minor group (particles with low density of twins) are reported here. Fig.5.6.a shows BSE image of a  $\text{PrNbO}_4$  particle (particle I). A high density of twins is seen on this

particle. Using FIB technique, we were able to lift out a lamella from the twinned region of this particle in the upper region. TEM and STEM studies explained in the previous sections were performed on the same lamella. The corresponding panchromatic CL image of the particle is shown in Fig.5.6.b.

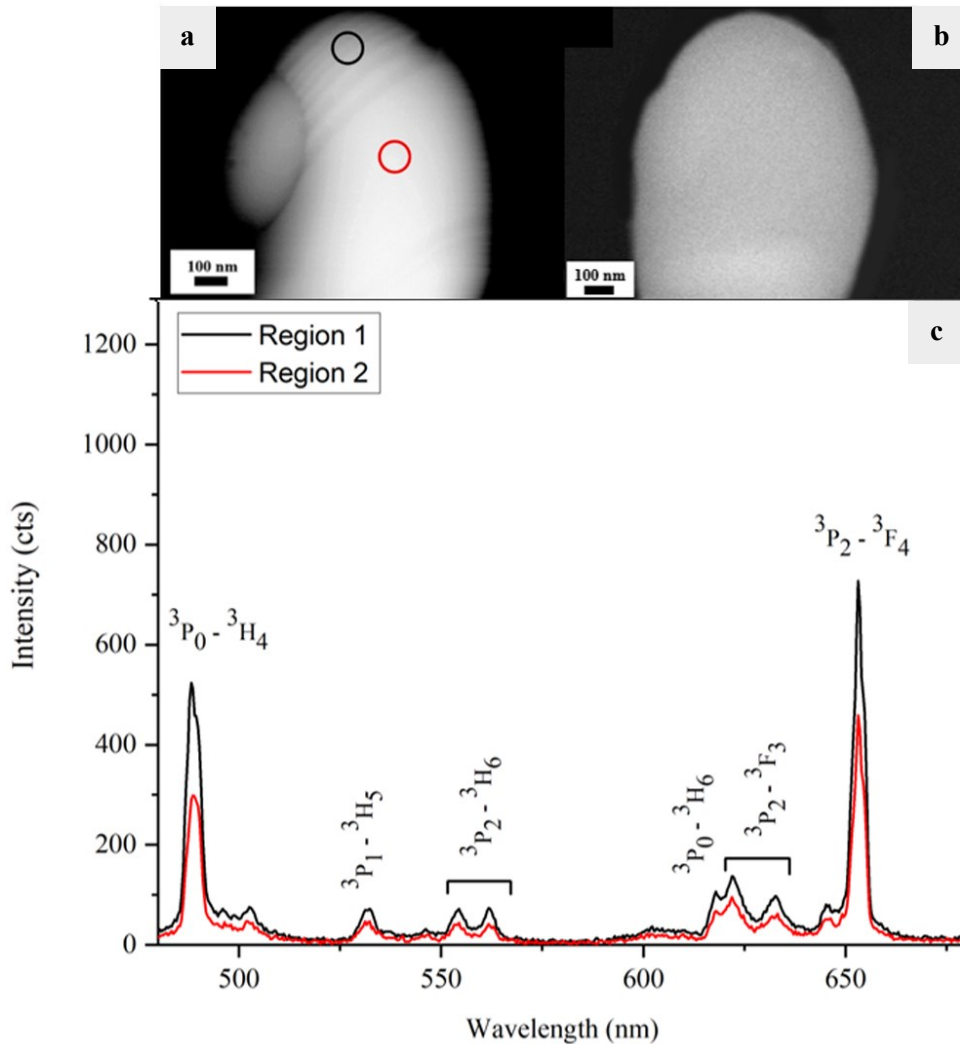


**Figure 5.6** (a) BSE image of the higher density twinned particle (twin density is  $0.0425 \text{ nm}^{-1}$ ) and (b) corresponding panchromatic CL image. (c) CL spectra of the particle where the black curve corresponds to the spectra acquired at the twinned area and the red curve to the twin free area).

Fig.5.7.a illustrates the BSE image taken from another particle (particle II) with a lower twin density. Fig.5.7.b displays the panchromatic CL image of particle II. The density of the twins for particle (I) and (II) was measured as explained in section 3.1; The findings are  $0.0425 \text{ nm}^{-1}$  and  $0.0075 \text{ nm}^{-1}$ , respectively.

As we do not observe any intensity difference based on panchromatic CL images, further analysis based on the CL spectra was carried out. As seen in Fig.5.6.a and Fig.5.7.a, not all the regions on the particles have twins. CL spectra for each particle were acquired on the twinned and twin-free areas. The background noise was removed for all the spectra. The CL spectra of the two selected regions for particle (I) are shown in Fig.5.6.c. Region 1 is the area with nanotwins of a density  $0.0425 \text{ nm}^{-1}$ . Region 2 belongs to an area without twinning. Fig.5.7.c displays the CL spectra of two regions for particle (II). In both graphs, the twinned areas are coloured in black and twin free areas in red.

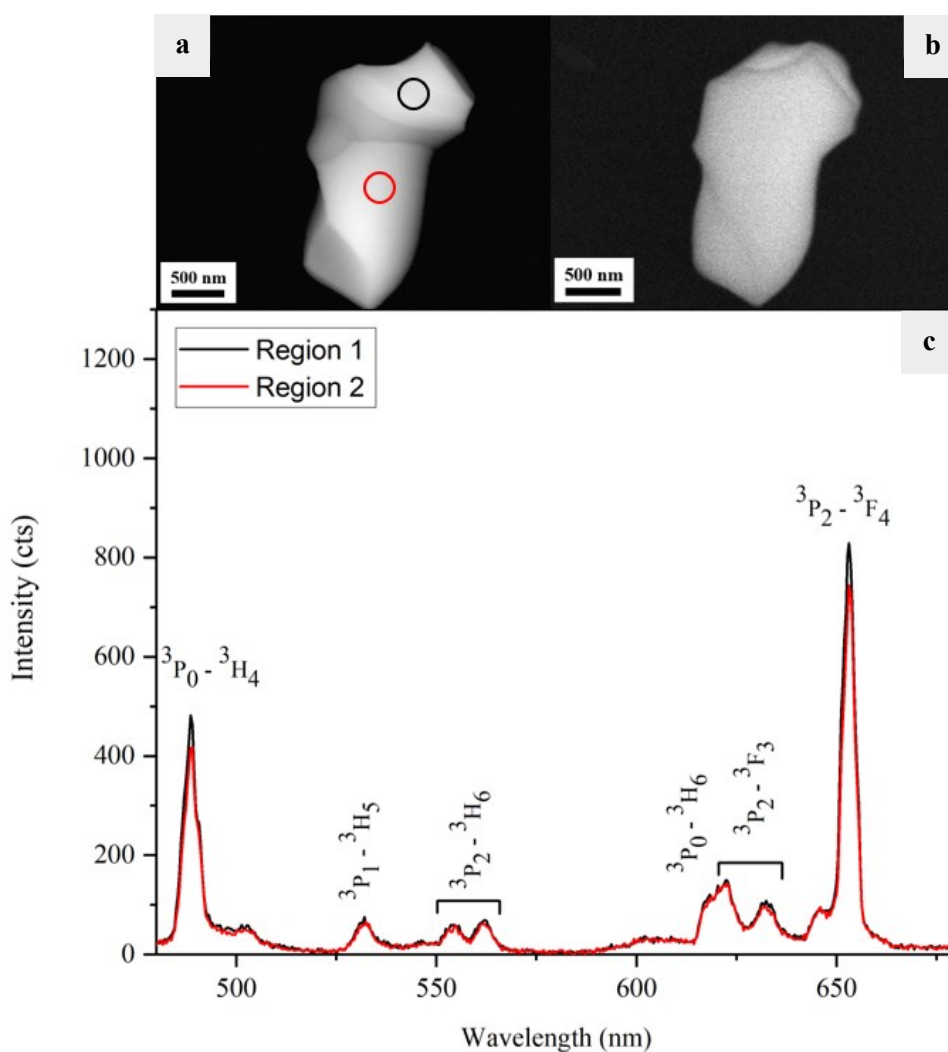


**Figure 5.7** (a) BSE image of a representative particle with a low density of twins ( $0.0075 \text{ nm}^{-1}$ ) and (b) panchromatic CL image taken on the same particle. (c) CL spectra of the particle with the measurement areas marked in red (twin free area) and black (low density of twins) in (a).

The position of all emission lines are the same in both spectra and exhibit the following transitions  ${}^3P_0$  to  ${}^3H_4$ ,  ${}^3P_1$  to  ${}^3H_5$ ,  ${}^3P_2$  to  ${}^3H_6$ ,  ${}^3P_0$  to  ${}^3H_6$ ,  ${}^3P_2$  to  ${}^3F_3$ , and  ${}^3P_2$  to  ${}^3F_4$ . All these

transitions are the main transitions of the lanthanides which are labelled according to the Dieke diagram ( $\text{Pr}^{3+}:\text{LaCl}_3$ ).[25] However, the intensity is different for the areas with the twins compared to the twin free area. The intensities of the emission lines are compared to each other and summarized in table 5.1.

For particle (I) the intensity of the twinned area is considerably higher compared to the twin free areas. Whereas for particle (II), which has lower density of twins, the intensity of the twinned area except for the dominant transitions is the same compared to the twin free area. To determine the exact difference, we have calculated the relative differences between the twinned versus twin free peaks with respect to the lower peaks. Results are shown in table 5.2.

**Table 5.1:** Intensity comparison between four spectra related to the twinned and twin free areas of the particles.

Regions	$^3\text{P}_0$ to $^3\text{H}_4$	$^3\text{P}_1$ to $^3\text{H}_5$	$^3\text{P}_2$ to $^3\text{H}_6$	$^3\text{P}_0$ to $^3\text{H}_6$	$^3\text{P}_2$ to $^3\text{F}_3$	$^3\text{P}_2$ to $^3\text{F}_4$
(I) Twinned	524	72	73	107	117	728
(I) Twin free	297	47	44	64	76	459
(II) Twinned	482	66	68	109	129	829
(II) Twin free	416	66	68	109	129	744

**Table 5.2:** Percentage difference of the twinned versus twin free peaks.

Particle	$^3\text{P}_0$ to $^3\text{H}_4$	$^3\text{P}_1$ to $^3\text{H}_5$	$^3\text{P}_2$ to $^3\text{H}_6$	$^3\text{P}_0$ to $^3\text{H}_6$	$^3\text{P}_2$ to $^3\text{F}_3$	$^3\text{P}_2$ to $^3\text{F}_4$
(I) % difference of the twins vs. twin free peaks	+76	+53	+66	+67	+54	+58
(II) % difference of the twins vs. twin free peaks	+16	0	0	0	0	+11

We compared the peak ratios and position of the twin free areas for both particles. Despite having different thicknesses for each particle leading to changes in the absolute intensity

values, the relative intensity ratio for all the peaks except  ${}^3P_2$  to  ${}^3F_4$  are similar and the peak position change only within 1 nm. This data is given in table 5.3.

**Table 5.3:** Peak ratios of the twin free areas for both particles. CL spectra are normalized to their highest peak ( ${}^3P_2$  to  ${}^3F_4$ ) to 100, and the relative intensities for the other transitions are listed.

Regions	${}^3P_0$ to ${}^3H_4$	${}^3P_1$ to ${}^3H_5$	${}^3P_2$ to ${}^3H_6$	${}^3P_0$ to ${}^3H_6$	${}^3P_2$ to ${}^3F_3$	${}^3P_2$ to ${}^3F_4$
(I) Twin free	65	9	8	15	12	100
(II) Twin free	56	8	8	16	12	100

For particle (I), due to the high density of twins all the peaks show 53% to 76% increase versus the peaks from the non-twinned areas. However, for particle (II), only the peaks associated with  ${}^3P_0$  to  ${}^3H_4$  and  ${}^3P_2$  to  ${}^3F_4$  are increased by 16% and 11%, respectively. These two transitions are considered as the dominant transitions of the trivalent Pr regardless of the type of host.[70–72,94–96] For the rest of the transitions, no difference was observed. The reason for higher intensities observed for particle (I) in total could be related to the higher density of the twins. As explained in [97], due to the shielding effect of the outer 5s and 5p electrons, the optical properties of inner shell f–f transitions in lanthanide compounds are usually not sensitive to the surrounding environment. However, there exist exceptional transitions which are called hypersensitive transitions.[98] The intensities of the hypersensitive transitions change greatly by a small change of surrounding environment, although their excitation energies remain insensitive.[98] These transitions obey the selection rules,  $|\Delta S| = 0$ ,  $|\Delta L| \leq 2$  and  $|\Delta J| \leq 2$  in the case of  $Pr^{3+}$  ion with  $\Delta S$  being the difference in the spin quantum number,  $\Delta L$  of the orbital angular momentum and  $\Delta J$  of the total angular momentum.[98] Based on this we know that transition associated with  ${}^3P_2$  to  ${}^3F_4$  is hypersensitive and this can explain why this transition has higher intensity compared to the rest.

Monte Carlo electron trajectory simulations in  $PrNbO_4$  were performed using the software Casino v2.51 at an acceleration voltage of 10 kV (see Fig.5.8). The electrons penetrate into the sample up to 500 nm and the width of the penetration is around 800 nm. Thus, the interaction volume is smaller than the particle size. Also, the CL signal comes from a volume with several hundred nanometres in dimension. We can still distinguish clearly the regions with high twin density and low twin density. It is also important to mention that

our TEM investigations reveal that the twins extend from the top surface to the bottom surface of the particle and thus a large twin area is contributing to the observed CL signal.

Presence of defects in lanthanide doped materials allows parity forbidden f-f transitions to occur.[13,74,75] According to [99], local distortions (surface effects and defects such as vacancies, dislocations and interstitial defects) will lower the symmetry and therefore induce an increase in the relative intensity of the electric dipole transitions. Similar effects are also expected for twins. Since higher emission lines are observed for the twinned areas, we believe that these crystal defects are perturbing f-f transitions resulting in increased intensity. Based on these results and our recent findings published in [49], the high amount of Pr in addition to the presence of defects in PrNbO<sub>4</sub> make these particles excellent luminescent materials. Moreover, we showed with our multi-technique approach that higher density of the twins leads to the strongest luminescence brightness and therefore they are better candidates to be used in optical applications.

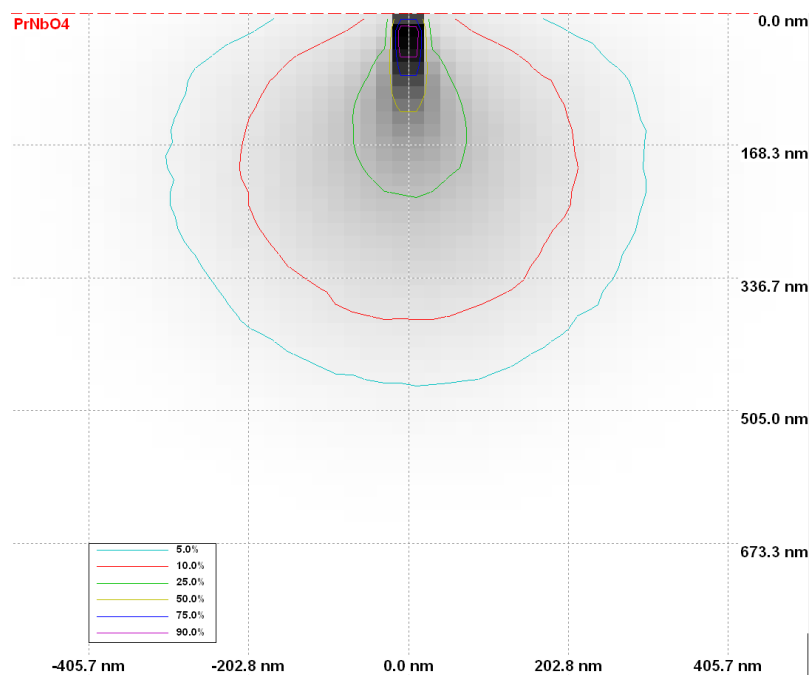


**Figure 5.8** Monte Carlo simulations of electron trajectories in PrNbO<sub>4</sub> at beam accelerating voltage equal to 10 kV. The colored lines indicate the percentage of the electrons which have not come to rest.

#### 5.4. Other twin types in PrNbO<sub>4</sub>



The majority of the observed twins were having a  $(30\bar{1})$  twin boundary plane as described above. However, other twin types were observed in TEM as explained in the following. Since these twins were the minority, CL measurements was not performed for them.

#### 5.4.1. Twins with (200) twin boundary plane

As mentioned in [82], there exist different types of twin boundary planes for lanthanide niobates. HRTEM on a conventional powder sample showed a different twin boundary plane with inclined twin planes on a  $\text{PrNbO}_4$  particle. Results are presented in Fig.5.9. The HRTEM micrograph of this particle allowed us to determine the twin boundary plane to be (200). The (161) planes are mirrored as visible in the FFT. Twin boundary plane is identified by blue circles on the FFT pattern, as well as a blue line on the HRTEM image.

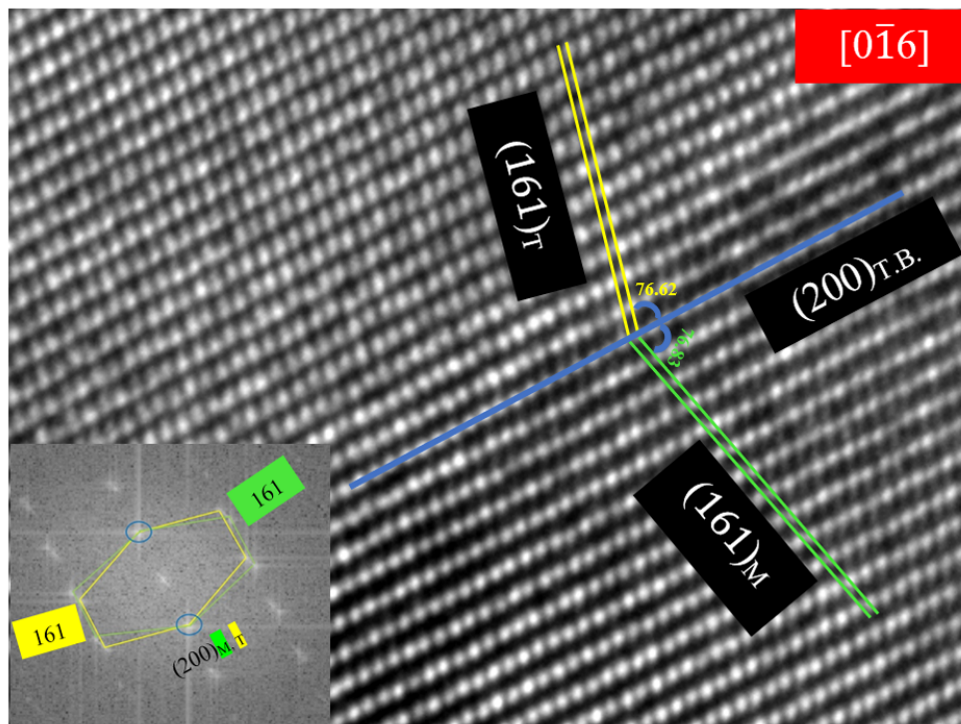


**Figure 5.9** HRTEM image of  $\text{PrNbO}_4$  particle. (T.B. indicates the twin boundary. M and T stand for matrix and twin, respectively). The inset shows the FFT pattern of the same area. Pattern of the matrix is indicated in green and twin in yellow)

We used the FFT pattern to determine the twin boundary plane and the according zone axis. The crystal was oriented in the  $[0\bar{1}6]$  zone axis and we indexed (161) and (200) as the twin planes and twin boundary plane, respectively. Moreover, the angle between the twin

boundary plane and conjugate twin plane was measured. The result is almost the same ( $76.6^\circ$  and  $76.8^\circ$ ) on both sides and indicates mirror symmetry. Since the atoms along the boundary belong to both lattices, it can be claimed that these twins are coherent. The appearance of such twin is in accordance to [82].

In order to prove where the atomic columns are located, a multislice simulation was carried out for monoclinic structure of  $\text{PrNbO}_4$  along the  $[0\bar{1}6]$  zone axis and the corresponding thickness–defocus map is shown in Fig.5.10. The experimental images were captured in the microscope with  $C_s = -0.18$  mm at an operating voltage of 300 kV. As seen from the simulated image, the contrast varies significantly with thickness and defocus. Around the defocus value equal to 35 nm with thickness equal to 7.15 nm, the Nb and Pr atoms are giving a bright contrast. This area is marked in green on Fig.5.10. With decrease in the defocus values, i.e., 10 nm, the Pr and Nb atoms become dark and the O atoms become bright. For the present experimental conditions, all the Pr and Nb atoms appear bright. This is in support of the bright atom contrast seen in the acquired HRTEM image shown in Fig.5.9.

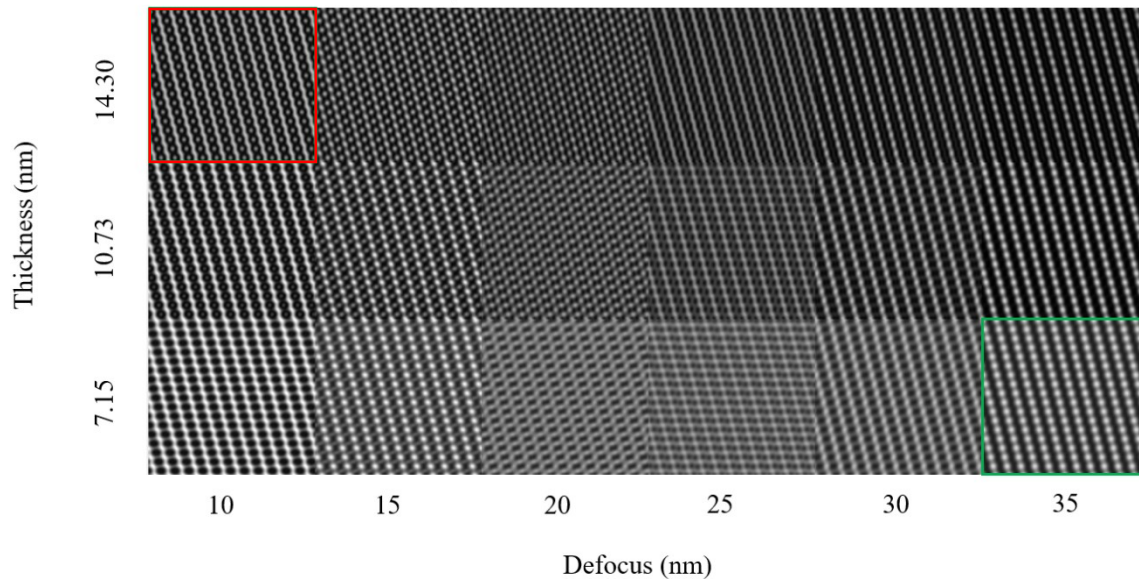


**Figure 5.10** Simulated defocus-thickness map of monoclinic  $\text{PrNbO}_4$  along  $[0\bar{1}6]$  zone axis by multislice method. Accelerating voltage = 300 kV,  $C_s = -0.18$  mm.

As shown in Fig.5.10, close to a defocus equal to 10 nm and a thickness equal to 14.30 (marked in red) we should be able to see the O atoms clearly. For this reason, we changed our initial defocus and went to a thicker area to be able to resolve O atoms. The results are

shown in Fig.5.11. Fig.5.11.a represents the simulated image with defocus equal to 10 nm and thickness equal to 14.30.

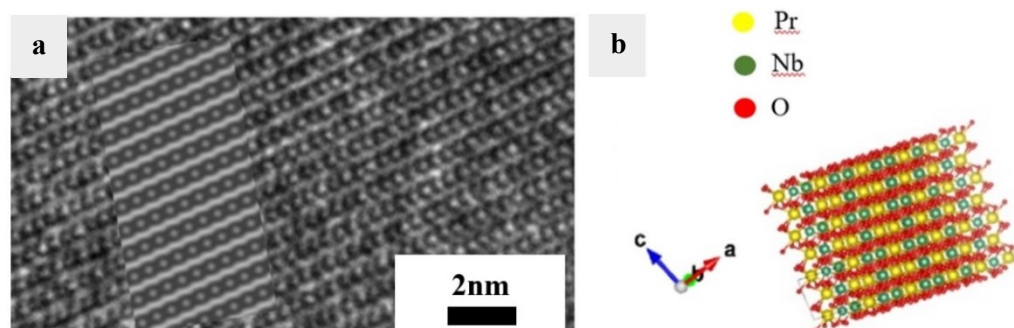


**Figure 5.11** (a) Experimental HRTEM image of PrNbO<sub>4</sub> superimposed with simulated defocus-thickness map of monoclinic PrNbO<sub>4</sub> along  $[0\bar{1}6]$  zone axis. The defocus value is 10nm, and thickness value is 14.30nm (b) Crystal structure of PrNbO<sub>4</sub> viewed along same zone axis (yellow spheres, Praseodymium; green, Niobium; red, Oxygen)

The HRTEM image of PrNbO<sub>4</sub> is superimposed in Fig.5.11.a. This image shows the Pr, Nb atoms with spherical shape and the O atoms as extended chain which matches with its simulated image. The structure of PrNbO<sub>4</sub> in its monoclinic structure viewed along  $[0\bar{1}6]$  is shown in Fig.5.11.b using the program VESTA ver. 3.3.2 and basic atom locations: Pr(0.25, 0.12, 0), Nb(0.25, 0.65, 0), and O(0.01, 0.72, 0.2). HRTEM images were analyzed and interpreted based on their simulation using the Java Electron Microscopy Simulation (JEMS) software [100] for a monoclinic crystal structure of PrNbO<sub>4</sub> (space group: C2/c) with the lattice parameters  $a = 5.499 \text{ \AA}$ ,  $b = 5.157 \text{ \AA}$ ,  $c = 11.342 \text{ \AA}$ , and  $\alpha = 90^\circ$ ,  $\beta = 94.57^\circ$ ,  $\gamma = 90^\circ$  (ICSD 109176).

#### 5.4.2. Deformation twins

According to [101], deformation twins are formed due to the excess of strain energy especially at the rims of the crystals. These twins have a lens like shape caused by the minimization of the strain energy. Shockley partial dislocations are activated by the shear stress. As a result, deformation twins are formed by the motion of partial dislocations in a coordinated way. More information on this type of twinning can be read in [101]. Fig.5.12.a shows a TEM image of several crunched PrNbO<sub>4</sub> particles. HRTEM image of a crunched PrNbO<sub>4</sub> particle with a deformation twin is given in Fig.5.12.b. The lens like shape on the

particle indicates the excess of energy while crunching the particles with a mortar. Since this type of twinning was the minority, CL investigations on the crunched particles were not carried out.

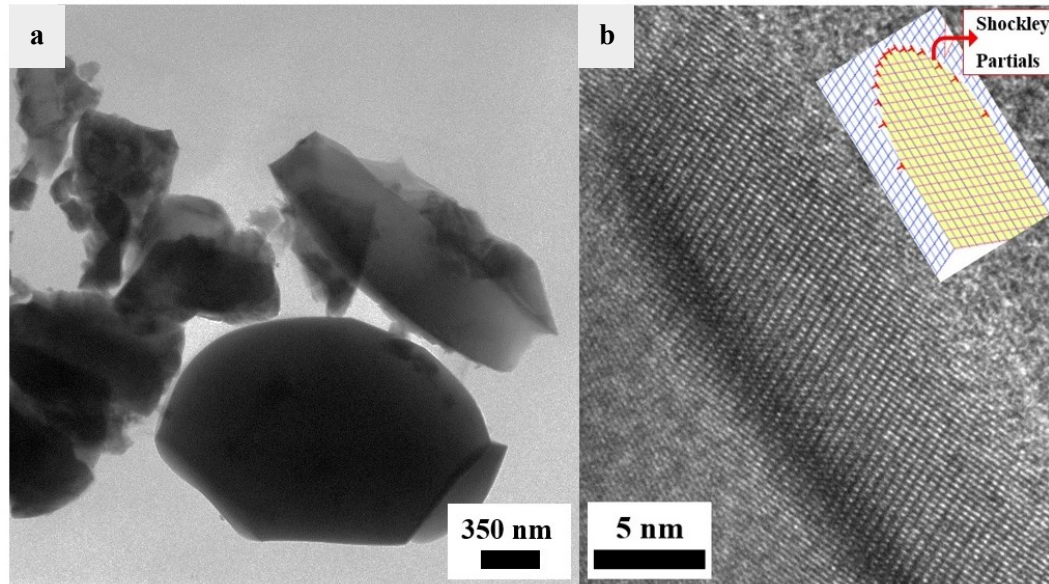


**Figure 5.12** (a) TEM image of crunched PrNbO<sub>4</sub> particles. (b) HRTEM image of a deformation twin on a crunched PrNbO<sub>4</sub> particle. The inset is reproduced from [101] © H. Föll (Iron, Steel and Swords script) and shows the arrangement of Shockley partials due to deformation twinning.

## 5.5. Conclusion

BSE, CL and TEM studies were performed on PrNbO<sub>4</sub> powder particles at identical location. Crystal defects of PrNbO<sub>4</sub> are visualized and explained in detail. Twinning as a result of phase transformation during the synthesis of the particles were observed. Further analysis showed that the twins are coherent. Two types of particles with high density and less density of the twins were found. The effect of the defect density on the optical properties of PrNbO<sub>4</sub> was investigated. Emission lines acquired for both of the particles were compared. For all these regions, there is no shift in the peak positions, however, there is a noticeable change in the intensity of the emission lines. Twinned areas with higher density showed higher intensity in comparison to twin free areas and the regions with less density of the twins. For the major emission lines associated with the  $^3P_0$  to  $^3H_4$  and  $^3P_2$  to  $^3F_4$ , regardless of the density, the intensity was significantly higher. Other twin types, namely deformation twins and phase transformation twins with a different twin boundary

plane were observed for PrNbO<sub>4</sub> particles. Since these types of twins were the minority, further detailed investigations such as CL analysis were not carried out for them.



## 6. Structural and Cathodoluminescence Investigations of Pr<sup>3+</sup>-Doped Ca<sub>2</sub>Nb<sub>3</sub>O<sub>10</sub> Nanosheets

This chapter is based on the manuscript by Changizi, R.; Zaefferer, S.; Ziegler, C.; Romaka, V.; Lotsch, B.; and Scheu, C.; which was submitted and is currently under review. The focus of the chapter is on 2D nanosheets exfoliated from a Pr<sup>3+</sup> doped KCa<sub>2</sub>Nb<sub>3</sub>O<sub>10</sub> particles with different Pr concentrations. The chemical composition of the nanosheets are analyzed by STEM EDX measurements and given in details. Moreover, the luminescent behaviour of the nanosheets are compared to the one from the bulk. In the end of the chapter, structural characterization of the nanosheets is demonstrated using (S)TEM imaging and multislice simulation method.

### 6.1. Literature review

Atomically thin nanosheets, termed “two-dimensional” materials have been lately the topic of interest.[19,102] This is due to the novel properties related to the quantum confinement effects and the large number of active surface atoms relative to the bulk. Butler et al.[103] defines two-dimensional (2D) material as a material in which the atomic arrangement and bond strength along two-dimensions are similar and much stronger than along the third dimension.[103] The fact that 2D materials have different properties compared to the bulk [19] has attracted attention in the scientific community. Unique chemical and physical properties, improved mechanical flexibility, enhanced electrical and optoelectronic properties, among others, are mentioned in literature.[19,103–105] Graphene is an archetypical 2D material which was prepared in 2004 by Geim’s group through the Scotch tape exfoliation of graphite.[106] Geim and Novoselov were awarded with the Nobel prize for their discovery.

There is a growing interest in 2D rare-earth nanomaterials because of the novel luminescent and magnetic properties conferred by 4f-4f transitions.[19] Due to the inner 4f-4f energy level transitions, lanthanide ions can emit photons with almost the same energy while being surrounded by different chemical environments.[104] However, to make full use of this property, it is crucial to find a way to dope the lanthanide ions into the host and cast them into 2D sheets as efficiently as possible. Even though luminescence of lanthanide ions doped 2D nanosheets is rarely studied [107], the existing literature related to the topic is briefly summarized here.

Liu et al.[104] confirmed that doping lanthanide ions into 2D nanosheets can adjust the emission region. They have shown that doping  $\text{Nd}^{3+}$  ions broadens the emission region of  $\text{In}_2\text{Se}_3$  nanosheets from the visible to the near infrared NIR range. According to this group [104], 2D  $\text{In}_2\text{Se}_3:\text{Nd}^{3+}$  nanosheets with strong NIR luminescence can be used in NIR photonic nanodevices and biomedicine applications.

The fabrication of lanthanide-containing  $\text{NaYF}_4$  2D nanosheets was performed by Clarke et al.[105]. They mentioned that exfoliated 2D materials commonly exhibit a bandgap widening after exfoliation, while the  $\text{NaYF}_4:\text{Yb,Er}$  nanosheets display a noticeable narrowing of the bandgap. This was confirmed by density functional theory (DFT) calculations and valence band photoemission measurements.[105] They reported that by decreasing the nanosheet thickness, the PL emission becomes weaker, which is due to the presence of fewer excited ions.[105]

In another study, Bai et al.[108] observed that the introduction of lanthanide ions can expand the intrinsic narrow-band emission of layered transition metal dichalcogenides (TMDs). TMDs are 2D layered semiconductors. To prove their statement, they doped  $\text{Er}^{3+}$  into the lattice of bi-layered  $\text{MoS}_2$  and found that the NIR emission is obtained.

Huang et al.[107], developed a simple and environmentally friendly strategy to enhance the luminescence properties of  $\text{MgWO}_4:\text{Ln}^{3+}$  ( $\text{Ln} = \text{Eu, Tb}$ ) nanosheets through incorporation of carbon dots (CDs) to form  $\text{CDs}@ \text{MgWO}_4:\text{Ln}^{3+}$  nanostructures. They reported that the incorporation of CDs with  $\text{MgWO}_4:\text{Ln}^{3+}$  nanosheets have slight effect on the morphology and phase structure but increases the PL emission intensity of  $\text{CDs}@ \text{MgWO}_4:\text{Eu}^{3+}$  and  $\text{CDs}@ \text{MgWO}_4:\text{Tb}^{3+}$  nanosheets. They claimed that the luminescence enhancement mechanism was due to the capture of electrons by CDs and energy transfer between CDs and luminescent  $\text{Ln}^{3+}$ . These CDs have a size of 3-5 nm.[107]

In our recent studies [49,79], we reported the correlation between crystal structure, Pr concentration and defects density on the luminescent properties of bulk material with a particle size of several  $\mu\text{m}$  and different structures including  $\text{PrNbO}_4$  (cubic) and  $\text{Pr}^{3+}:\text{Ca}_2\text{Nb}_2\text{O}_7$  (monoclinic). In the present work, we study  $\text{Pr}^{3+}$  doped  $\text{Ca}_2\text{Nb}_3\text{O}_{10}$  nanosheets and compare their luminescence with the aforementioned bulk particles.

## 6.2. Experimental procedures



To obtain 2D nanosheets, Pr<sup>3+</sup> doped KCa<sub>2</sub>Nb<sub>3</sub>O<sub>10</sub> powder particles with a nominal formula K<sub>1-x</sub>Ca<sub>2-x</sub>Pr<sub>x</sub>Nb<sub>3</sub>O<sub>10</sub>, [x= 0.05 and 0.50] were exfoliated in a 2-step process. First, K was exchanged against protons and subsequently exchanged against a bulky organic cation such as tetra-*n*-butylammonium (TBA<sup>+</sup>). As a result, individual [Ca<sub>2</sub>Nb<sub>3</sub>O<sub>10</sub>]<sup>-</sup> nanosheets were produced. More details can be found in [32].

TEM samples of the nanosheets were produced by mixing the sheets into ethanol and deionized water. To increase the dispersion of the sheets, the solution was placed in an ultrasonicator for 20 minutes. The final suspension was dropped onto a TEM grid (Cu or Au) covered by an amorphous holey-carbon film and dried.

HRTEM imaging and other TEM modes such as BF imaging were performed in a Thermo Fisher Scientific Titan TEM which has an X-FEG and an aberration corrector for the objective lens. An acceleration voltage of 300 kV was used to operate the microscope. A super X-detector from Bruker was used to perform EDX analysis. Acquisition time for each EDX map was 25 minutes to obtain good statistic with a high signal to noise ratio.

A FEI Titan Themis 300 STEM equipped with a Cs probe corrector was applied to do further investigations. The microscope was operated at 300 kV. STEM images were taken with a HAADF detector. A convergence angle of 23.8 mrad was used for the probe, with a spot size of around 1 Å.

HRTEM images were analyzed and interpreted based on simulations using JEMS software for a pseudo 2D crystal structure of [Ca<sub>2</sub>Nb<sub>3</sub>O<sub>10</sub>]<sup>-</sup> nanosheets. For this, a CIF file was created as follows.

To construct a set of 2D nanosheets and represent it as a 3D periodic structure, several necessary structural transformations were performed, including origin shift, supercell construction, K atom removal, and vacuum slab creation, using VESTA program. At the first stage, the origin of the initial crystal structure was changed by 0.5 along the *c* basis vector to position all atoms of the 2D sheet in the central part of the unit cell. After that, a 1×1×2 supercell was created by changing the value of the *P*<sub>33</sub> element of the transformation matrix (*P*) from 1 to 2. To be able to freely remove individual atoms for the creation of the vacuum slab the symmetry of the structure was removed (reduced to space group *P*1) while keeping the atomic coordinates of all generated atoms in the supercell unchanged. The thickness of the slab is 1.4-1.5 nm. At the final stage, all K atoms were removed from the structure, as well as all atoms with *z*-coordinate ≥ 0.5. After these structural

transformations, half of the unit cell along the *c*-direction contains the created 2D nanosheet which is separated from the same nanosheet in the neighboring unit cell by the vacuum slab, so that the interaction between the 2D sheets is minimized. The resulting structure was exported to CIF for image simulations.

A FEG SEM (Zeiss SEM450) equipped with DELMIC SPARC system was used to study CL properties of the nanosheets. The device has a motorized parabolic mirror which is used to reflect the generated light towards the lenses. Investigations were performed at an electron acceleration voltage of 10 kV, a beam current of 5.5 nA and a working distance of 14 mm. For the acquisition no sample cooling system was used. For CL investigation, the nanosheets were mixed with deionized water and dispersed on a Si substrate.

## 6.3. Results and discussions

### 6.3.1. EDX analysis of the nanosheets

EDX measurements were performed on 2D nanosheets exfoliated from  $K_{1-x}Ca_{2-x}Pr_xNb_3O_{10}$ , [ $x= 0.05$  and  $0.50$ ]. The first group was supposed to have a low concentration of Pr and in the second group, a high Pr concentration was expected. EDX spectra were acquired on up to 30 nanosheets. For the 2D nanosheets with lower concentration of Pr used during the synthesis, the HAADF image and corresponding EDX spectra are shown in Fig.6.1. As seen in this figure, two individual nanosheets with different brightness in the HAADF image were investigated. The different brightness indicates a different thickness and/or different composition. The brighter appearing sheet in Fig.6.1.a shows a higher peak intensity for the Nb- $K_\alpha$ , Nb- $K_\beta$ , Nb-L and Ca- $K_\alpha$  and Pr-L lines than the dark appearing sheet (Fig.6.1.b) which shows the same element specific lines. The quantitative evaluation of the EDX data reveals that the ratio between the elements for both sheets stays the same. This indicates that the difference in brightness in the HAADF image is related to a different thickness of the nanosheets but not a difference in composition. However, due to the absorption phenomena for light elements, the O ratio with respect to other elements is different for different sheets. As a result, the ratio of O and Nb changes between the two sheets. Based on the EDX data, the exfoliation process was successful, indicated by the absence of K. Additional peaks belong to C, and other contaminations such as Au and Cu which belong to the TEM grid and other artefacts.

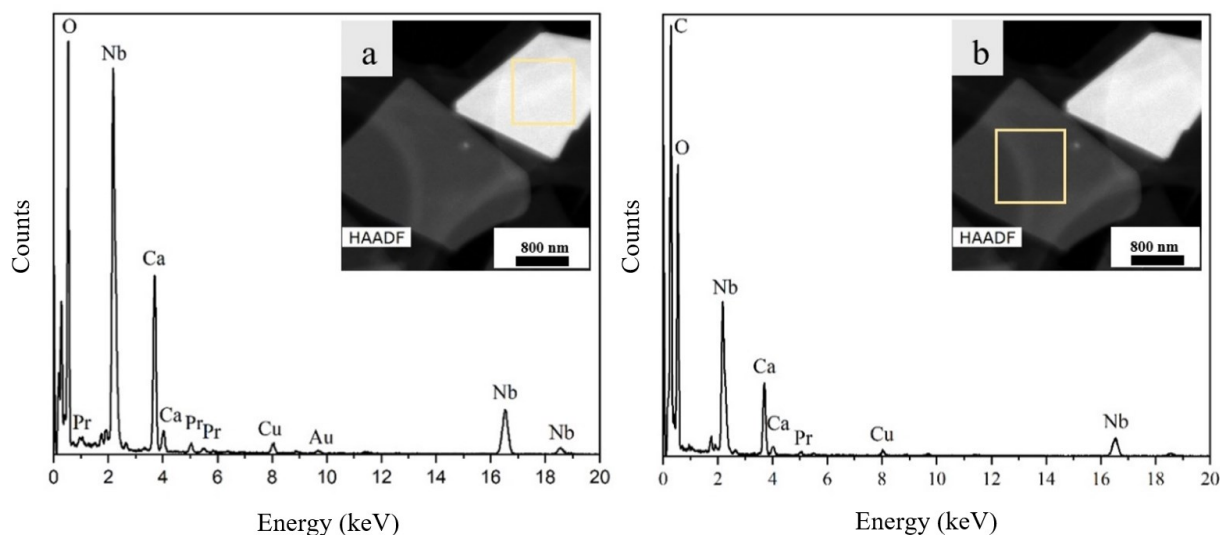


**Figure 6.1** HAADF micrograph and corresponding EDX spectra of individual  $\text{Pr}^{3+}$  doped  $\text{Ca}_2\text{Nb}_3\text{O}_{10}$  nanosheets synthesized with a low Pr content: (a) thicker nanosheet and (b) thin nanosheet. The spectra were extracted from the regions marked with a yellow square.

Similar observations were made for the nanosheets which were synthesized with a higher concentration of Pr. Fig.6.2 presents the HAADF image and the EDX spectrum of a single nanosheet from this sample. Again, no K was found but the main peaks show the presences of Ca, Nb, Pr and O, while the other impurity peaks are not related to the sheets.

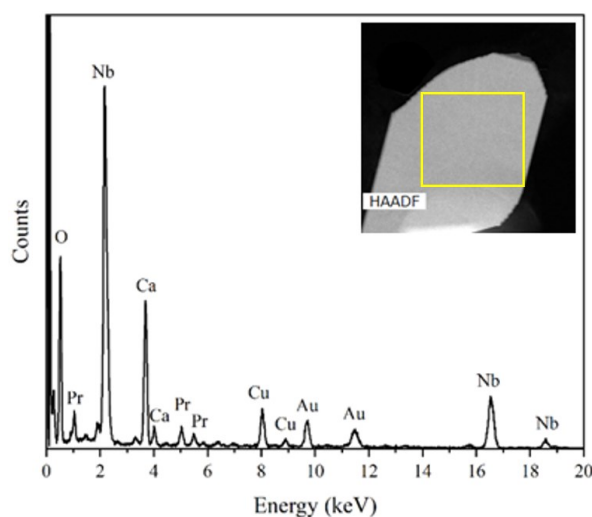


**Figure 6.2** EDX spectrum of an individual  $\text{Pr}^{3+}$  doped  $\text{Ca}_2\text{Nb}_3\text{O}_{10}$  nanosheet synthesized with a higher Pr content and corresponding HAADF image where the area of data acquisition is marked.

EDX data sets of several individual nanosheets were taken, analysed and quantified to obtain the average elemental composition of the sheets. The results for fifteen nanosheets (ten with higher Pr content and five with lower Pr content) were averaged and are presented in table 6.1. For single nanosheets with a higher Pr content, the averaged atomic percentage were obtained as follows: 58.1 at% O, 14.5 at% Ca, 25.6 at% Nb and 1.8 at% Pr. Moreover, Ca and Nb over Pr ratios are calculated and averaged and also listed in table 6.1. The same analysis was done for the single sheets with a low Pr content. The averaged results are given as: 52.0 at% O, 17.9 at% Ca, 27.2 at% Nb and 0.9 at% Pr. Comparing the average atomic percent for Ca and Nb for the different types of sheets revealed that a different number of Ca and Nb were substituted by Pr. The average Pr concentration for the high Pr content sheets (1.8 at%) is doubled compared to the Pr concentration for the lower Pr content sheets (0.9 at%).

**Table 6.1** EDX measurements on several individual nanosheets

Type of nanosheets	<b>O<sub>ave</sub></b> <b>(at%)</b>	<b>Ca<sub>ave</sub></b> <b>(at%)</b>	<b>Nb<sub>ave</sub></b> <b>(at%)</b>	<b>Pr<sub>ave</sub></b> <b>(at%)</b>	<b>(Ca/Pr)<sub>ave</sub></b>	<b>(Nb/Pr)<sub>ave</sub></b>
High Pr content	58.1	14.5	25.6	1.8	8.4	14.7
Standard deviation	11	3.5	7.1	0.5	0.9	1.1
Low Pr content	52.0	17.9	27.2	0.9	19.8	30.6
Standard deviation	13.1	4.8	5.9	0.2	1.1	4.1

In summary, based on the EDX results, we can conclude that the nanosheets synthesized with different Pr content indeed contained different amount of Pr, while nanosheets synthesized with the same Pr content had the same Pr atomic ratio with a low standard deviation (see table 6.1) independent of the sheet thickness. Since there was no trace of K, the exfoliation process was successful. Average Pr concentration for the nanosheets synthesized with high Pr content is twice more than the nanosheets synthesized with low Pr content. This indicates that part of the Pr cannot be incorporated in the lattice and that a solubility limit exists for the nanosheets. Comparing the Pr concentration in the nanosheets to the bulk samples [49], it is understood that Pr concentration in the nanosheets can go up to less than 2 at%. In the bulk sample prepared from the same  $\text{KCa}_2\text{Nb}_3\text{O}_{10}$  precursor this amount was around 10 at% which had crystallized in a different structure ( $\text{Pr}^{3+}$ :  $\text{Ca}_2\text{Nb}_2\text{O}_7$ ). It is important to mention that a high amount of Pr content was used to synthesize bulk particles, and as a result two different phases with different crystal structures, namely  $\text{PrNbO}_4$  and  $\text{Pr}^{3+}$ :  $\text{Ca}_2\text{Nb}_2\text{O}_7$  were produced. To prevent phase separation, a lower amount

of Pr content was used in the bulk particles which were used for exfoliation [ $K_{1-x}Ca_{2-x}Pr_xNb_3O_{10}$ ,  $x= 0.05$  and  $0.50$ ].

### 6.3.2. Structural analysis of the nanosheets in (S)TEM

Structural investigations of  $Pr^{3+}$  doped 2D nanosheets with lower Pr content were carried out in the Cs-corrected (S)TEM. As shown in Fig.6.3.a, nanosheets are laying on top of each other. To further study the atomic structure, one thin region (marked in yellow) was chosen. An HRTEM image of the selected area is illustrated in Fig.6.3.b. The region was oriented in  $[001]$  as determined by the FFT pattern. The FFT pattern has no additional (rotated) reflections. The crystal has a monoclinic structure like the bulk  $KCa_2Nb_3O_{10}$  precursor (ICSD 157839-see Fig.4.a) but with only three layers of connected Nb-O octahedra with Ca ions positioned in between and the K layers removed. In Fig. 6.4 b and c, the pseudo 2D crystal structure of  $[Ca_2Nb_3O_{10}]^-$  in  $[100]$  and  $[001]$  is viewed. A similar structure was observed for undoped nanosheets by Viridi et al.[109] By using atomic force microscopy (AFM) measurements, they reported the thickness of a single nanosheet to be between 1.85 and 3 nm. The latter was due to the presence of  $TBA^+$  molecules on top of the surface.[109] Moreover, Li. et al.[110], observed a thickness of 1.85 nm for undoped nanosheet using AFM under vacuum conditions.

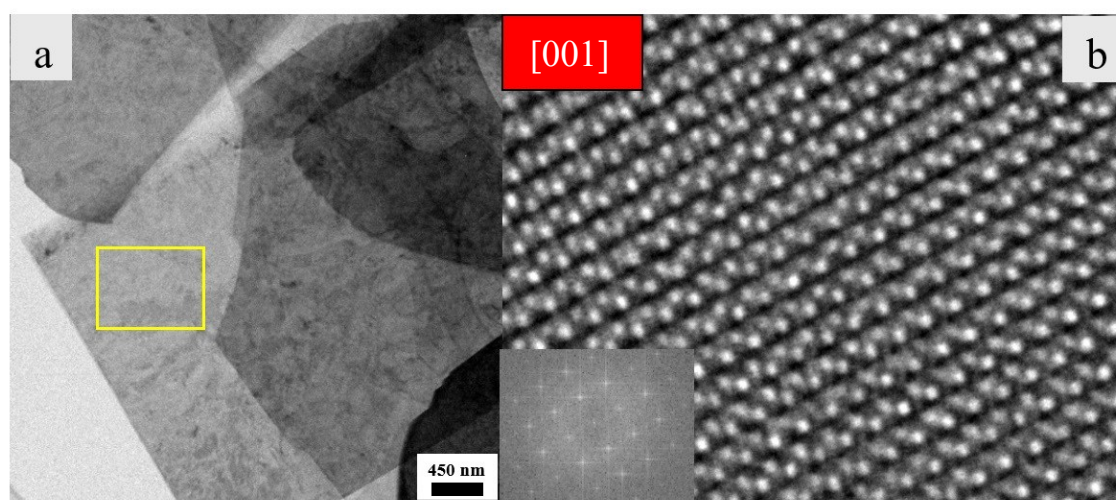


**Figure 6.3** (a) BF TEM image of an assembly of 2D nanosheets. (b) HRTEM image of the marked area indicated in yellow in (a), showing a set of stacked nanosheets taken in  $[001]$  zone axis; the inset indicates the FFT pattern.

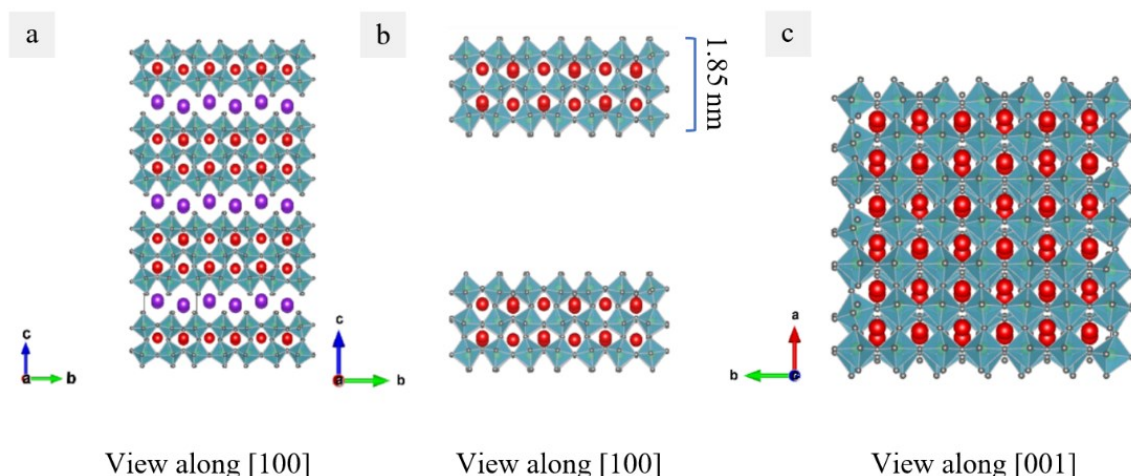


**Figure 6.4** Crystal structure of (a)  $\text{KCa}_2\text{Nb}_3\text{O}_{10}$  viewed in  $[100]$  and pseudo 2D  $[\text{Ca}_2\text{Nb}_3\text{O}_{10}]^-$  viewed in (b)  $[100]$  and (c)  $[001]$  (red spheres, Calcium; gray, Oxygen and purple, Potassium); Nb (shown with green spheres) is located within the centre of the octahedra.

To obtain HRTEM images a negative  $C_s$  value was used. This condition gives enhanced contrast due to contributions of both amplitude and phase contrast.[45] According to [47], an optimum contrast for samples up to 4 nm thickness is achieved if a negative  $C_s$  value with a positive defocus is used.

Multislice simulations were carried out for the pseudo 2D structure of  $[\text{Ca}_2\text{Nb}_3\text{O}_{10}]^-$  nanosheets along the  $[001]$  direction. The simulations were done to determine the thickness of the sheets and indicate the atomic positions of Nb, Ca and O. According to [49][79], possible sites substituted by Pr could be Ca and Nb. The corresponding thickness-defocus map is shown in Fig.6.5. In the simulated images, the thickness and the defocus values vary between 2.97-11.89 nm and 10-70 nm, respectively. The marked areas are compared with the HRTEM images taken at different defocus values. It is important to note that a larger thickness than 1.85 nm would indicate i) the presence of  $\text{TBA}^+$  molecules and ii) that some of the sheets remain stacked as in the bulk even after exfoliation.

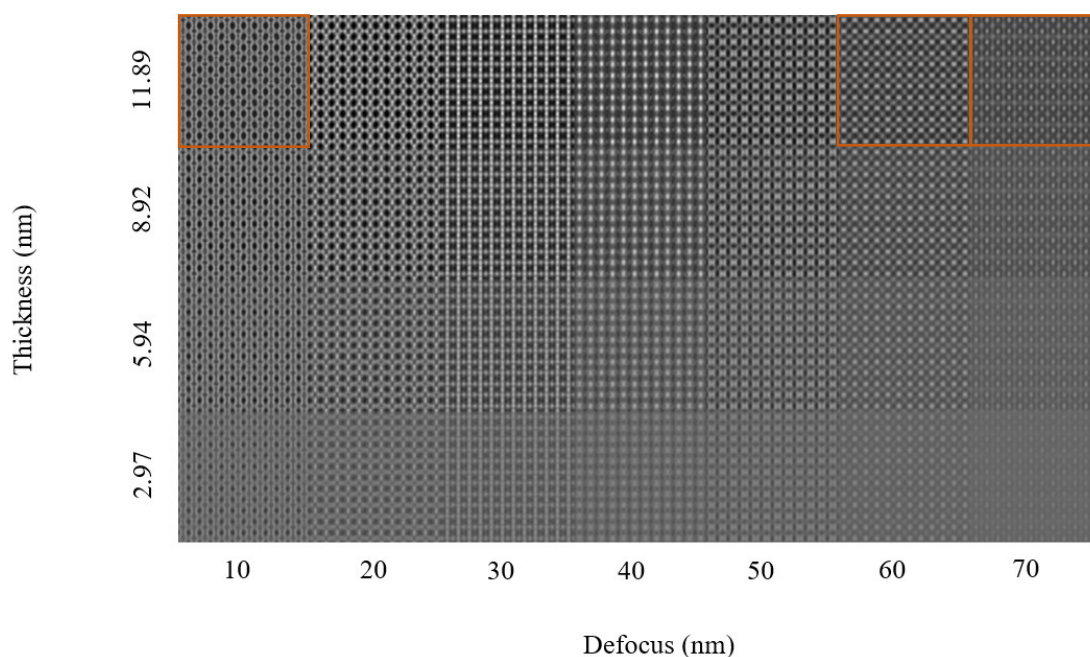


**Figure 6.5** Defocus-thickness map of pseudo 2D  $[\text{Ca}_2\text{Nb}_3\text{O}_{10}]^-$  nanosheet viewed along  $[001]$  and simulated with the multislice method. Accelerating voltage = 300 kV,  $C_s = -0.01$  mm.

HRTEM images were taken at a thicker nanosheet for different defocus values. The results are compared with the simulated images and displayed in Fig.6.6. As seen on this image, the simulated images (shown with a red frame) resemble the contrast of the experimental HRTEM images. The difference in the contrast we believe is related to the pseudo 2D structure defined in the CIF file (presence of vacuum slab). Moreover, astigmatism and small-angle misalignments in the experiment, as well as minor differences of defocus or spherical aberration values in the simulation should be mentioned. For the defocus value 10 nm and thickness around 11.89 nm, the best fit was obtained. For this condition, Ca atoms are giving a bright contrast. On the other hand, Nb and O atoms appear dark. For defocus value 60-70 nm and the same thickness, all atoms Ca, Nb and O atoms show a bright contrast. Based on Fig.6.6.b, we conclude that in Fig.6.3, the thin area is most likely a set of 4 nanosheets stacked turbostratically in  $z$ -direction on top of each other. Brighter spots in that image indicate the location of Ca atoms and pale spots reveal where octahedra (with Nb and O atoms sitting at the centre and on the corners, respectively) are positioned.

The atomic position of O, Nb and Ca atoms marked with colored spheres as well as the octahedra are shown on the simulated images (Fig.6.6). There is no hint for the Pr atoms in

the HRTEM images which might be due to the very low concentration of the dopant and the fact that different individual atoms in a regular lattice cannot be recognised by HRTEM.

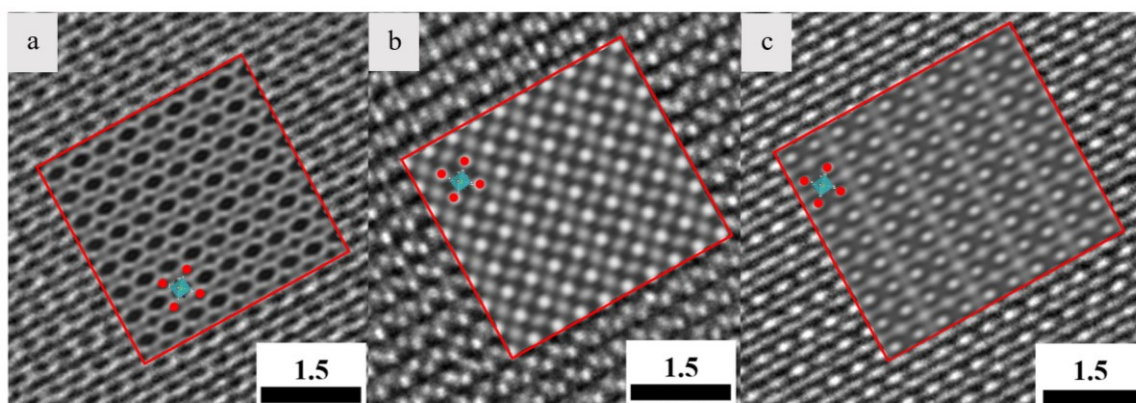


**Figure 6.6** Experimental HRTEM images superimposed with simulated images of pseudo 2D [Ca<sub>2</sub>Nb<sub>3</sub>O<sub>10</sub>] nanosheet along [001] with a thickness value=11.89 nm for (a) defocus value=10 nm, (b) defocus value=60 nm, and (c) defocus value=70 nm. Simulated images are marked with red frames. Red, green and gray spheres indicate Calcium, Niobium and Oxygen, respectively. Nb is located inside the octahedra.

To be able to observe Pr atoms, STEM imaging on a thicker sheet with a high Pr content was performed (Fig.6.7.a). Fig.6.7.b represents the HRSTEM of the thicker nanosheet in [001]. The inset in this image shows the FFT pattern. Since in HAADF imaging, the contrast is  $Z$  dependent, the atomic columns with the brightest contrast should be indicating Pr atoms' locations. As seen on our HRSTEM image, a homogenous contrast in the atomic columns is observed. This could be due to the fact that Pr concentration is too low to be noticeably detected in addition to the fact that that STEM always gets an integral value of the whole atomic column. Only if the Pr atoms would arrange in one atomic column, they might have been visible. Thus, the fact that we cannot identify them means that they are homogeneously embedded within the sheets.



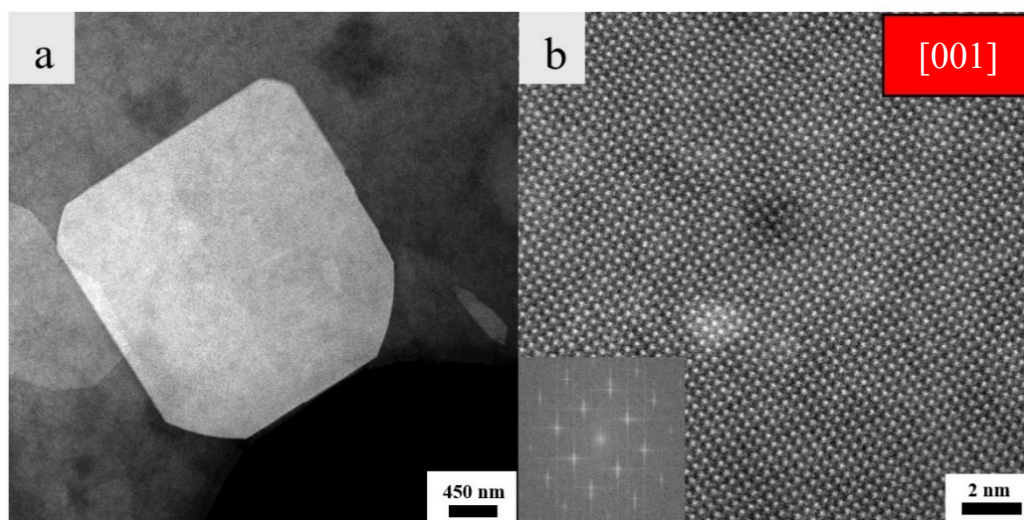


**Figure 6.7** (a) STEM image of an individual thicker nanosheet with a high Pr content on top of the carbon support and (b) HRSTEM-HAADF image of the same nanosheet taken in [001]. The inset indicates the FFT pattern of the single sheet.

### 6.3.3. CL analysis of the nanosheets

CL measurements were carried out for nanosheets with a higher Pr content. One spectrum as the representative is shown in Fig.6.8. Since Pr concentration for the nanosheets is low (1.8 at%), in total CL intensity is lower compared to the bulk particles which had a Pr content larger than 10 at%.[49] The positions of the emission lines are labeled.  $^3P_0\text{-}^3H_4$ ,  $^3P_0\text{-}^3H_6$  and  $^3P_2\text{-}^3F_3$  are the common transitions observed in the spectra of bulk particles, namely,  $\text{PrNbO}_4$  and  $\text{Pr}^{3+}:\text{Ca}_2\text{Nb}_2\text{O}_7$ . However, the  $^3P_0\text{-}^3H_4$  transition has a significantly lower intensity compared to the bulk. This transition is the dominant transition in lanthanide doped materials and can be employed for lasing activities in the material preparation.[72] Other transitions related to  $^3P_1\text{-}^3H_6$  (597 nm),  $^1D_2\text{-}^3H_4$  (603 nm) and  $^1I_6\text{-}^3F_2$  (610 nm) are observed only in the spectra of the nanosheets. These transitions are close to the orange light emission in the visible spectrum (600 nm), therefore, they can be used in applications where orange emission is needed. According to [71], the emission from the  $^1D_2$  level is greatly dependent on the interaction between two nearby  $\text{Pr}^{3+}$  ions. They showed that by increasing Pr concentration, the peak related to  $^1D_2$  level disappeared in their PL data. When the  $\text{Pr}^{3+}$  concentration increases, the distance between  $\text{Pr}^{3+}$  ions decreases; as a result, concentration quenching becomes more frequent. Our result confirms this because only in

the case of nanosheets with averaged Pr concentration of 1.8 at%, the transition belonging to  $^1D_2-^3H_4$  was detected and not in  $\text{PrNbO}_4$  and  $\text{Pr}^{3+}:\text{Ca}_2\text{Nb}_2\text{O}_7$ . [49]

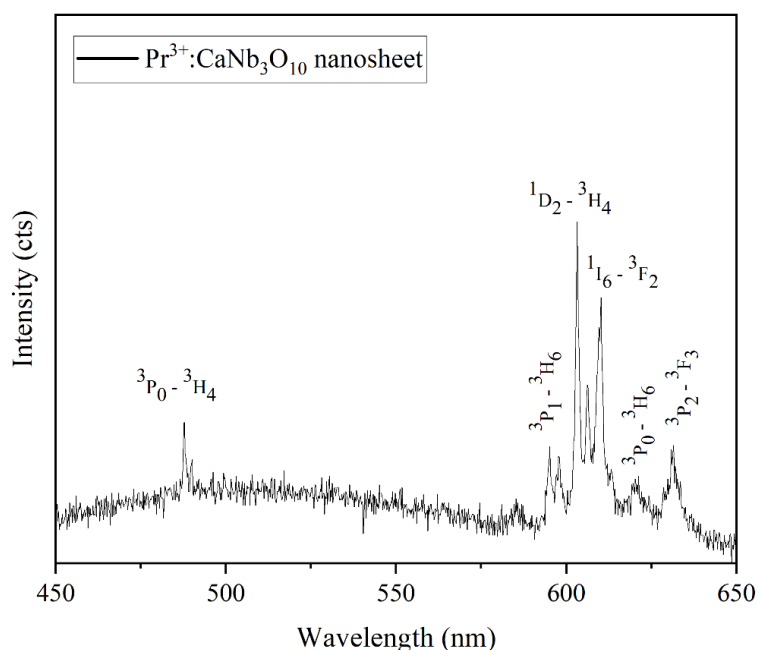


**Figure 6.8** CL spectrum of an individual  $\text{Pr}^{3+}:\text{CaNb}_3\text{O}_{10}$  nanosheet. Major peaks were labelled according to the Dieke diagram [25].

## 6.4. Conclusion

$\text{Pr}^{3+}$  doped  $\text{Ca}_2\text{Nb}_3\text{O}_{10}$  nanosheets synthesized with two different Pr contents were studied. Nanosheets synthesized with a higher Pr content had the highest Pr concentration (1.8 at%), whereas for the sheets with the lower Pr content, this amount was only 0.9 at%. The structure of the nanosheets was investigated by HRTEM and HRSTEM. It was found out that the nanosheets have the same structure as the monoclinic  $\text{KCa}_2\text{Nb}_3\text{O}_{10}$  but with only three layers of connected Nb-O octahedra with Ca ions located in between and the K completely removed. Different thicknesses for the sheets were observed, the lowest in the range of 3 nm (corresponding to a single sheet when taking  $\text{TBA}^+$  molecules on top and bottom of the nanosheet into account), others up to 12 nm. The latter indicates that after exfoliation, some of the layers of the bulk structure remained stacked, leading also to a FFT pattern with only one set of reflections. Considering the presence of  $\text{TBA}^+$  molecules, at least 4 layers formed the thicker nanosheets as exemplarily shown with the help of multislice image simulations. CL analysis was done only on the nanosheets with the higher

Pr content. Compared to the different bulk phases [49], additional peaks close to 600 nm region of the visible spectrum were observed.

On the basis of these results and our previous publications [49][79], we conclude that bulk particles ( $\text{PrNbO}_4$  and  $\text{Pr}^{3+}:\text{Ca}_2\text{Nb}_2\text{O}_7$ ) have brighter emission lines (especially transitions belonging to the dominant peaks:  ${}^3\text{P}_0\text{-}{}^3\text{H}_4$  and  ${}^3\text{P}_2\text{-}{}^3\text{F}_4$ ). However, 2D nanosheets ( $\text{Pr}^{3+}:\text{CaNb}_3\text{O}_{10}$ ) with additional sharp emission lines around 600 nm and smaller size are potential candidates to be used in other applications where the mentioned wavelength (orange color) is needed.



## 7. Summary and Outlook

The scope of this thesis is to understand the luminescence properties of lanthanide doped niobates and lanthanide niobate compounds, and to determine the factors which enhance that. Two factors were introduced and investigated as the main reasons for luminescence: The lanthanide concentration and the presence of defects such as twins.

During the annealing process of  $\text{Pr}^{3+}$  doped  $\text{KCa}_2\text{Nb}_3\text{O}_{10}$ , complex niobates with different phases  $\text{PrNbO}_4$  and  $\text{Pr}^{3+}:\text{Ca}_2\text{Nb}_2\text{O}_7$  were formed.[49] The solubility limit of Pr in  $\text{Pr}^{3+}$  doped  $\text{KCa}_2\text{Nb}_3\text{O}_{10}$  is the reason for the formation of the two phases during annealing. K was evaporated completely, and replaced by Pr. XRD and TEM measurements verified a monoclinic crystal structure (space group: C2/c) with lattice parameters  $a = 5.499 \text{ \AA}$ ,  $b = 5.157 \text{ \AA}$ ,  $c = 11.342 \text{ \AA}$ , and  $\alpha = 90^\circ$ ,  $\beta = 94.57^\circ$ ,  $\gamma = 90^\circ$  for  $\text{PrNbO}_4$ . For the other phase, a cubic crystal structure  $\text{Ca}_2\text{Nb}_2\text{O}_7$  (space group: Fd-3m) with a lattice parameter  $a = 10.445 \text{ \AA}$  was found. Based on the XRD results, it was understood that there exists an increase in the interplanar spacing which is due to the Pr ions sitting on Nb sites within the  $\text{Ca}_2\text{Nb}_2\text{O}_7$  crystal lattice. The crystal lattice strain was calculated accordingly and the result was 0.5%.

As proven by EDX,  $\mu\text{m}$ -sized  $\text{PrNbO}_4$  particles consist beside oxygen of Pr and Nb with almost constant ratio of Nb/Pr  $\approx 0.9$ . Therefore, based on the off-stoichiometric ratio of Pr:Nb, a small fraction of the Pr ions should be located on Nb sites within the  $\text{PrNbO}_4$  crystal structure. For the second phase, Ca and Nb are partly replaced by Pr. A chemical formula was obtained as  $\text{Pr}_x\text{Ca}_{48-x/2}\text{Nb}_{52-x/2}\text{O}_y$ , for this phase. The average composition of x is 20 at%. The  $d$  spacing value corresponding to the (111) plane was calculated based on the diffraction pattern of a  $\text{Pr}^{3+}:\text{Ca}_2\text{Nb}_2\text{O}_7$  particle. Comparing the  $d$  spacing in this case (6.4  $\text{ \AA}$ ) with the one from the ICSD theoretical data (6.03  $\text{ \AA}$ ), the increase in the  $d$  value in the experimental data confirms that Pr should be sitting on Ca and Nb sites almost equally. As mentioned in [54,55], multiple sites are present in the lattice of lanthanide-doped materials. In this work it was shown that that  $\text{Pr}^{3+}$  ions enter the  $\text{ABNbO}_3$  structure with A and B being alkali and alkaline earth metals not only by substituting A(K) and B(Ca) but also by substituting Nb lattice positions. In the CL spectra of both phases, dominant electric dipole transitions of Pr, namely  $^3\text{P}_0$  to  $^3\text{H}_4$  (489 nm) and  $^3\text{P}_2$  to  $^3\text{F}_4$  (653 nm), were observed. Comparing the emission spectra for both phases it was found out that the  $\text{PrNbO}_4$  has brighter emission lines. Due to a high amount of Pr, both K and Ca atoms of the  $\text{KCa}_2\text{Nb}_3\text{O}_{10}$  host were substituted by Pr. This creates a unique surrounding for  $\text{Pr}^{3+}$  ions

(Pr<sup>3+</sup> ions occupy the sites with C<sub>2</sub> symmetry) which helps overcome the parity forbidden rule and promotes very sharp f-f transitions. Thus, PrNbO<sub>4</sub> is a better optical candidate and should be produced directly in the future.

Phase transformation twinning as a result of monoclinic distortions during the synthesis was investigated as another factor contributing to the luminescence of PrNbO<sub>4</sub> particles.[79] The nature of the twins is ferroelastic and are generated by stress.[84] A new correlative approach using BSE imaging, CL spectroscopy, FIB lamella lift out and HR(S)TEM was used at the same location within the particles. TEM observation of the particles revealed the presence of twins with different densities. The twin domains vary in size; the twin width can be measured as less than 20 nm in one region, while it can increase to more than 50 nm in other regions. Coherent structure for the dominant type of the twins (twins with higher density) was further proved by TEM. Based on the HRTEM and HRSTEM images, the twin boundary plane was indexed as (30 $\bar{1}$ ). As proven by a combination of BSE imaging technique and CL, areas with high twin density show brighter emission lines compared to the areas with low twin density. However, the peaks associated with <sup>3</sup>P<sub>0</sub> to <sup>3</sup>H<sub>4</sub> and <sup>3</sup>P<sub>2</sub> to <sup>3</sup>F<sub>4</sub> had significantly higher intensity in the CL spectra for both high density and low density twinned areas. In order to show that the CL signal is only coming from the twinned regions, Monte Carlo electron trajectory simulations in PrNbO<sub>4</sub> using the software Casino were performed with the same parameters as in the experiment. It was understood that the penetration depth of the electrons is up to 500 nm. Thus, the interaction volume is smaller than the particle size and a large twinned area is contributing to the observed CL signal.

As mentioned in [99], any type of local distortions including defects such as vacancies or dislocations increase the relative intensity of the transitions; thus, observing higher intensity for highly twinned areas can be explained. The perturbation of the energy states caused by the defects leads to the occurrence of the parity forbidden f-f transitions. Due to the existence of the outer 5s and 5p electrons, the inner shell f-f transitions in lanthanide compounds are very well shielded and therefore not sensitive to the surrounding environment. However, in case of hypersensitive transitions the intensities are influenced significantly by a small change in the surrounding environment.[98,111,112] The transition associated with <sup>3</sup>P<sub>2</sub> to <sup>3</sup>F<sub>4</sub> is a hypersensitive transition and that explains why higher intensity is observed for this one compared to the other transitions.

Further TEM investigations revealed other twin types for PrNbO<sub>4</sub> particles. HRTEM of a conventionally prepared sample showed a twin boundary plane (200) with inclined twin

planes (161). The similar angle between the twin boundary plane and the conjugate twin plane on both sides implied a mirror symmetry. As a result, it was found out that these twins are coherent.

The third twin type called deformation twin was observed on PrNbO<sub>4</sub> which were crushed with a mortar. These twins have a lens like shape and are formed at the rims of a crystal due to the excess of strain energy. Since this type of twinning was the minority, CL spectra on these particles were not acquired.

Another type of material which was studied in this work are 2D nanosheets. According to [104,107], lanthanide 2D materials should have better luminescent properties compared to their bulk counterpart. Two types of nanosheets with a low and a high Pr content with a nominal formula K<sub>1-x</sub>Ca<sub>2-x</sub>Pr<sub>x</sub>Nb<sub>3</sub>O<sub>10</sub>, [x= 0.05 and 0.50] were synthesized. EDX measurements on several Pr doped nanosheets proved that the nanosheets contained different amount of Pr, however, the ratio of Ca/Pr and Nb/Pr remained constant within each group (low and high doped sheets). Structural analysis of the nanosheets was done in (S)TEM. It was found out that the sheets have a monoclinic crystal structure which is the same as in the bulk KCa<sub>2</sub>Nb<sub>3</sub>O<sub>10</sub> particles. In the STEM EDX data no K was observed; thus they consist of only three layers of connected Nb-O octahedra with Ca ions located in between. Using a multislice simulation method, the thickness of a single nanosheet was estimated to be minimum 3 nm which was in agreement with literature.[109] The atomic location of O, Ca and Nb were determined in the simulated images. Based on our detailed study on the bulk particles, we believe that Pr should be located either on Ca or Nb sites. However, due to a very low concentration of Pr atoms, it was not possible to detect Pr atoms in the STEM-HAADF images. Additional peaks were observed in the CL spectra of the sheets.

The work in hand demonstrates the importance of electron microscopy to understand the optical properties of lanthanide (doped) oxides; and the influence of lanthanide content and the formation of twins on the luminescent properties of the material. Electron microscopy techniques enable an atomic scale local analysis that gives detailed insight into individual micro metre particle or nanosheets. SEM and EDX measurements were performed to study the morphology and the chemical composition of the formed phases during the synthesis of the material. XRD analysis was conducted to confirm the crystal structure of the phases. FIB was successfully applied to cut a region of interest with high density of twins. BSE imaging was used as a technique to find the regions with high density of twins on the

particles and emission spectra were acquired by CL. TEM investigations helped to obtain information in the nanometre scale, including the crystal structure of different phases as well as twin structure by investigating highly twined areas.

This work presents a multi-technique correlative study which makes it unique compared to the other studies on lanthanides. In order to expand the investigation to other lanthanides and the influence of the crystal structure, crystal defects and lanthanide concentrations on the luminescence, it is essential to or to investigate agglomerates of the sheets. use a multi technique approach which includes EDX, CL and TEM on individual particles. Moreover, to be able to see the impact of lanthanide 2D nanosheets on the luminescence, it is crucial to synthesize the sheets with an optimum amount of lanthanide dopants. More research needs to be carried out to determine the optimum amount. Based on the knowledge gained in this thesis, lanthanide orthoniobates have the strongest luminescent brightness, and should be suggested for optical applications.



## 8. References

1. Ganjali MR, Gupta VK, Faridbod F, Norouzi P. Lanthanides Series Determination by Various Analytical Methods. Lanthanides Series Determination by Various Analytical Methods. Elsevier Inc.; 2016. 1–437 p.
2. Beatty R. The lanthanides. Cavendish Square Publishing; 2008. 32 p.
3. Kolesov R, Xia K, Reuter R, Stöhr R, Zappe A, Meijer J, Hemmer PR, Wrachtrup J. Optical detection of a single rare-earth ion in a crystal. *Nat Commun.* 2012 Aug 28;3(1):1–7.
4. Bünzli J-CG, Eliseeva S V. Basics of Lanthanide Photophysics. In: Lanthanide Luminescence. Springer, Berlin, Heidelberg; 2010. p. 1–45.
5. Liu G, Jacquier B. Spectroscopic Properties of Rare Earths in Optical Materials. Hull R, Parisi J, Osgood RM, Warlimont H, editors. Berlin, Heidelberg: Springer Berlin Heidelberg; 2005. (Springer Series in Materials Science; vol. 83).
6. Malta OL, Carlos LD. Intensities of 4f-4f transitions in glass materials. *Quim Nova.* 2003;26(6):889–95.
7. Reisfeld R. Optical properties of lanthanides in condensed phase, theory and applications. *AIMS Mater Sci.* 2015;2(2):37–60.
8. Gaft M, Reisfeld R, Panczer G. Modern Luminescence Spectroscopy of Minerals and Materials. Cham: Springer International Publishing; 2005. (Springer Mineralogy).
9. Gan FX. Optical and Spectroscopic Properties. Springer-Verlag; 1992. 283 p.
10. Reisfeld R. Radiative and non-radiative transitions of rare-earth ions in glasses. *Rare Earths.* 2007 Dec 13;123–75.
11. Reisfeld R. Multiphonon Relaxation in Glasses. *Radiationless Process.* 1980;489–98.
12. Binnemans K. Lanthanide-based luminescent hybrid materials. *Chem Rev.* 2009 Sep 9;109(9):4283–374.

13. Lima ARF, Sczancoski JC, Siu Li M, Longo E, Camargo ER. Structural characterization and photoluminescence behavior of pure and doped potassium strontium niobates ceramics with tetragonal tungsten-bronze structure. *Ceram Int.* 2016 Mar 1;42(4):4709–14.
14. Cotton S. *Lanthanide and Actinide Chemistry*. S. Komiya, editor. John Wiley & Sons, Ltd; 2006. 1–263 p.
15. Sinha SP. *Systematics and the Properties of the Lanthanides*. Springer Netherlands; 1983.
16. Liddle ST, Mills DP, Natrajan LS. penny. World scientific; 2022.
17. Kim DW, Kwon DK, Yoon SH, Hong KS. Microwave dielectric properties of rare-earth ortho-niobates with ferroelasticity. *J Am Ceram Soc.* 2006 Dec;89(12):3861–4.
18. Kelly PM, Wauchope CJ. The origin of the domain structure in  $\text{LaNbO}_4$ . *Mater Lett.* 1996 May 1;27(1–2):7–11.
19. Atif R, Zarkov A, Asuigui DRC, Glaser P, Stewart O, Stoll SL. Single-Source Precursors for Lanthanide Diselenide Nanosheets. *Chem Mater.* 2019 Sep 24;31(18):7779–89.
20. Atwood DA, editor. *The Rare Earth Elements: Fundamentals and Applications*. John Wiley & Sons, Ltd; 2013.
21. Coplen by NEH and T. *The Periodic Table of the Elements*. Chem Int,; Newsmag IUPAC. 2014 Jan 1;26(1):8–9.
22. Griffiths DJ, Schroeter DF. *Introduction to Quantum Mechanics*. Cambridge University Press; 2018.
23. Hehlen MP, Brik MG, Krämer KW. 50th anniversary of the Judd–Ofelt theory: An experimentalist’s view of the formalism and its application. *J Lumin.* 2013 Apr 1;136:221–39.
24. Walsh BM. Judd-Ofelt theory: principles and practices. In: *Advances in Spectroscopy for Lasers and Sensing*. Springer Netherlands; 2006. p. 403–33.

25. Dieke GH, Crosswhite HM. The Spectra of the Doubly and Triply Ionized Rare Earths. *Appl Opt.* 1963 Jul 1;2(7):675–86.
26. Kück S. Laser-related spectroscopy of ion-doped crystals for tunable solid-state lasers. *Appl Phys B Lasers Opt.* 2001;72(5):515–62.
27. Neamen DA. *Semiconductor physics and devices.* Vol. 9. McGraw-Hill; 2006. 57 p.
28. Yu PY, Cardona M. *Fundamentals of semiconductors: physics and materials properties.* Vol. 198. Springer; 2010. 775 p.
29. Sze SM, Ng KK. *Physics of Semiconductor Devices.* John Wiley & Sons, Inc.; 2006.
30. Pierret RF. *Semiconductor Device Fundamentals.* Addison-Wesley; 1996. 792 p.
31. Hamaguchi C. *Basic semiconductor physics: Second edition.* Springer Berlin Heidelberg; 2010. 570 p.
32. Ziegler C. *Two-Dimensional Transition Metal Oxide Nanosheets for Nanoarchitectonics.* Ludwig Maximilian University of Munich; 2015.
33. Yang J, Zhao M, Shahid M, Feng J, Wan C, Pan W. Electronic structure, anisotropic elastic and thermal properties of monoclinic  $\text{Ca}_2\text{Nb}_2\text{O}_7$ . *Ceram Int.* Elsevier Ltd; 2016.
34. Detail information of  $\text{PrNbO}_4$  | Catalyst Database, First database in catalyst field [Internet]. Available from: <http://www.catalysthub.net/materials.php?id=1812695>
35. Reimer L. *Scanning electron microscopy: physics of image formation and microanalysis.* Springer-Verlag; 1985. 457 p.
36. Williams DB, Carter CB. *Transmission electron microscopy: A textbook for materials science.* *Transmission Electron Microscopy: A Textbook for Materials Science.* Springer US; 2009. 1–760 p.
37. Goodhew PJ, Humphreys J, Beanland R. *Electron Microscopy and Analysis, Third Edition.* Taylor and Francis, 2001;
38. Goldstein JI, Newbury DE, Michael JR, Ritchie NWM, Scott JHJ, Joy DC. *Scanning electron microscopy and x-ray microanalysis.* *Scanning Electron Microscopy and X-*

- ray Microanalysis. Springer New York; 2017. 1–550 p.
39. Pennycook SJ, Nellist PD (Peter D. Scanning transmission electron microscopy : imaging and analysis. Springer; 2011. 762 p.
  40. Brandon DG, Kaplan WD. Microstructural Characterization of Materials. 2013. 560 p.
  41. Everhart TE, Thornley RFM. Wide-band detector for micro-microampere low-energy electron currents. *J Sci Instrum.* 1960;37(7):246–8.
  42. Yacobi BG, Holt DB. Cathodoluminescence Microscopy of Inorganic Solids. Cathodoluminescence Microscopy of Inorganic Solids. Springer US; 1990.
  43. Panchromatic Cathodoluminescence Imaging - Nanoscience Instruments [Internet]. Available from:  
<https://www.nanoscience.com/techniques/cathodoluminescence/panchromatic-cathodoluminescence-imaging/>
  44. Lupini AR, Rashkeev SN, Varela M, Borisevich AY, Oxley MP, Van Benthem K, Peng Y, De Jonge N, Veith GM, Pennycook TJ, Zhou W, Ishikawa R, Chisholm MF, Pantelides ST, Pennycook SJ. CHAPTER 2: Scanning transmission electron microscopy. *RSC Nanosci Nanotechnol.* 2015;2015(37):30–79.
  45. Urban KW, Jia CL, Houben L, Lentzen M, Mi SB, Tillmann K. Negative spherical aberration ultrahigh-resolution imaging in corrected transmission electron microscopy. *Philos Trans R Soc A Math Phys Eng Sci.* 2009 Sep 28;367(1903).
  46. Jia CL, Houben L, Thust A, Barthel J. On the benefit of the negative-spherical-aberration imaging technique for quantitative HRTEM. *J Ultramic.* 2009;110(5):500–5.
  47. Lee Zh, Kaiser U. Calculation of optimum contrast for HRTEM images of SiC and graphene at medium and lower voltages. Ulm University. 2009.
  48. Hosokawa F, Sawada H, Kondo Y, Takayanagi K, Suenaga K. Development of Cs and Cc correctors for transmission electron microscopy. *J Microsc.* 2013 Feb 1;62(1):23–41.

49. Changizi R, Zhang S, Ziegler C, Schwarz T, Lotsch B V., Scheu C. Correlation between Structural Studies and the Cathodoluminescence of Individual Complex Niobate Particles. *ACS Appl Electron Mater.* 2021 Jan 26;3(1):461–7.
50. Hu M, Liu W. Application of lanthanide-doped luminescence nanoparticles in imaging and therapeutics. *Photonanotechnology Ther Imaging.* 2020 Jan 1;205–41.
51. Wang S, Wang L. Lanthanide-doped nanomaterials for luminescence detection and imaging. *TrAC Trends Anal Chem.* 2014 Nov 1;62:123–34.
52. Kittel C, McEuen P. *Introduction to solid state physics.* 8th ed. John Wiley & Sons, Inc., 2005; 692 p.
53. Ferreira da Rosa PP, Kitagawa Y, Hasegawa Y. Luminescent lanthanide complex with seven-coordination geometry. *Coord Chem Rev.* 2020 Mar 1;406:213153.
54. Pin S, Piccinelli F, Upendra Kumar K, Enzo S, Ghigna P, Cannas C, Musinu A, Mariotto G, Bettinelli M, Speghini A. Structural investigation and luminescence of nanocrystalline lanthanide doped  $\text{NaNbO}_3$  and  $\text{Na}_{0.5}\text{K}_{0.5}\text{NbO}_3$ . *J Solid State Chem.* 2012 Dec 1;196:1–10.
55. Morais Faustino BM, Foot PJS, Kresinski RA. Lanthanide luminescence sensitization via  $\text{SnO}_2$  nanoparticle host energy transfer. *J Lumin.* 2019 Feb 1;206:205–10.
56. Krishnan R, Swart HC. Cathodoluminescence properties of monoclinic phased reddish-orange emitting  $\text{BaY}_2(\text{MoO}_4)_4:\text{Eu}^{3+}$  phosphor. *Opt Mater (Amst).* 2020 Jan 1;99:109604.
57. Chen H, Wang Y. Photoluminescence and cathodoluminescence properties of novel rare-earth free narrow-band bright green-emitting  $\text{ZnB}_2\text{O}_4:\text{Mn}^{2+}$  phosphor for LEDs and FEDs. *Chem Eng J.* 2019 Apr 1;361:314–21.
58. Nico C, Monteiro T, Graça MPF. Niobium oxides and niobates physical properties: Review and prospects. *Prog Mater Sci.* 2016 Jul 1;80:1–37.
59. Dzierzgowski K, Wachowski S, Gojtowska W, Jasiński P, Gazda M, Mielewczyk-Gryń A. Praseodymium substituted lanthanum orthoniobate: electrical and structural properties. *Ceram Int.* 2018;8210–5.

60. Dou R, Zhang Q, Gao J, Chen Y, Ding S, Peng F, Liu W, Sun D. Rare-Earth Tantalates and Niobates Single Crystals: Promising Scintillators and Laser Materials Crystals. 2018 Jan 24;8(2):55.
61. Vendrell X, García JE, Cerdeiras E, Ochoa DA, Rubio-Marcos F, Fernández JF, Mestres L. Effect of lanthanide doping on structural, microstructural and functional properties of  $K_{0.5}Na_{0.5}NbO_3$  lead-free piezoceramics. *Ceram Int.* 2016 Nov 15;42(15):17530–8.
62. Lorenz K, Nogales E, Miranda SMC, Franco N, Méndez B, Alves E, Tourbot G, Daudin B. Enhanced red emission from praseodymium-doped GaN nanowires by defect engineering. *Acta Mater.* 2013 May 1;61(9):3278–84.
63. Bizeto MA, Constantino VRL, Brito HF. Luminescence properties of the layered niobate  $KCa_2Nb_3O_{10}$  doped with  $Eu^{3+}$  and  $La^{3+}$  ions. *J Alloys Compd.* 2000 Oct 26;311(2):159–68.
64. Mhlongo GH, Dhlamini MS, Ntwaeaborwa OM, Swart HC, Hillie KT. Luminescent properties and quenching effects of  $Pr^{3+}$  co-doping in  $SiO_2:Tb^{3+}/Eu^{3+}$  nanophosphors. *Opt Mater (Amst).* 2014 Feb 1;36(4):732–9.
65. Adell I, Solé RM, Pujol MC, Aguiló M, Díaz F. Optimization of the Synthesis and Physical Characterization of Praseodymium-Doped Type III  $KGd(PO_3)_4$  Nanocrystals. *ACS Omega.* 2018 Sep 30;3(9):11307–16.
66. Diallo PT, Jeanlouis K, Boutinaud P, Mahiou R, Cousseins JC. Improvement of the optical performances of  $Pr^{3+}$  in  $CaTiO_3$ . *J Alloys Compd.* 2001 Jul 12;323–324:218–22.
67. Pan G, Bai X, Yang D, Chen X, Jing P, Qu S, Zhang L, Zhou D, Zhu J, Xu W, Dong B, Song H. Doping Lanthanide into Perovskite Nanocrystals: Highly Improved and Expanded Optical Properties. *Nano Lett.* 2017 Dec 13;17(12):8005–11.
68. Mir WJ, Sheikh T, Arfin H, Xia Z, Nag A. Lanthanide doping in metal halide perovskite nanocrystals: spectral shifting, quantum cutting and optoelectronic applications. *NPG Asia Mater* 2020 121. 2020 Jan 24;12(1):1–9.
69. Jusza A, Lipińska L, Baran M, Olszyna A, Jastrzębska A, Gil M, Mergo P,

- Piramidowicz R. Praseodymium doped nanocrystals and nanocomposites for application in white light sources. *Opt Mater (Amst)*. 2019 Sep 1;95:109247.
70. Cybińska J, Legendziewicz J, Boulon G, Bensalah A, Meyer G, Cybińska J, Legendziewicz J, Boulon G, Bensalah A, Meyer G. Assignment of spectroscopic properties in praseodymium-doped and praseodymium/ytterbium-co-doped ternary  $K_2LaX_5$  ( $X = Cl, Br, I$ ) Halides. *OptMa*. 2006;28(1–2):41–52.
  71. Li YC, Chang YH, Lin YF, Chang YS, Lin YJ. Luminescent properties of trivalent praseodymium-doped lanthanum aluminum germanate  $LaAlGe_2O_7$ . *J Phys Chem Solids*. 2007 Oct 1;68(10):1940–5.
  72. Kumar M, Parandamaiah M, Babu YCR, Kumar A. Spectral studies of praseodymium doped heavy metal borate glass systems. *Int J Eng Sci*. 2014;17–24.
  73. Luo W, Li R, Liu G, Antonio MR, Chen X. Evidence of Trivalent europium incorporated in anatase  $TiO_2$  nanocrystals with multiple sites. *J Phys Chem C*. 2008 Jul 17;112(28):10370–7.
  74. Faustino BMM, Foot PJS, Kresinski RA. Synthesis and photoluminescent properties of  $Sm^{3+}$ -doped  $SnO_2$  nanoparticles. *Ceram Int*. 2016 Dec 1;42(16):18474–8.
  75. Bouras K, Rehspringer JL, Schmerber G, Rinnert H, Colis S, Ferblantier G, Balestrieri M, Ihiawakrim D, Dinia A, Slaoui A. Optical and structural properties of Nd doped  $SnO_2$  powder fabricated by the sol–gel method. *J Mater Chem C*. 2014 Sep 18;2(39):8235–43.
  76. Chauhan I, Nigam S, Sudarsan V, Vatsa RK. Hetero-junction assisted improved luminescence of  $Eu^{3+}$  doped  $ZnO-SnO_2$  nanocomposite. *J Lumin*. 2016 Aug 1;176:124–9.
  77. Keller C. Über ternäre Oxide des Niobs und Tantals vom Typ  $ABO_4$ . *ZAAC - J Inorg Gen Chem*. 1962;318(1–2):89–106.
  78. Górecka N, Szczodrowski K, Lazarowska A, Barzowska J, Michalik D, Grinberg M. The influence of charge compensation defects on the spectroscopic properties of europium doped  $Ca_9Y(PO_4)_7$ . *RSC Adv*. 2017 Aug 16;7(64):40549–57.
  79. Changizi R, Zaefferer S, Abdellaoui L, Scheu C. Effects of Defect Density on

- Optical Properties Using Correlative Cathodoluminescence and Transmission Electron Microscopy Measurements on Identical PrNbO<sub>4</sub> Particles. *ACS Appl Electron Mater.* 2022 Apr 26;4(4):2095–100.
80. Haugsrud R, Norby T. Proton conduction in rare-earth ortho-niobates and ortho-tantalates. *Nat Mater* 2006 53. 2006 Feb 19;5(3):193–6.
  81. Zhang H, Wang Y, Xie L. Luminescent properties of Tb<sup>3+</sup> activated GdTao<sub>4</sub> with M and M' type structure under UV-VUV excitation. *J Lumin.* 2010 Nov;130(11):2089–92.
  82. Tsunekawa S, Takei H. Twinning structure of ferroelastic LaNbO<sub>4</sub> and NdNbO<sub>4</sub> crystals. *Phys status solidi.* 1978;50(2):695–702.
  83. Albino M, Veber P, Castel E, Velázquez M, Schenk K, Chapuis G, Lahaye M, Pechev S, Maglione M, Josse M. Growth and Characterization of Centimeter-Sized Ba<sub>2</sub>LaFeNb<sub>4</sub>O<sub>15</sub> Crystals from High-Temperature Solution under a Controlled Atmosphere. *Eur J Inorg Chem.* 2013 May 14;2013(15):2817–25.
  84. Mir SH, Takasaki Y, Engel ER, Takamizawa S. Ferroelasticity in an Organic Crystal: A Macroscopic and Molecular Level Study. *Angew Chemie Int Ed.* 2017 Dec 11;56(50):15882–5.
  85. Bhattacharya K. Microstructure of martensite: why it forms and how it gives rise to the shape memory effect. Oxford University Press; 2003. 288 p.
  86. Prytz O, Taftø J. Accurate determination of domain boundary orientation in LaNbO<sub>4</sub>. *Acta Mater.* 2005 Jan 10;53(2):297–302.
  87. Fulle K, McMillen CD, Sanjeeva LD, Kolis JW. Hydrothermal Chemistry and Growth of Fergusonite-type RENbO<sub>4</sub> (RE = La-Lu, Y) Single Crystals and New Niobate Hydroxides. *Cryst Growth Des.* 2016 Sep 7;16(9):4910–7.
  88. Jian L, Wayman CM. Electron back scattering study of domain structure in monoclinic phase of a rare-earth orthoniobate LaNbO<sub>4</sub>. *Acta Metall Mater.* 1995 Oct 1;43(10):3893–901.
  89. Brixner LH, Whitney JF, Zumsteg FC, Jones GA. Ferroelasticity in the LnNbO<sub>4</sub>-type rare earth niobates. *Mater Res Bull.* 1977 Jan 1;12(1):17–24.



90. Rojas-González FE, Hernández-Negrete O, Esparza-Ponce HE, Hernández-Paredes J. A method to decorate the surface of  $\text{LiNbO}_3:\text{Eu}^{3+}$  powders with  $\text{EuNbO}_4$  nanoparticles. *J Alloys Compd.* 2020 Jul 25;830:154688.
91. Uma S, Gopalakrishnan J.  $\text{K}_{1-x}\text{La}_x\text{Ca}_{2-x}\text{Nb}_3\text{O}_{10}$ , a Layered Perovskite Series with Variable Interlayer Cation Density, and  $\text{LaCaNb}_3\text{O}_{10}$ , a Novel Layered Perovskite Oxide with No Interlayer Cations. *J Solid State Chem.* 1993;102(2):332–9.
92. Frank A, Changizi R, Scheu C. Challenges in TEM sample preparation of solvothermally grown  $\text{CuInS}_2$  films. *Micron.* 2018 Jun 1;109:1–10.
93. Marfunin AS. *Advanced Mineralogy: Volume 1 Composition, Structure, and Properties of Mineral Matter: Concepts, Results, and Problems.* Advanced Mineralogy. Springer Berlin Heidelberg; 1994. 1–551 p.
94. Ji Y, Cao J, Zhu Z, Li J, Wang Y, Tu C. Luminescence Properties and White Emission in  $\text{Pr}^{3+}$  Doped Hexagonal  $\text{YAlO}_3$  Nanophosphors. *Mater Express.* 2011 Oct 10;1(3):231–6.
95. Feng W, Lin H, Liu H. Photoluminescence and Crystal-Field Analysis of  $\text{Pr}^{3+}$ -Doped  $\text{SrMoO}_4$  Phosphors. *Zeitschrift für Naturforschung - Sect A J Phys Sci.* 2015 Jan 1;70(1):11–6.
96. Li Y, Yu Q, Huang L, Wang J, Su Q, Huang XY, Han SY, Huang W, Liu XG, Zhou L, Yang J, Wang J, Li Y, Kuang XJ, Tang JK, Liang HB, Zhou W, Zhang G, Chen Y, Su Q, Liu XF, Teng Y, Zhuang YX, Xie JH, Qiao YH, Dong GP, Chen DP, Qiu JR, Ji XH, Zhang QY, Liu CM. Near ultraviolet and visible-to-near-infrared spectral converting properties and energy transfer mechanism of  $\text{Sr}_2\text{SiO}_4:\text{Ce}^{3+}$ ,  $\text{Pr}^{3+}$  phosphor. *Opt Mater Express*, Vol 4, Issue 2, pp 227-233. 2014 Feb 1;4(2):227–33.
97. Hatanaka M, Yabushita S. Theoretical Study on the f–f Transition Intensities of Lanthanide Trihalide Systems. *J Phys Chem A.* 2009 Nov 12;113(45):12615–25.
98. Hatanaka M, Yabushita S. Mechanisms of f–f hypersensitive transition intensities of lanthanide trihalide molecules: a spin–orbit configuration interaction study. *Theor Chem Acc.* 2014 Aug 1;133(8):1–15.
99. Van Hest JJHA, Blab GA, Gerritsen HC, De Mello Donega C, Meijerink A. Probing

- the Influence of Disorder on Lanthanide Luminescence Using Eu-Doped LaPO<sub>4</sub> Nanoparticles. *J Phys Chem C*. 2017 Sep 7;121(35):19373–82.
100. Suvorova EI, Stadelmann PA, Buffat PA. HRTEM simulation in determination of thickness and grain misorientation for hydroxyapatite crystals. *Crystallogr Reports*. 2004 May;49(3):343–52.
  101. Föll H. Twinning, Shear Deformation and Martensite Formation [Internet]. Available from:  
[https://www.tf.uni-kiel.de/matwis/amat/iss/kap\\_5/illustr/s5\\_4\\_3.html](https://www.tf.uni-kiel.de/matwis/amat/iss/kap_5/illustr/s5_4_3.html)
  102. Song Y, Shao B, Feng Y, Lü W, Huo J, Zhao S, Liu M, Liu G, You H. Emission Enhancement and Color Tuning for GdVO<sub>4</sub>:Ln<sup>3+</sup> (Ln = Dy, Eu) by Surface Modification at Single Wavelength Excitation. *Inorg Chem*. 2017 Jan 3;56(1):282–91.
  103. Butler SZ, Hollen SM, Cao L, Cui Y, Gupta JA, Gutiérrez HR, Heinz TF, Hong SS, Huang J, Ismach AF, Johnston-Halperin E, Kuno M, Plashnitsa V V., Robinson RD, Ruoff RS, Salahuddin S, Shan J, Shi L, Spencer MG, Terrones M, Windl W, Goldberger JE. Progress, challenges, and opportunities in two-dimensional materials beyond graphene. *ACS Nano*. 2013 Apr 23;7(4):2898–926.
  104. Liu Y, Bai G, Jiang L, Hua Y, Chen L, Xu S. Lanthanide Nd ion-doped two-dimensional In<sub>2</sub>Se<sub>3</sub> nanosheets with near-infrared luminescence property. *Nanophotonics*. 2020 Aug 1;9(8):2407–14.
  105. Clarke C, Singh M, Tawfik SA, Xu X, Spencer MJS, Ramanathan R, Reineck P, Bansal V, Ton-That C. Mono- to few-layer non-van der Waals 2D lanthanide-doped NaYF<sub>4</sub> nanosheets with upconversion luminescence. *2D Mater*. 2020 Oct 12;8(1):015005.
  106. Novoselov KS, Geim AK, Morozov S V., Jiang D, Zhang Y, Dubonos S V., Grigorieva I V., Firsov AA. Electric field in atomically thin carbon films. *Science*; 2004 Oct 22;306(5696):666–9.
  107. Huang J, Lu W, Wang J, Li Q, Tian B, Li C, Wang Z, Jin L, Hao J. Strategy to Enhance the Luminescence of Lanthanide Ions Doped MgWO<sub>4</sub> Nanosheets through Incorporation of Carbon Dots. *Inorg Chem*. 2018 Jul 16;57(14):8662–72.

108. Bai G, Yang Z, Lin H, Jie W, Hao J. Lanthanide Yb/Er co-doped semiconductor layered WSe<sub>2</sub> nanosheets with near-infrared luminescence at telecommunication wavelengths. *Nanoscale*. 2018 May 17;10(19):9261–7.
109. Viridi KS, Kauffmann Y, Ziegler C, Ganter P, Blaha P, Lotsch B V., Kaplan WD, Scheu C. Band Gap Extraction from Individual Two-Dimensional Perovskite Nanosheets Using Valence Electron Energy Loss Spectroscopy. *J Phys Chem C*. 2016 May 26;120(20):11170–9.
110. Li, B.-W.; Osada, M.; Ozawa, T. C.; Ebina, Y.; Akatsuka, K.; Ma, R.; Funakubo, H.; Sasaki, T. Engineered Interfaces of Artificial Perovskite Oxide Superlattices Via Nanosheet Deposition Process. *ACS Nano* 2010, 4, 6673–6680.
111. Görller-Walrand C, Binnemans K. Chapter 167 Spectral intensities of f-f transitions. *Handb Phys Chem Rare Earths*. 1998 Jan 1;25:101–264.
112. Peacock RD. The intensities of lanthanide f-f transitions. *Rare Earths*. 1975 Dec 13;83–122.



# 9. Curriculum Vitae

## Personal Information

Name and Sure name: Rasa Changizi  
Date of birth: 12.07.1990  
Place of Birth: Iran, Tehran  
Nationality: Dual (Iranian and German)

## University Education

10/2018 – 05/2022 PhD thesis at the Max-Planck-Institut für Eisenforschung GmbH (MPIE), Düsseldorf, Germany, research group Nanoanalytics and Interfaces (Prof. Christina Scheu)  
04/2015 – 08/2018 Studies of Physics at Heinrich Heine university of Düsseldorf, Germany  
Degree: Master of Science (M.Sc.)  
09/2009 – 08/2013 Studies of Physics at Shahid Beheshti university, Tehran, Iran  
Degree: Bachelor of Science (B.Sc.)

## Work experiences

06/2022 – present Project researcher at the Max-Planck-Institut für Eisenforschung GmbH (MPIE), Düsseldorf, Germany, research group Nanoanalytics and Interfaces (Prof. Christina Scheu)  
10/2018 – 05/2022 Research assistant at the Max-Planck-Institut für Eisenforschung GmbH (MPIE), Düsseldorf, Germany, research group Nanoanalytics and Interfaces (Prof. Christina Scheu)

- 05/2017 – 08/2018      Master thesis “Cathodoluminescence study of lanthanide-doped oxides” at the Max-Planck-Institut für Eisenforschung GmbH (MPIE), Düsseldorf, Germany, research group Nanoanalytics and Interfaces (Prof. Christina Scheu)
- 03/2016 – 04/2017      Student research assistant at at the Max-Planck-Institut für Eisenforschung GmbH (MPIE), Düsseldorf, Germany, research group Nanoanalytics and Interfaces (Prof. Christina Scheu)

## 10. List of publications, presentations and awards

### 10.1. Scientific publications

1. Changizi, R.; Zaefferer, S.; Ziegler, C.; Romaka, V.; Lotsch, B.; and Scheu, C.; Structural and Cathodoluminescence Investigations of Pr<sup>3+</sup>-Doped Ca<sub>2</sub>Nb<sub>3</sub>O<sub>10</sub> Nanosheets, submitted.

Contributions: (S)TEM, EDX, CL and HRTEM image analysis were performed by Rasa Changizi. Stefan Zaefferer helped with the CL measurements. Crystal structure CIF file was created by Vitaliy Romaka. Synthesis of the 2D nanosheets was done by Christian Ziegler. The manuscript is submitted.

2. Changizi, R.; Zaefferer, S.; Abdellaoui, L.; and Scheu, C.; Effects of of Defect Density on Optical Properties Using Correlative Cathodoluminescence and Transmission Electron Microscopy Measurements on Identical PrNbO<sub>4</sub> Particles, ACS Appl. Electron. Mater. 2022, 4, 4, 2095–2100.

Contributions: (S)TEM, CL measurements and analysis were performed by Rasa Changizi. BSE measurements were carried out by Stefan Zaefferer. FIB lamella preparation was done by Lamy Abdellaoui. The manuscript was written by Rasa Changizi and revised by all the authors.

3. Changizi, R.; Zhang, S.; Ziegler, C.; Schwarz, T.; Lotsch, B.; and Scheu, C.; Correlation between Structural Studies and the Cathodoluminescence of Individual Complex Niobate Particles, ACS Appl. Electron. Mater. 2021, 3, 461–467.

Contributions: SEM, EDX, CL and TEM measurements performed by Rasa Changizi, XRD measurements and synthesis of the samples done by Christian Ziegler. CL and XRD analysis were done by Rasa Changizi with the help of Siyuan Zhang. The manuscript was written by Rasa Changizi and revised by all the authors.

4. Frank, A.; Changizi, R.; and Scheu, C.; Challenges in TEM Sample Preparation of Solvothermally Grown CuInS<sub>2</sub> Films. Micron 2018, (DOI 10.1016/j.micron.2018.03.003).

Contributions: FIB lamella preparation, (S)TEM and EDX measurements were performed by Anna Frank. Conventional TEM sample preparations were done by Rasa Changizi. The manuscript was written by Anna Frank and revised by all the authors.

### 10.2. Poster presentations

1. Changizi, R.; Lim, J.; Zhang, S.; Schwarz, T.; Scheu, C.: Characterization of KCa<sub>2</sub>Nb<sub>3</sub>O<sub>10</sub>. IAMNano 2019, International Workshop on Advanced and In-situ Microscopies of Functional Nanomaterials and Devices, Düsseldorf, Germany (2019)
2. Changizi, R.; Zhang, S.; Schwarz, T.; Scheu, C.: Structural study and luminescence properties of Lanthanide-doped oxides. Microscopy Conference 2019, Berlin, Germany (2019)

3. Changizi, R.; Zhang, S.; Schwarz, T.; Scheu, C.: Cathodoluminescence and the structural study of Lanthanide-doped oxides. Workshop on Transmission Electron Microscopy (E-MAT), Antwerp, Belgium (2019)
4. Changizi, R.; Zhang, S.; Schwarz, T.; Scheu, C.: Study of the chemical composition and the luminescent spectra of Lanthanide-doped oxides. E-MRS 2019 Spring Meeting, Nice, France (2019)

### **10.3. Awards**

1. Communication award for science video competition at Max-Planck-Institut für Eisenforschung GmbH (MPIE), November 2021, Düsseldorf, Germany
2. First prize of the microscopy conference (MC 2019) Best image content, “Art in sciences”, September 2019, Berlin, Germany



# Acknowledgment

It would have not been possible to write this thesis without the help from all the people mentioned below:

I would like to thank my dear supervisor Prof. Christina Scheu. Tina, I loved the way you let me grow and be stronger and confident, both scientifically and personally. I am proud of you and absolutely adore the trust relationship that you develop between you and your students. Working by your side gave me the chance to fall in love with science one more time. I can only appreciate your support and wish to one day become a caring leader just like you.

I would also like to give a big thanks to Prof. Stefan Zaeferrer. Discussing scientific problems with you was always enjoyable. Please keep teaching science to students the way you do!

The main focus of my PhD thesis was to learn operating TEM and the physics behind it. I want to thank MPIE for giving me the chance to participate in the TEM school in Antwerp -EMAT 2019-. There I had the chance to meet amazing people and learn TEM in a very fun and collaborative way.

Also, I would like to thank Jörg Thomas. I was always impressed how patient you were in your role of teaching TEM to students. MPIE will always need technicians like you!

Volker Kree and Philipp Watermeyer are the other technicians who helped me during my journey of learning the machines (SEM, TEM, FIB, etc.), thank you so much for that!

Also, I thank Dr. Subin Lee for his help with the finer points of TEM and HRTEM simulation.

Living in Germany as a foreigner who couldn't initially speak German was sometimes very difficult, especially dealing with visa process, contracts, insurance and other bureaucracy related work. I was lucky to get to know Sophia-Helena Zwaka who is the international officer in MPIE. She always helped me in this regard and I want to emphasize here how important her role was.

A big thanks to Tanja Sondermann and Achim Kuhl for their technical support, especially during the COVID-19 pandemic. Their help was very much needed and they made sure to fix all the problems as soon as possible.

During the last year of PhD I had the chance to compete with other PhD students in MPIE to make science videos and I won the communication award for that. This was not possible without Yasmin Ahmed Salem who is the Press and Public Relations Officer. Yasmin, you turned this competition into a fun experience. Thanks a lot for that!

Angelika Gedsun and Zahra Kahrobaee, you were my dearest colleagues during the last 3 and a half years. We bonded over tea and became good friends. This friendship will not come to an end like our PhD theses and I am already looking forward to celebrating more Christmases and Nowruzes with you.

I thank the whole SN and NG groups for the fun times and their support during the last years.

Gavin Dutrow and Dr. Hanna Bishara, I was so glad to have your help and support in proofreading parts of my thesis. Thanks a lot for that.

Many thanks to my dearest friends Laura Silletti and Julia Andrews for the wonderful time we spent together in Duesseldorf and your support.

I want to give a very special thanks to my beloved partner, Daniel. This thesis without your help, support and presence would have been literally impossible. You were the main source of luminescence in my life especially during the last three years. A huge thanks to you not only for your emotional support but also for the proofreading of my thesis, papers and our physics related discussions.

Last but not least acknowledgment will go to my amazing family; Maman, Baba, Reza and Ramin, I was able to finish this journey with all your emotional help and support. Although you were far away from me, especially due to COVID-19, I appreciate that you always stayed in close contact with me via regular phone calls and video calls. You are the best family one could ever ask for.

Final thought for the reader,

I have written most of this thesis during the COVID-19 pandemic. This was a very difficult time and if it was not for that, more collaborations and conferences would have been possible. On the other hand, I found light in the darkness. During the whole pandemic science became a way for me to escape the world's madness. It helped me stay confident and happy in the most difficult days that I had ever faced in my life. Thus, I thank science for giving me the faith to stay strong.